CONSTRAINING SOIL FORMATION AND DEVELOPMENT THROUGH QUANTITATIVE ANALYSES OF CHEMICAL WEATHERING AND PHYSICAL EROSION

Jérôme Schoonejans

Thèse présentée en vue de l'obtention du grade de Docteur en Sciences

OCTOBER 2016

Université catholique de Louvain
Faculté des Sciences
Earth and Life Institute - Georges Lemaître Centre for Earth and Climate Research

Place Louis Pasteur 3, 1348 Louvain-la-Neuve, Belgique
http://www.uclouvain.be/teclim

Examination committee

SUPERVISORS

- **Vanacker Veerle**

  Professor, Université catholique de Louvain. Earth and Life Institute, Georges Lemaître Centre for Earth and Climate Research, Belgium

- **Opfergelt Sophie**

  Professor, Université catholique de Louvain. Earth and Life Institute, Environmental Sciences, Belgium

EXAMINATION COMMITTEE

- **Chabaux François**

  Professor, Université de Strasbourg, Laboratoire d'Hydrologie et de Géochimie de Strasbourg (LHyGeS), Strasbourg, France.

- **De Keersmaecker Marie-Laurence (Chair)**

  Professor, Université catholique de Louvain. Earth and Life Institute, Georges Lemaître Centre for Earth and Climate Research, Belgium

- **Govers Gerard**

  Professor, KU Leuven. Department of Earth and Environmental Sciences, Belgium

- **van Wesemael Bas**

  Professor, Université catholique de Louvain. Earth and Life Institute, Georges Lemaître Centre for Earth and Climate Research, Belgium

Notice

Parts of this thesis (2 chapters) have been published in peer-reviewed journals and the remaining parts (2 chapters) are in preparation for a submission, as indicated below:

- **Chapter II**

  Schoonejans, J., V. Vanacker, S. Opfergelt, Y. Ameijeiras-Mariño, and M. Christl (2016), Kinetically limited weathering at low denudation rates in semi-arid climatic conditions, *Journal of Geophysical Research Earth Surface*, 121, doi:10.1002/2015JF003626.

- **Chapter III**

  Schoonejans, J., V. Vanacker, S. Opfergelt (in prep.) Topographic control on chemical weathering and soil development in deeply weathered subtropical soils (southern Brazil)

- **Chapter IV**

  Schoonejans, J., V. Vanacker, S. Opfergelt, M. Granet and F. Chabaux (2016), Coupling uranium series and ^{10}Be cosmogenic radionuclides to evaluate steady-state soil thickness in the Betic Cordillera, *Chemical Geology*, Article in Press, DOI: 10.1016/j.chemgeo.2016.03.030

- **Chapter V**

  Schoonejans, J., V. Vanacker, S. Opfergelt, M. Christl (in prep.) Long-term soil erosion derived from in-situ and meteoric 10Be inventories in deeply weathered soils in southern Brazil

Acknowledgements

So many people contributed directly or indirectly to the achievement of the present dissertation. First and foremost, I would like to express my gratitude to my supervisors and all the jury members for their valuable remarks which improved significantly the manuscript and for the constructive discussion we had.

Professor Veerle Vanacker, my supervisor, you have guided my research in an innovative and original way that stimulated my work during the last for years. Many thanks go to you since you have invested full effort to supervise my research and to push myself to achieve my objectives. I appreciated the way you converted issues into challenges and also your great support to revise carefully and endlessly the drafts of my manuscripts. Additionally, I'm grateful to have been introduced to innovative geochemical techniques and to have benefited from your experience on cosmogenic nuclides. I extend my acknowledgements to the numerous opportunities you offered me to attend conferences, workshops, Summer Schools and internship all over Europe.

Professor Sophie Opfergelt, my co-supervisor, I would like to thank you for your great availability, your generous support and your encouragements all along these four years of research. It was always a pleasure to listen to your thoughtful advices. I greatly appreciate the warm welcome among the SOLS research unit during my third year, when Veerle was on sabbatical year. I also really enjoyed your enthusiasm and positive attitude when we were preparing our field trips with Veerle and Yolanda.

I extend my thanks to the Professors Gerard Govers, Kristof Van Oost and Bas van Wesemael, members of the thesis committee, for always bringing wise and significant inputs. Your pieces of advice and your valuable comments were an enormous help to improve my methodology and the interpretation of my results, especially in the Chapter III and V. I should also mention their significant help during the field campaign in Brazil by their optimization of the management of the research team and by lending their hand and their sweat to dig soil pits. In addition, their cheerfulness and their positivism have contributed to the successful of this big challenge. . I would also like to thanks the Professor De Keersmaecker for having accepted to be President of my Jury and for

having conducted the defenses with serenity and humanity.

Professor François Chabaux. I'm deeply grateful to you for your involvement in my research project. I would also like to thank you for having accepted to be part of my jury thesis and for allowing me to make an internship at LHyGeS in Strasbourg. This offers me the opportunity to work in a forefront laboratory which is equipped with advance equipment and experimented research staff. Moreover, during the 3 months, I spent, I had the chance to exchange with fascinating researchers and discover an unforgettable region, where history, wine and traditions fit together.

This research project would not have been possible without the support of many people. If the thesis represents investigations during several years, research is also a piece of human and social life with the start of new collaborations and friendships. So, I would like to acknowledge with much appreciation the following persons:

The SOGLO PhD students (Dácil, Marie-Liesse, Benji, Marijn, Jeremy, Emmanuel) with whom we have built strong relationships and scientific exchanges during all the opportunities we had to spend time together. The month we spent together in Brazil will stay a memorable experience as well as all the EGU conference and the traditional SOGLO annual meetings. I would like to have some words for Yolanda, her cheerfulness during our first fieldtrip in Spain, during the sieving on the roof of the Hotel La Parra and at the basement of Mercator was always a great support. Thank you for your help and your meticulous approach when we had to deal with tens of samples in the SOLS lab.

The LHyGeS researchers who quickly taked me into their group. I'm grateful to all PhD student with whom I had constructive discussions but also great time. Special thanks to Julien for his help with the fancy U-Series Model and for sharing with me his good mood and his knowledge. I cannot forget to thank Eric Pelt who offered me accommodation, help while he was very busy and with I had very instructive discussions. Thanks also to all the others (Adrien, Clio, Harold, Izabella, Jean-Jean, Thiebaud,) with whom I keep so many good memories.

My colleague of the Mercator building with whom I had a lot of fun during our lunch time or during our overtime hours in the CS computer room and downtown for the after work in all the bars of LLN. My special words of appreciation are also addressed to Sylvain T. and François K. who were always available for having a blast together but also to Olivier L. and Pierre-Yves for their friendship and the precious moments we had.

At all my family and my friend for their support, their encouragements and their interest for my research even if it was not always easy to understand the essence of my subject.

And finally, I cannot end my acknowledgments without a word for the woman who became my wife during my PhD. I would like to warmly thank her for being the biggest support I have ever had and for having found the appropriate words to overcome roadblocks of the PhD.

Table of contents

List of symbols and abbreviations

a. s. l.	Above Sea Level
AMS	Accelerator Mass Spectrometry
CDF	Chemical Depletion Fraction (unit less)
CRONUS	Cosmic-Ray Produced Nuclide Systematics
CRN	Cosmogenic Radio Nuclide
CZ	Critical Zone
CZO	Critical Zone Observatory
C_i	Concentration of an immobile element I *(Ti, Zr)* (weight %)
C_j	Concentration of an element j (weight %)
D	Soil surface Denudation (mm/kyr)
E	Physical Erosion
ETH Zurich	Swiss Federal Institute of Technology in Zurich
ET_p	Mean annual Evapotranspiration (mm/yr)
H	Soil or regolith thickness (mm)
f_j	First order rate constant for input coefficient (or gain) of nuclide j (yr^{-1})
FAO-WRB	FAO-World Reference Base (soil taxonomy)
ICP-AES	Inductively Coupled Plasma - Atomic Emission Spectroscopy
ICP-MS	Inductively Coupled Plasma - Mass Spectrometry.
$I_{^{10}Be}$ or $I_{^{9}Be}$	Inventory of meteoric ^{10}Be or ^{9}Be (at/cm²)
$I'_{^{10}Be}$	Inventory of meteoric ^{10}Be corrected for losses (at/cm²)
k_j	First order rate constant for output coefficient (or loss) of nuclide j (yr^{-1})
LHyGeS	Laboratoire d'Hydrologie et de Géochimie de Strasbourg
L_w	Regolith thickness (m)
$m_{j,\,flux}$	mass flux of an element *j* in a soil profile (kg/m²)
$m_{j,\,flux\,n}$	Thickness normalized mass flux in a soil profile (kg/m²)
M_{tot}	Total weathering mass fluxes of a regolith profile (kg/m²)
MAT	Mean annual precipitation (mm/yr)
MAT	Mean annual temperature (°C)
N_0	^{10}Be concentrations at the surface (z = 0) (at/g)
N_z	^{10}Be concentrations at the surface and depth (z) (at/g)
N_j	Nj is the abundance of the nuclide ^{238}U, ^{234}U, ^{230}Th or ^{226}Ra (in number of

	atoms)
P	Soil Production (mm/kyr)
q	Delivery rate of meteoric ^{10}Be (at cm^{-2} yr^{-1})
SSHO	Susquehanna Shale Hills Observatory (central Pennsylvania)
SSST	Steady-State Soil Thickness
t	Time (yr)
$T_{1/2}$	Half-live radioactive decay (yr)
U-series	Uranium series isotopes (^{238}U, ^{234}U, ^{230}Th and ^{226}Ra)
W	Chemical weathering
z	Soil/regolith depth (mm)
XRD	X-ray Diffraction
$\varepsilon_i(z)$	Strain or volumetric expansion (+) or collapse (-) of the soil at the depth z (unit less)
λ	Radioactive decay constant of an element (yr^{-1})
Λ	Path attenuation length of cosmic rays (g/cm^2)
ρ	Soil/Rock bulk density (g/cm^3)
τ_x	Fractional mass gain or loss per element x in a soil profile (unit less)
$[X]$	Concentration of the element *X* in the soil/rock (mg/kg)

Chapters

Chapter I

Introduction

A soil system under pressure

At the Earth surface, the terrestrial life is supported by a very thin layer. The latter, called the soil mantle or mobile regolith, is a porous matrix constituted by inorganic material derived from weathered and fragmented bedrock, water, air and organic matter from living and dead organisms. The average fraction of each constituent is estimated at 45, 25, 25 and 5 % although they vary according to the environmental conditions, and are dynamic as a result of soil development [*Brady and Weil*, 1996].

The soil system appears as a stack of horizons that are more or less well-defined and results from the interaction between five soil forming factors: lithology, climate, biological activities, relief and time [*Jenny*, 1941]. The thickness of the soil mantle is governed on the one hand by soil production resulting from mechanical disintegration and chemical weathering of the bedrock and input from atmospheric dust and on the other hand by soil denudation from losses of solutes and soil particles. Soil forming processes are slow on a human timescale, and take place over hundreds or thousands of years. Soil formation rates are controlled by the intensity of chemical weathering and physical erosion (Figure 1.1).

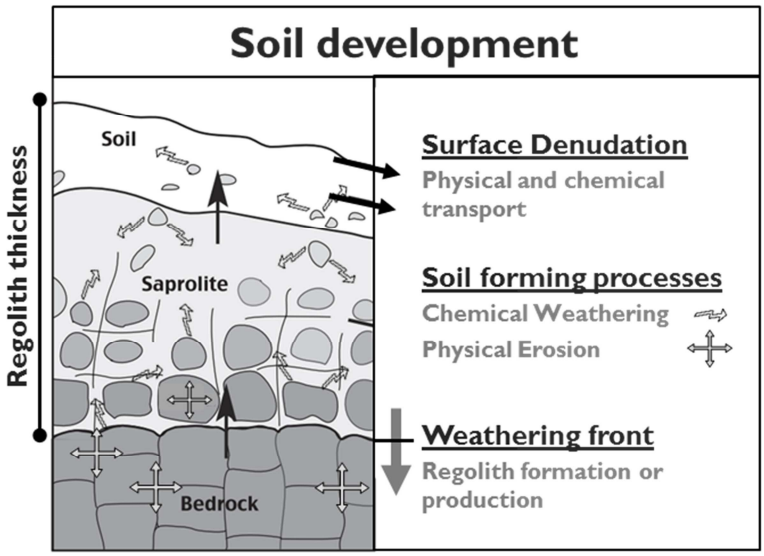

Figure 1.1: Schematic overview of the main processes of the soil development. Upward arrows are indicative for vertical particle fluxes; diagonal arrows for lateral particle and solid fluxes, electric arrows for chemical weathering of minerals and crossed arrows for physical breakdown of the bedrock (modified from Brantley et al. [2011])

Chemical weathering encompasses aqueous alterations and transformations of primary minerals of the bedrock which are driven by a thermodynamic disequilibrium with respect to their forming conditions in the Earth's crust. Among these reactions, we can distinguish chemical reactions involving dissolution of carbonates, oxidation of iron minerals producing e.g. hematite, hydrolysis of feldspars forming secondary minerals (i.e. clays) and Fe/Al oxides and biochemical reactions caused by the metabolism of living organisms - for example, the exudate of organic acids and release of CO_2 from respiration by plant roots. Chemical reactions are enhanced by temperature which conditions the speed of the reaction and by water availability which transports the weathering agents and products in the soil system.

Physical erosion fragments and breaks down the bedrock through e.g. ice growth in rock fractures, root penetration, pressure release after a landslide and thermal expansion or contraction due to sun exposure [*Holden*, 2005; *Anderson*, 2007; *Amundson*, 2007; *Bauer and Velde*, 2014].

The soil system can be considered as a reactor where interactions between the atmosphere, bedrock, water and vegetation take place. This is why soils are a central component of the so-called Critical Zone (CZ), a concept uniting all those components

and stretching from the underground aquifers to the top of the canopy [*National Research Council*, 2001; *Brantley*, 2006; *Anderson*, 2007]. The CZ is also known as a supplier of ecosystem services by providing primary resources and energy to society through e.g. supply of wood and minerals, water filtration, and waste degradation. However, over the past three centuries the human population has increased tenfold to more than 7 billion causing profound anthropogenic disturbances to the soil-landscape system which can profoundly affect the CZ by altering lateral and vertical fluxes of soil nutrients and soil particles at the land surface [*Raymond and Cole*, 2003; *Foley et al.*, 2005; *Vanacker et al.*, 2014].

Human activities can alter soil formation and development to the extent that humans are now identified as the sixth soil forming factor [*Dudal*, 2004; *Richter*, 2007]. According to *Crutzen* [2002], 30 to 50% of the land surface and more than 50% of the freshwater resources are exploited by humans. On a global scale, modern erosion rates are about one order of magnitude higher than the natural erosion rates [*Hooke*, 2000; *Wilkinson*, 2005; *Montgomery*, 2007; *Vanacker et al.*, 2007; *Cerdan et al.*, 2010]. A study, conducted by *Wilkinson and McElroy* [2007], has evaluated at about 21Gt yr^{-1} the global sediment flux to the oceans, with 83% of this flux derived from the highest 10% of Earth's surface. When taking into account anthropogenic erosion, the global sediment flux increases more than three times and reaches about 75Gt yr^{-1} [*Wilkinson and McElroy*, 2007]. Moreover, the spatial distribution of the main source areas changes drastically, as the main portion of anthropogenic sediment (65%) comes from lowlands such as stable cratons and passive continental margins (below 350 m of altitude) where intensive agriculture is concentrated. Despite the increase of the global sediment flux over the last five centuries, the volume of sediment that is delivered to the ocean has decreased by 15% compared to pre-anthropogenic times because a significant portion of the sediment is intercepted by manmade reservoir or dams [*Syvitski and Kettner*, 2011].

It is therefore essential for the scientific community to measure precisely the impacts of anthropogenic activities on the soil system. The SOGLO project (Soils Under Global Change) funded by the Belgian Federal Science Policy (BELSPO), involving four Belgian universities, three foreign partners and more than 20 researchers has the aim to answer this challenging question using an integrated approach (https://hal.elic.ucl.ac.be/soglo/).

The research presented in this thesis is part of the SOGLO project, and aims to quantify

natural rates of soil development in order to provide a baseline reference for distinguishing human impact on the soil system. Recent technological advances and isotopic methods now allow us to quantify soil formation and geomorphic processes (Figure 1.2) over timescales of 10^3 to 10^5 years. By constraining the rates of soil production, soil denudation and chemical weathering, it becomes possible to reconstruct long-term soil development.

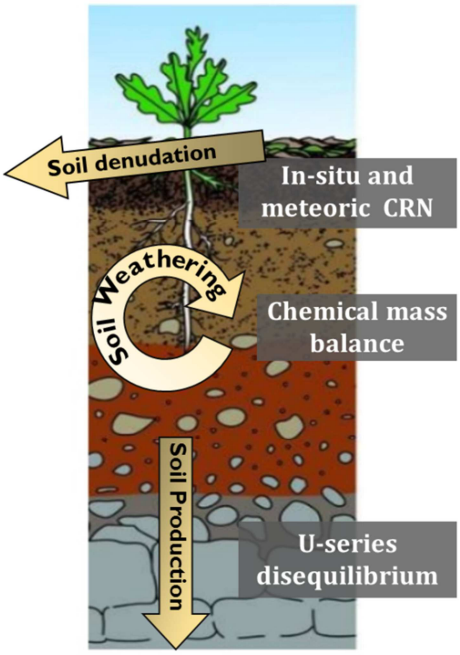

Figure 1.2: The thickness of the soil system depends on soil production, weathering and denudation processes, and can be constrained using geochemical techniques based on respectively U-series disequilibrium, chemical mass balances and cosmogenic radionuclides.

In this thesis, we make use of three independent geochemical techniques in order to quantify the rates of soil development: U-series disequilibrium for constraining soil production rates, chemical mass balances for soil weathering intensities, and in-situ and meteoric cosmogenic radionuclides for determining soil denudation rates. They are presented and briefly described below, while more details are provided in the following chapters.

In-situ and meteoric produced cosmogenic radionuclides

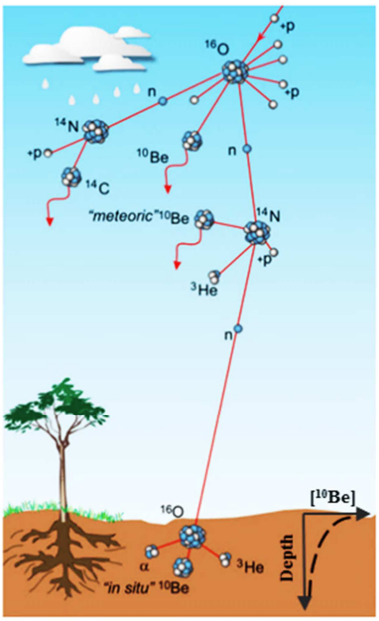

Figure 1.3: Figure illustrating the production of meteoric ^{10}Be in the atmosphere and in-situ ^{10}Be isotopes at the Earth surface (modified from von Blanckenburg and Willenbring [2014])

In-situ and meteoric produced cosmogenic radionuclides (CRN) allow us to constrain long-term (10^4 – 10^6 years) denudation rates at the hillslope and catchment scale [*Gosse and Phillips*, 2001; *von Blanckenburg*, 2005; *Balco et al.*, 2008]. Cosmogenic nuclides (isotopes: ^{10}Be or ^{26}Al) are produced at a predictable rate in quartz grains (in-situ) near the Earth's surface and in the atmosphere (meteoric) (Figure 1.3). At sea level high latitude, the production rate of in-situ cosmogenic radionuclides is about 4.65 atoms per gram of quartz per year. The delivery of meteoric ^{10}Be to the surface depends on dust-aerosol and precipitation inputs and the ^{10}Be concentration in the source material. The accumulation of these isotopes can then be used as a cosmogenic clock that records the residence time of the material in the upper few meters of the Earth's surface, and is also indicative for the accumulation or removal of soil particles at the surface as a result of erosion or deposition processes. If one assumes that the soil thickness remains constant over the integration time (so-called steady state soil thickness), the concentration of CRN can also be used to derive soil production rates. More details are given in the *Chapter II* and *V*.

Geochemical mass balance methods

Geochemical mass balance methods allow us to constrain the intensity of chemical weathering in the soil system, and to quantify the fraction of soil denudation that can be attributed to chemical weathering [*Brimhall et al.*, 1992; *Riebe et al.*, 2003; *Yoo and Mudd*, 2008; *White and Buss*, 2014]. Mass balance equations are used to quantify mass transfer changes of elements when transforming from unweathered bedrock to soil material, and are based on the principle that immobile elements (such as Zr, Ti or Hf) behave conservatively in the soil system. As the calculations are highly dependent on the immobile elemental concentrations, the reference element should be conservative in the soil system. The intensity of weathering can then be measured by comparing the concentration of the conservative elements in the bedrock and weathered material. More details are given in the *Chapter II* and *III.*

U-series disequilibrium

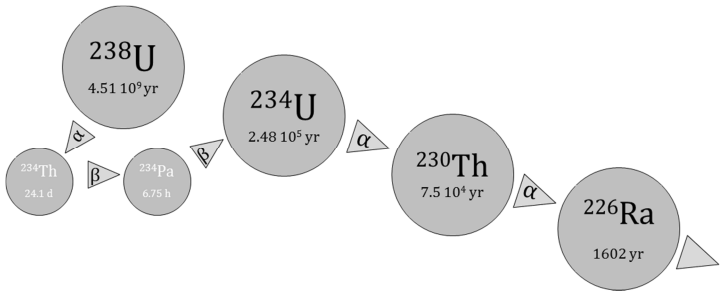

Figure 1.4: Figure showing the main nuclides (in black) of the ^{238}U radioactive series that are used in the U-series disequilibrium method. Half-lives ($T_{1/2}$) are indicated below each nuclide. Arrows denote for α-decay (emission of 2 protons and 2 neutrons) and β-decay (neutron and proton conversion and emission of 1 electron) (inspired on Chabaux et al. [2003a]; Dosseto et al. [2008b])

Uranium isotopes (Figure 1.4) can reveal U-series disequilibrium that allow us to quantify the long-term advance of the weathering front in the bedrock, and constrain the soil production rate [*Ma et al.*, 2010; *Chabaux et al.*, 2011; *Dosseto et al.*, 2012; *Suresh et al.*, 2013]. In bedrock older than 1 Ma, the activity ratios of uranium-series nuclides equal to 1. The weathering of primary minerals disrupts this secular equilibrium and leads to a radioactive disequilibrium between the different nuclides. From this moment the radioactive clock is initialized because each nuclide will begin to return to the secular equilibrium by radioactive decay. Usually it is considered that the time needed to return to secular equilibrium is around 5 or 6 half-lives of the daughter nuclide. More details are given in the *Chapter IV*.

Chemical weathering and physical erosion of soils

Quantitative understanding of the interaction between mechanical rock breakdown, chemical weathering, and physical erosion is essential for unraveling Earth's biogeochemical cycles [*Raymo and Ruddiman*, 1992]. On a geological time scale, the weathering of silicate minerals contained in rock and soil consumes atmospheric CO_2 and it results in a progressive uptake of this greenhouse gas from the atmosphere [*Berner et al.*, 1983; *Raymo and Ruddiman*, 1992; *Li and Elderfield*, 2013]. The (de)coupling between chemical weathering and physical erosion in various environmental settings has to be clarified in order to understand the role of silicate weathering in global geochemical cycles.

Field data and soil weathering models have shown that physical erosion and chemical weathering are positively correlated in many environments [*Ferrier and Kirchner*, 2008; *Gabet and Mudd*, 2009]. However, the feedbacks between soil production at the base of the regolith, chemical weathering (W), and erosion (E) are not yet fully understood. The mechanical breakdown of fresh bedrock enhances chemical weathering through increase of the specific surface area of rock fragments and supply of fresh and easily weatherable minerals [*Riebe et al.*, 2004; *Norton and von Blanckenburg*, 2010]. The supply of fresh particles is often considered to be the limiting factor for soil formation, and these conditions are often described as *supply limited* weathering regimes where $W \propto E^{\lambda=1}$. However, reaction kinetics may limit chemical weathering processes in e.g. areas with sufficiently high erosion rates due to shorter soil residence times which do not allow the minerals to weather completely [*West et al.*, 2005]. In such environments, the relation between physical erosion and chemical weathering stays positive but the increase in erosion rates leads to a lower increase in weathering rates, and this regime is described as *kinetically limited weathering regime* ($W \propto E^{\lambda<1}$). In environments where the soil system is very thin (and the mineral residence time short), the relation between physical erosion and chemical weathering breaks apart. In this case, the weathering reactions are controlled by weathering kinetics and are described as *kinetically controlled regimes [Dixon et al., 2012]* ($W \propto 1/E^{\lambda\leq1}$).

To enhance our understanding of the interaction between mechanical rock breakdown, chemical weathering, and physical erosion, it is essential to have robust geochemical techniques that allow us to constrain independently the soil production, weathering and erosion rates. By combining the three geochemical methods described above, we are able

to test new hypotheses related to the coupling of chemical weathering and soil denudation in two contrasting study sites.

Contrasting study sites

Two soil observatories have been selected in concertation with the other partners of the SOGLO project, in order to constrain long-term soil production and denudation rates. The eastern side of the Betic Cordillera (SE Spain) is the first study area, while the second study site is located in the central part of the southern State of Brazil, the Rio Grande Do Sul. Full details on the environmental settings of the two sites are given in the chapters II to V and are also resumed in Table 1.1.

The two sites offer us the opportunity to analyze soil development in two contrasting environments: the Betic Cordillera is characterized by steep topography and high denudation rates, and low availability of water during a prolonged period of the year. We posit that chemical weathering is limited by the water fluxes in the soil system. In contrast, southern Brazil has a rolling topography and low denudation rates, and water is abundantly available throughout the year. We posit that the rate of weathering in Brazil is limited by the supply of fresh minerals from the bedrock [e.g. *Ferrier and Kirchner*, 2008].

Table 1.1: Localization of the study sites concerned in the thesis and their main environmental characteristics [ESRI, 2009]

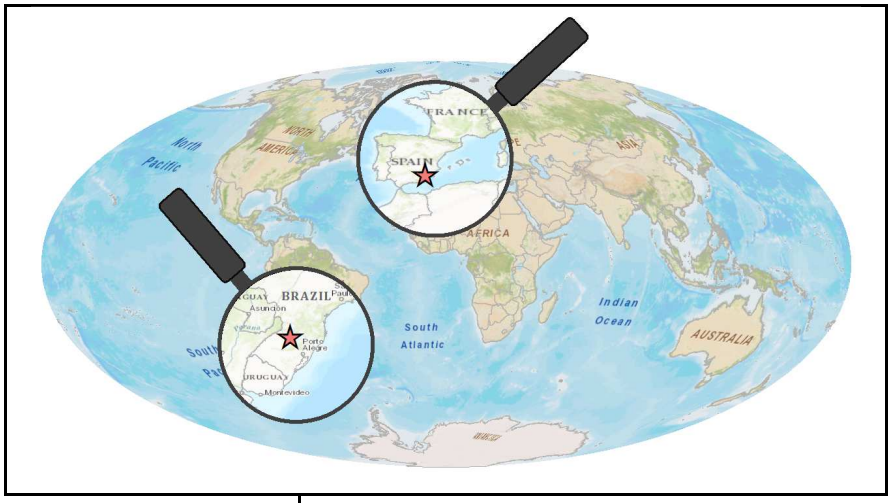

	Betic Cordillera (SE Spain)	**Rio Grande Do Sul (southern Brazil)**
Climatic regime	Semi-arid	Sub-tropical
- **MAP**[1]	- 275-425 mm/yr	- 1700-1800 mm/yr
- **MAT**[1]	- 12 – 17°C	- 16-20°C
- **ET_p**[2]	- 800-900 mm/yr	- 780 mm/yr
Vegetation type and density	Matorral (shrubs) sclerophyllous and thorny. Scattered	Deciduous sub-tropical forest. Dense
Lithology	Metamorphic rocks initiated around 51 Ma (Mica-schist, phyllite, quartz veins)	Lava flow dated from 127-137 Ma (ryhodacite)
Soil type (WRB soil taxonomy, FAO)	Regosol and Cambisol	Alisol and Acrisol
Landscape morphology	Mountainous and tectonically active zone	Dissected plateau

[1]: Range of mean annual precipitation and mean annual temperature derived from national climate databases.

[2]: Mean annual potential evapotranspiration, calculated with the Thornthwaite method [*Palmer and Havens*, 1958]

Research objectives

This study seeks to improve our quantitative understanding of soil development processes. The main objective is to provide new insights on soil development on time scales of 10^3 to 10^5 years based on field data and novel geochemical analyses of soil and bedrock samples. The research focused on three research objectives:

1. First, we explore the relation between chemical weathering and physical erosion in two contrasting settings, and evaluate the climatic and topographic factors limiting soil production and chemical weathering.

2. Second, we explore the concept of the steady state soil thickness (SSST) that assumes that soils have a constant thickness that depends mainly on local environmental conditions, and lithology. This concept is often cited in the literature, but has rarely been validated with field data. By using two independent geochemical techniques (U-series and in-situ ^{10}Be), we provide novel data on the association between soil production and denudation. For constraining long term soil processes, the thesis was oriented towards the development and application of new isotopic techniques. We have taken advantage of the most recent developments in U-series disequilibrium analyses, which is an isotopic method that allows one to assess the rate of progress of the weathering front in the bedrock (soil production).

3. Third, we constrain long term soil denudation rates of subtropical soils using meteoric ^{10}Be. The use of meteoric ^{10}Be in old and well-developed soils remains challenging because of potential leaching of the element in acidic conditions. To resolve this issue, we test a method that accounts for the losses of meteoric ^{10}Be in the soil system, thereby improving the reliability of the meteoric ^{10}Be-derived denudation rate estimates for highly weathered soils. The results are then validated with denudation rates obtained from in-situ ^{10}Be, that is formed inside the quartz lattice and conservative in the soil system.

Thesis outline

The PhD dissertation is organized in six chapters, including this introduction (Chapter I).

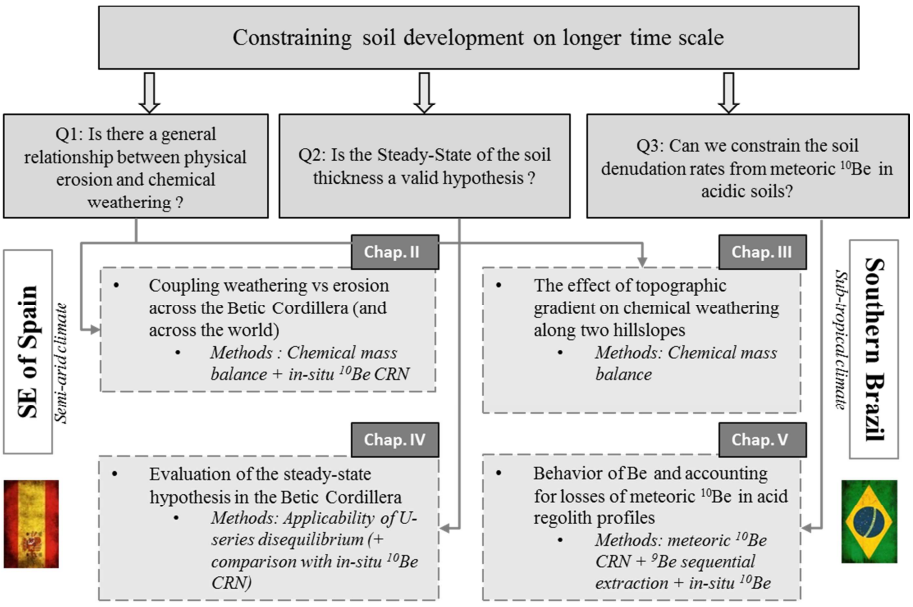

Figure 1.5: Structure of the thesis

The ***chapter II*** focuses on the relationship between soil production, catchment-wide denudation, and chemical weathering in a semi-arid environment. The central hypothesis here is that the production of mobile regolith and soil material by mechanical rock breakdown and chemical weathering in semi-arid conditions is kinetically limited, even at low rates of total denudation.

Chapter III focuses on the topographic control on chemical weathering mass fluxes. The analysis is based on two toposequences in a natural forest in southern Brazil that have different slope morphology. Chemical mass balance techniques are used to understand how weathering fluxes evolve with respect to slope morphology.

The validation the steady-state hypothesis of soil thickness is addressed in ***Chapter IV***. For the sites in the Betic Cordillera, two independent geochemical techniques are applied to constrain independently soil production and soil denudation rates. Soil denudation rates are derived from *in-situ* produced ^{10}Be, while soil production rates are derived from the isotopic disequilibrium of Uranium isotopes in the soil (U-series disequilibrium). This work has been possible with to the support of the LHyGeS laboratory at the University of Strasbourg.

In ***Chapter V***, meteoric ^{10}Be isotopes are used as a tracer to quantify soil denudation. Given the high rates of chemical weathering of the soils in this subtropical environments, the method is adapted to account for potential leaching of the Be element in the soil system. For soil samples taken from a steep toposequence in southern Brazil (identical to *Chapter III*), successive chemical extractions are realized to understand the behavior of Beryllium in the soil system. Then concentrations of meteoric ^{10}Be are corrected for chemical leaching in order to quantify the soil denudation rates. The rates are then validated with denudation rates from in-situ produced ^{10}Be isotopes.

The ***Chapter VI*** sums up the main findings presented in *Chapter II* to *Chapter V* and provides some implications for future research.

The supporting materials for all chapters are presented at the end of the thesis.

Chapter II

Kinetically limited weathering at low denudation rates in semi-arid climatic conditions

Based on:
Schoonejans, J., V. Vanacker, S. Opfergelt, Y. Ameijeiras-Mariño and M. Christl (2016b), Kinetically limited weathering at low denudation rates in semiarid climatic conditions, Journal of Geophysical Research: Earth Surface, 121(2), 336-350, doi:10.1002/2015JF003626.

ABSTRACT

Biogeochemical cycling within the critical zone depends on the interactions between minerals and fluids controlling chemical weathering and physical erosion rates. In this study, we explore the role of water availability in controlling soil chemical weathering in semi-arid climatic conditions. Weathering rates and intensities were evaluated for nine soil profiles located on convex ridge crests of three mountain ranges in the Spanish Betic Cordillera. We combine a geochemical mass balance with ^{10}Be cosmogenic nuclides to constrain chemical weathering intensities and long-term denudation rates. As such, this study presents new data on chemical weathering and ^{10}Be derived denudation for understudied semi-arid climate systems. In the Betic Cordillera, chemical weathering intensities are relatively low (~5 to 30

% of the total denudation of the soil) and negatively correlated with the magnitude of the water deficit in soils. Chemical mass losses from soils are inversely related to denudation rates (14-109 mm/kyr) and positively to soil thickness (14-58 cm), these results are consistent with kinetic limitation of chemical weathering. A worldwide compilation of chemical weathering data suggests that soil water balance may regulate the coupling between chemical weathering and physical erosion by modulating soil solute fluxes. Therefore future landscape evolution models that seek to link chemical weathering and physical erosion should include soil water flux as an essential driver of weathering.

INTRODUCTION

On Earth, the Critical Zone supports terrestrial life, being the near-surface environment where interactions between the atmosphere, lithosphere, hydrosphere and biosphere take place [*Brantley et al.*, 2006; *Anderson et al.*, 2007]. This heterogeneous zone extends from the top of the canopy down to the groundwater table, and encompasses organisms, soil, rock, air and water [*National Research Council*, 2001]. Within the Critical Zone, the thickness of the soil is controlled by soil production at the base of the mobile regolith, chemical weathering within the regolith, and physical soil erosion and deposition at the soil surface [*Heimsath*, 1997; *Chadwick and Chorover*, 2001; *Buss et al.*, 2005]. In eroding settings, chemical weathering and physical erosion are the dominant processes of soil formation and development, and their process' rates mainly depend on local topography, lithology, hydrology, and vegetation [*Crews et al.*, 1995; *Drever and Stillings*, 1997; *Chadwick et al.*, 1999; *West et al.*, 2005; *Bhatt and McDowell*, 2007]. *Rasmussen et al.* [2010]; *White and Blum* [1995] and *White et al.* [1999] have recognised the fundamental role of soil hydrology in regulating weathering fluxes, and the positive effect of soil temperature on reaction kinetics.

Quantitative understanding of the interaction between mechanical rock breakdown, chemical weathering and physical erosion is essential for unraveling Earth's biogeochemical cycles [*Raymo and Ruddiman*, 1992]. Field data and soil weathering models have shown that mechanical breakdown of bedrock enhances chemical weathering through increase of the specific surface area of rock fragments and supply of fresh minerals [*White et al.*, 1996; *Hodson and Langan*, 1999; *Cohen et al.*, 2009; *Riggins et al.*, 2011; *Yoo et al.*, 2011; *Vanwalleghem et al.*, 2013; *Attal et al.*, 2015]. In

addition, dissolution of primary minerals leads to a weakening of rocks and fragments which facilitates mechanical breakdown. Physical erosion and chemical weathering rates are positively correlated in many environmental settings where chemical weathering is limited by the supply of fresh minerals [e.g. *Anderson et al.*, 2002; *Millot et al.*, 2002; *Riebe et al.*, 2004; *West et al.*, 2005; *Brantley et al.*, 2007; *Larsen et al.*, 2014]. However, in areas of sufficiently high physical erosion rates, reaction kinetics may limit weathering processes due to reduced mineral residence time as suggested by modeling and observational studies [e.g. *Gabet*, 2007; *Ferrier and Kirchner*, 2008; *Gabet and Mudd*, 2009]. As physical erosion rates increase, the residence time of minerals in the thin weathering zone is shorter than the duration of chemical weathering for most primary mineral phases [e.g. *Hilley et al.*, 2010]. As such, in thin weathering zones, increases in physical erosion rates are expected to result in decreases in chemical weathering intensities.

Recent observational studies suggested that chemical weathering and physical erosion rates can be positively related even at very high rates of soil erosion [*White and Brantley*, 2003; *Larsen et al.*, 2014]. Water availability is cited as one of the principal rate-controlling factors [*Rasmussen et al.*, 2011; *Maher*, 2011], and potentially explains the high rates of soil production and weathering intensities measured in the extremely wet climate of the western Southern Alps of New Zealand. However, the hydrological regulation of chemical weathering processes is still poorly constrained as there still are few observational datasets on soil production and chemical weathering rates. More data are needed across a broad range of climatic conditions to quantify the strength and direction of the relationship between chemical weathering and physical erosion.

This study focuses on the relationship between soil production, denudation, and chemical weathering in a semi-arid environment. The central hypothesis here is that the production of mobile regolith and soil material by mechanical rock breakdown and chemical weathering in semi-arid conditions is kinetically limited, even at low rates of total denudation. Furthermore, we explore the role of soil water balance on regulating weathering fluxes in soils under water deficit regimes. Study sites are all located in the southern Betic Cordillera (SE Spain), and selected across a spatial gradient in climatic and topographic conditions.

SITE DESCRIPTION

Geomorphological and climatic setting of the Betic Cordillera

The focus of this study is on the eastern part of the Betic Cordillera located in Southeast Spain. The Betic Cordillera is composed by several E-W to SE-NW oriented mountain ranges rising up to 2000 m a.s.l (Figure 2.1), and is the product of tectonic compression and shortening arising from the convergence of the African and Eurasian plates [*Braga et al.*, 2003; *Jabaloy-Sánchez et al.*, 2007]. The internal zone of the Betic Cordillera has undergone a wide range of pressures and temperatures during the compression phase which began around 51 Ma, and is composed of three stacked geologic complexes. The Alpujarride and Nevado-Filabres complexes are the most upper ones and were exhumed during the early Miocene, while the Malaguide complex is largely covered and only outcropping in the northern part of the Sierra de las Estancias (Figure 2.1). All study sites belong to the Alpujarride and Nevado-Filabres complexes (Figure 2.1), and are underlain by low-grade metamorphic rocks. Mica-schist is the dominant lithology, but small outcrops of phyllite, interbedded quartzite veins and limestone are present [*ICONA*, 1988]. The mineralogy of the bedrock, as determined by XRD, is similar across the sampling sites and characterized by the presence of quartz (~30 %), muscovite (~25 %), clinochlore (<10 %), biotite and plagioclase [*Ameijeiras-Mariño et al.*, 2015].

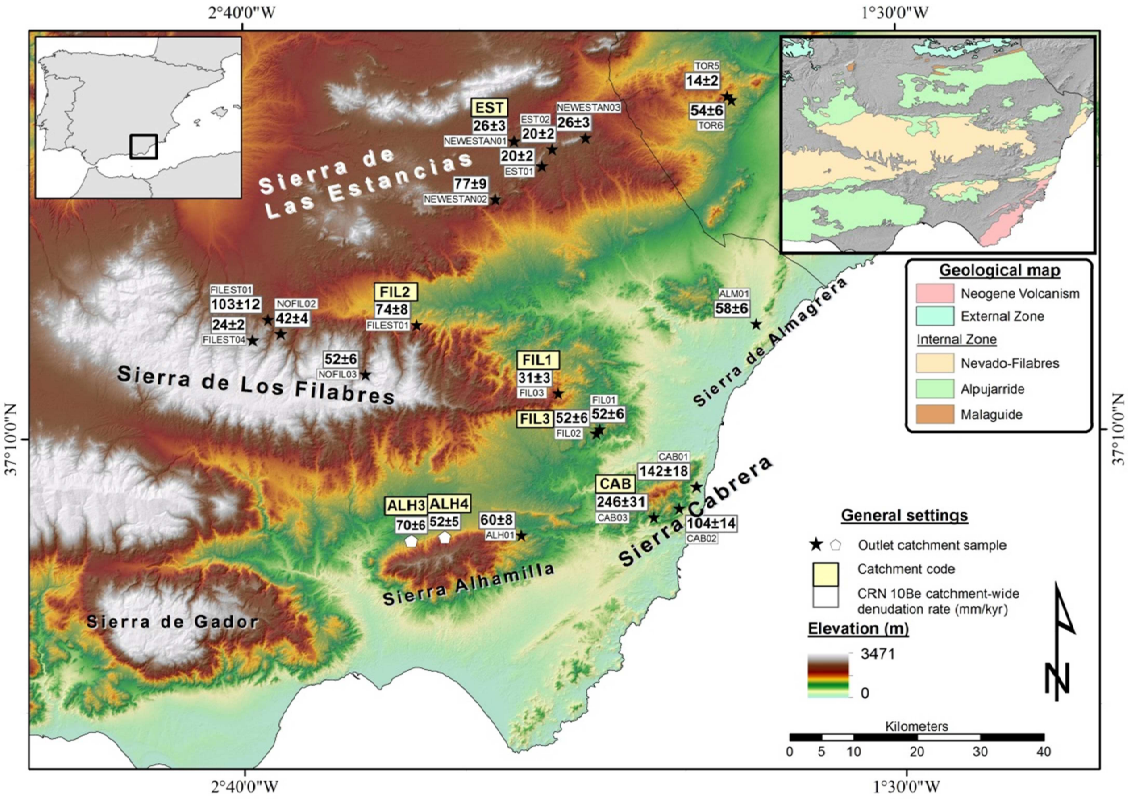

Figure 2.1: Overview topographic map of the Spanish Betic Cordillera, with inset map (left) showing its location within the Iberian Peninsula. The geostructural boundaries (inset on the right) were derived from the 1:400.000 geological map provided by the Junta de Andalucía [2004]. The location of sampling sites is indicated on the map, together with the corresponding ^{10}Be-derived denudation rates (±1 S.D.). (black stars refer to samples published in Bellin et al. [2014], while new samples are shown by white pentagons).

The modern topographic expression of the mountain ranges reflects the tectonic history of the Betic Cordillera [*Braga et al.*, 2003], with strong contrasts between the gently sloping hillsides of the Sierra de las Estancias and the steep highly dissected landscape of the Sierra Cabrera. In-situ produced ^{10}Be denudation rates for the eastern Betic Cordillera (Figure 2.1, *Vanacker et al.* [2014]) are ranging from 34 ± 24 mm/kyr for Sierra de las Estancias (n = 5), 54 ± 25 mm/kyr for Sierra de los Filabres (n = 8), 61 ± 9 mm/kyr for Sierra de Alhamilla (n=3), to 164 ± 74 mm/kyr for Sierra Cabrera (n = 3). The spatial pattern and magnitude of ^{10}Be-based denudation rates are consistent with tectonic uplift constrained by *Braga et al.* [2003] and *Masana et al.* [2005] based on marine deposits and trenching observations [*Bellin et al.*, 2014].

The present climate of the eastern Betic Cordillera can be defined as semi-arid (having a ratio of mean annual precipitation over potential evapotranspiration MAP/ET_p between 0.2 and 0.8 following *Estrela et al.* [1997]), and is characterized by warm summers and mild winters. The precipitation records present large inter- and intra-annual variability, and torrential rainfall with intensities of more than 200 mm per 24 h has been recorded [*De Luís et al.*, 2000]. Across the Betic Cordillera, the mean annual precipitation ranges between 275 and 425 mm, and generally increases with elevation. The mean annual temperature shows an opposite pattern, and ranges between 17 °C in Sierra Cabrera to about 12 °C in the Sierra de las Estancias (Table 2.1) [*García*, 2009]. Soil water availability is expected to show important spatial variability, as a result of strong spatial variation in mean annual potential evapotranspiration (ET_p): the *Junta de Andalucía* [2008] published average annual ET_p estimates based on the Thornthwaite method of 900 mm for Sierra Cabrera and 794 mm for Sierra de las Estancias for the period 1971-2000 [*Junta de Andalucía*, 2008]. The dominant vegetation type is matorral, characterized by a sclerophyllous and thorny vegetation [*Bellin et al.*, 2013]. Tree cover is very scattered with presence of some remnants of mesophilous taxons at higher altitudes.

Table 2.1: Location and characteristics of the sampled catchments.

Mountain range - Catchment code	**Latitude**	**Longitude**	**Surface area (ha)**[a]	**Min-Max altitude (m)**[a]	**Average slope gradient (°)**[a]	**Catchment-wide denudation rate (mm/kyr)**[b]	**Average annual precipitation (mm/yr)**[c]	**Mean annual temperature (°C)**[c]	**Lithology**[c]
Sierra Cabrera- CAB	37° 3' 5" N	1° 56' 25" W	198	243-756	28±8	246±31	275±25	17	Mica-schist
Sierra Filabres- FIL1	37° 13' 45" N	2° 5' 49" W	26	620-970	26±8	31±3	375±25	15.5	Mica-schist
Sierra Filabres- FIL2	37° 19' 37" N	2° 21' 30" W	94	699-1245	23±9	74±8	425±25	13.5	Mica-schist,phyllite
Sierra Estancias- EST	37° 35' 11" N	2° 10' 57" W	21	1142-1232	14±5	26±3	425±25	12.5	Mica-schist,phyllite

[a] Surface, altitude and average slope gradient are derived from the DEM [Junta de Andalucía, 2005].

[b] Catchment-wide denudation rates have been measured with CRN by Bellin et al. [2014].

[c] Average annual precipitation and temperature and lithology obtain respectively from ICONA [1988]; García [2009].

METHODOLOGY

Quantifying mass transfer coefficients, chemical depletion and total denudation

The intensity of weathering is here assessed as the fraction of mass lost by chemical weathering. We use a chemical mass balance where the elemental mass gains or losses in soil or mobile regolith compared to parent material are evaluated using immobile element concentrations [*Chadwick et al.*, 1990]. The element Zr is chemically immobile in a wide range of environmental settings, and becomes enriched during weathering and mineral dissolution [*Brimhall and Dietrich*, 1987; *Brimhall et al.*, 1992; *Riebe et al.*, 2001; *Kirchner et al.*, 2006]. Changes in individual elemental mass concentrations can then be described by tau values (τ_x, dimensionless ratios) or mass transfer coefficients that describe the fractional mass gain ($\tau_x > 0$) or loss ($\tau_x < 0$) relative to the composition of the parent material:

$$\tau_x = \frac{[X]_{soil} \times [Zr]_{rock}}{[X]_{rock} \times [Zr]_{soil}} - 1 \quad (2.1)$$

Where $[X]_{soil}$ and $[X]_{rock}$ are the concentrations of the individual element, X, in soil and parent rock respectively; and $[Zr]_{soil}$ and $[Zr]_{rock}$ the corresponding Zr concentrations. Tau values were calculated from bulk samples, and all elemental concentrations were adjusted by loss on ignition (~1000°C for 24h). This expression makes abstraction of possible influence of dust on soil chemistry. Although semi-arid climatic conditions are prevalent across the study sites, the potential impact of windblown dust on soil chemistry is assumed to be limited on the ridge tops that are typically exposed to wind and, as such, not favorable for dust deposition [*Díaz-Hernández and Rüoss*, 2009]. Given that soil profiles are all located on topographical convexities, we can assume that they mainly develop through in-situ weathering of the underlying parent material. For each profile, the parent rock chemistry was characterized by a bulk rock sample taken at the base of the mobile regolith. Although we acknowledge that a rock sample taken at great depth below the refusal layer should better represent the composition of the unweathered bedrock, this was technically not a feasible option given the remoteness of the study sites. Also, the use of rock samples from nearby rock outcrops or deep road cuts was not a viable alternative, given the large spatial variability in minor and trace elemental

concentrations of the mica-schist as shown by preliminary geochemical analyses.

According to previous weathering studies [*Riebe et al.,* 2003; *Dixon et al.,* 2009] this sampling method may introduce bias due to deep chemical weathering occurring in the deep saprolite. While deep chemical weathering has been demonstrated for regolith profiles developed on granite or charnockite rock series (formed > 1000°C), it is likely to be less the case for low-grade metamorphic rocks [*Jin et al.*, 2010] such as mica-schist, the dominant rock type in the Betic Cordillera, that differentiated at ~300°C following *Behrmann* [1983] and *Weijermars et al.* [1985].

The total fractional mass loss from chemical weathering in the soil can then be assessed from the chemical depletion fraction, *CDF*, for any given soil sample:

$$CDF = \left(1 - \frac{[Zr]_{rock}}{[Zr]_{soil}}\right) \tag{2.2}$$

The total denudation, *D*, of a soil surface is the result of mass lost by chemical weathering, *W*, and physical erosion, *E* (all in mm/kyr). Soils are considered to be in steady-state when the thickness of the mobile regolith is constant with time. In this case, the total denudation is roughly counterbalanced by soil production (mm/kyr), *P*, resulting from the conversion of bedrock into mobile regolith [*Heimsath et al.*, 1999; *Heimsath et al.*, 2001]. Soil production for topographic convexities, such as the study sites considered here, where lateral influx of soil or mobile regolith is negligible, can then be approximated by:

$$P = D = E + W \tag{2.3}$$

where the chemical weathering rate, *W*, can be quantified as the product of total denudation and chemical depletion fraction [*Riebe et al.,* 2001; *Riebe et al.*, 2004]:

$$W = D \times CDF = \left(1 - \frac{[Zr]_{rock}}{[Zr]_{soil}}\right) \tag{2.4}$$

Total denudation rates, *D*, are here derived from in-situ produced ^{10}Be concentrations in

soils. The soil surface denudation rates are determined from bulk soil samples taken at the base of the mobile regolith at depth z (cm). The measured ^{10}Be concentrations (at/g) were corrected for depth shielding using:

$$N_0 = N_{(z)} \times e^{\rho z / \Lambda} \quad (5)$$

where N_0 and $N_{(z)}$ are the ^{10}Be concentrations at the surface (z = 0) and depth (z), ρ is the density of soil or mobile regolith (g/cm³) and Λ is the path attenuation length of cosmic rays determined to be 160 g/cm² [*Gosse and Phillips*, 2001]. Topographic shielding was estimated using the procedure described in *Norton and Vanacker* [2009]. Soil surface denudation rates were then calculated using the CRONUS online calculator version 2.2 (http://hess.ess.washington.edu/, *Balco et al.* [2008]), using the time-dependent scaling laws proposed by *Dunai* [2000] (Table SI 2.3).

Sampling strategy

Four small catchments were selected within three Betic ranges: Sierra de las Estancias (EST), Sierra de los Filabres (FIL1, FIL2), Sierra Cabrera (CAB, Figure 2.1). The sites were selected to cover the range of denudation rates that were established for the Betic Cordillera by *Bellin et al.* [2014]. For each cordillera, catchments having rates close to the mean denudation rate were preferentially selected. Sites with clear evidence of drastic anthropogenic soil disturbances such as terracing or quarrying operations were avoided, as well as large catchments with complex topographic settings. In each catchment (or its close vicinity), two to three regolith profiles were sampled on exposed ridgetops to avoid the complexities of soil forming processes associated with lateral transport of fluids and soil particles along slope (Figure 2.2). Soil pits were excavated through the mobile regolith, and extended into parent material. All soils overlie fractured mica schist, and the mineral composition of soils and weathered rocks is not markedly different between sites, although slight variations exist [*Ameijeiras-Mariño et al.*, 2015]. Within each regolith profile, we sampled bulk soil material (0.5 – 1 kg) at 4 to 5 depth slices, and bedrock at the base of the pit.

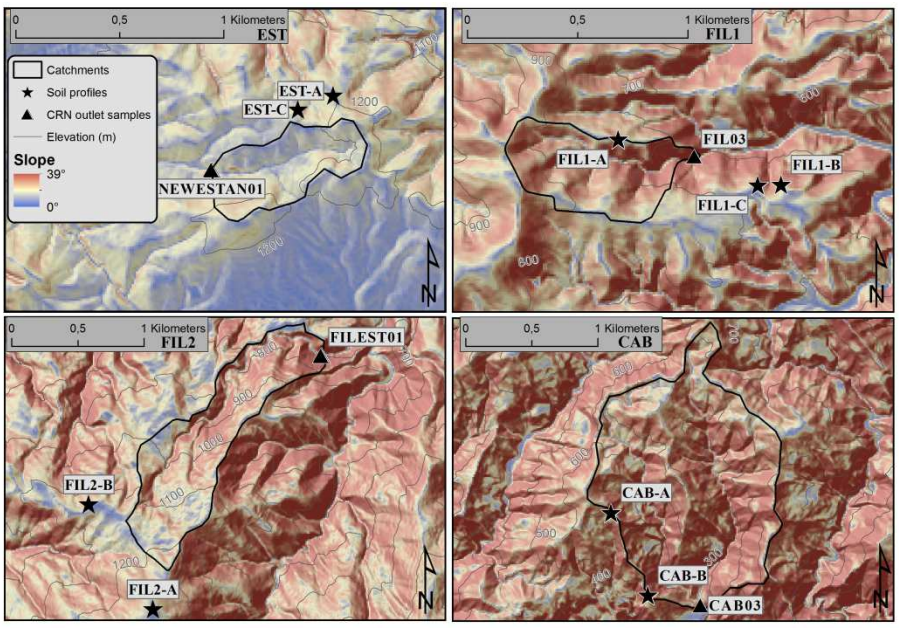

Figure 2.2: Topographic maps showing the location of the sampling sites at Sierra Cabrera (CAB), Sierra de los Filabres (FIL1, FIL2) and Sierra de las Estancias (EST). Note that all regolith profiles (black stars) are located at or near the ridge crest. Catchment-wide ^{10}Be denudation rates are derived from river sediments sampled at the outlet of the catchments (black triangle).

Analytical methods

In total, we analyzed 39 soil samples from nine different locations and 29 rock samples. All samples were air dried and sieved at 2 mm. The weathering rinds of rock samples were removed via sawing in order to measure, as far as possible, unweathered parent material. Then samples were crushed to break them into smaller pieces. Representative subsamples of soil, regolith and rock were powdered in an agate mill. Loss on ignition was recorded following combustion of an aliquot at 1000 °C for one day. Total elemental composition was determined by ICP – AES (Thermo iCAP 6000 Series) on 48 soil and rock subsamples after alkali fusion with Li-metaborate and Li-tetraborate at 1000 °C [*Chao and Sanzolone*, 1992].

Table 2.2: Cosmogenic radionuclide data of the regolith profiles.

Sample Code	Sierra	Latitude (°W)	Longitude (°N)	Altitude Elevation (m)	Soil Thickness (cm)	^{10}Be concentration ($\times 10^5$ at.g_{qtz}^{-1}) (± 1 σ)	^{10}Be denudation rates (mm kyr^{-1}) (± 1 σ)
EST-A	Estancias	2°10'36"	37°35'24"	1187	47	3.47±2.15	23±3
EST-C	Estancias	2°10'43"	37°35'22"	1187	58	1.09± 1.29	73±11
FIL1-A	Filabres	2°6'39"	37°13'47"	776	22	1.74± 1.38	34±4
FIL1-C	Filabres	2°6'14"	37°13'40"	776	17	1.67±1.03	35±4
FIL3-A	Filabres	2°3'21"	37°11'49"	585	14	3.52± 3.2	15±2
FIL2-A	Filabres	2°22'25"	37°18'35"	972	28	4.78± 2.41	14±2
FIL2-B	Filabres	2°22'44"	37°19'1"	972	28	4.29±2.22	15±2
CAB-A	Cabrera	1°56'53"	37°3'27"	525	19	0.59±0.79	95±14
CAB-B	Cabrera	1°56'42"	37°3'7"	525	18	0.46±0.83	109±22

Soil and sediment samples were processed for in-situ cosmogenic ^{10}Be analyses following the procedure described in *Vanacker et al.* [2007]. Samples were washed, dried and sieved, and the 500-1000 µm grain size fraction was used for further lab processing. Quartz minerals were extracted by magnetic separation and chemical leaching with weak acids (HCl, HNO_3 and HF) in an overhead shaker. Purified quartz samples were then leached with 24 % HF for 1 h to remove meteoric ^{10}Be, followed by total decomposition in concentrated HF. After spiking with ^{9}Be, the Beryllium in solution was extracted by ion exchange chromatography as described in *von Blanckenburg et al.* [1996a]. ^{10}Be/^{9}Be ratios were measured in BeO targets at ETH Zurich [*Kubik and Christl*, 2010]. The ratios were normalized to the ETH in-house secondary standard S2007N with nominal value of ^{10}Be/^{9}Be of 28.1×10^{-12} [*Kubik and Christl*, 2010] which is in agreement with a half-life of 1.387 Myr [*Chmeleff et al.*, 2010]. The ^{10}Be concentrations were corrected for laboratory blank (having a ^{10}Be/^{9}Be ratio of $0.48 \pm 0.14\times10^{-14}$), and the 1σ uncertainty estimates contain analytical errors from AMS measurement and blank error propagation (Table 2.2).

RESULTS

Soil profile development

There exist clear differences in soil profile development between the soils sampled at convex topographic positions in the Sierra Cabrera (CAB), Sierra de los Filabres (FIL1, FIL2) and Sierra de las Estancias (EST). Soils in Sierra Cabrera and Sierra de los Filabres are very thin (soil thickness between 20 and 30 cm), weakly developed and contain a large amount of rock fragments (Figure 2.3). They are classified as Regosols according to the FAO WRB soil taxonomy [*IUSS Working Group WRB*, 2014]. Soils in the Sierra de las Estancias are clearly more developed, and the rock upper boundary is observed at 45 to 60 cm depth (Figure 2.3). Two soil horizons can be observed: a light brown organic A horizon (0 to 15 - 20 cm) over a clay-rich B horizon (15 to 45 - 60 cm). The progressive change in color and texture from top to base of the profile suggests that soils are in a transitional stage of development, and can be defined as Cambisols. There are no apparent traces of calcrete or caliche in the study sites, which might be linked to the topographic position of the soil profiles (ridge crests). This is also confirmed by the chemical analyses that show very low concentrations of calcium (below 1 %) in the soil samples except in Cabrera (Supp. Information, Table SI 2.1).

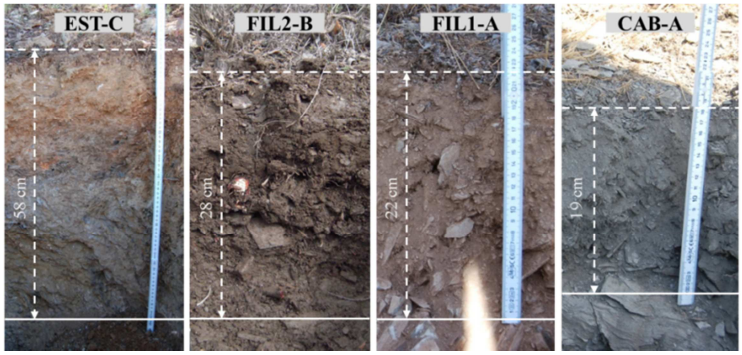

Figure 2.3: Illustration of the variation in soil development across the Betic Cordillera. The lower boundary of the mobile regolith is shown in white line and the soil profile code is indicated on the top of each picture

Chemical weathering intensity

Mass transfer coefficients, the so-called tau values (here determined by Zr enrichment), indicate that the major elements are depleted in the upper part of the soil profiles (Figure 2.4). This is particularly the case for easily weatherable elements such as K (Figure 2.4A), Na, and Ca that are strongly depleted in most topsoils, with exception of FIL2 and CAB where Ca-depletion of topsoil is not clear (Supp. Information, Table SI 2.2). The depletion profiles are generally consistent with the increase in clinoclore and muscovite content with depth. The Si element is carried by many primary and secondary minerals from the silicate group which are relatively resistant to chemical weathering. Therefore, its concentration tends to increase at the top of the soil profile compared to other elements. Tau values for Si show a range of depletion values between -0.28 and 0.13, which is less than for the major cations, but which still represents significant depletion relative to Zr. (Figure 2.4C). Fractional mass losses of K are highest for soils of the Sierra de las Estancias, where the depletion of Al in the topsoil is also most pronounced (Figure 2.4): for example, the fractional mass loss in topsoil (at 13 cm depth) in EST-A equals -0.82 for K and -0.74 for Al. In contrast, the weakly developed soils of Sierra Cabrera (CAB-A and CAB-B), show higher (i.e. less negative, τ-K = -0.27 and -0.15) τ-K values than those of Sierra de las Estancias, and display no major change in Al concentrations with depth (Figure 2.4B).

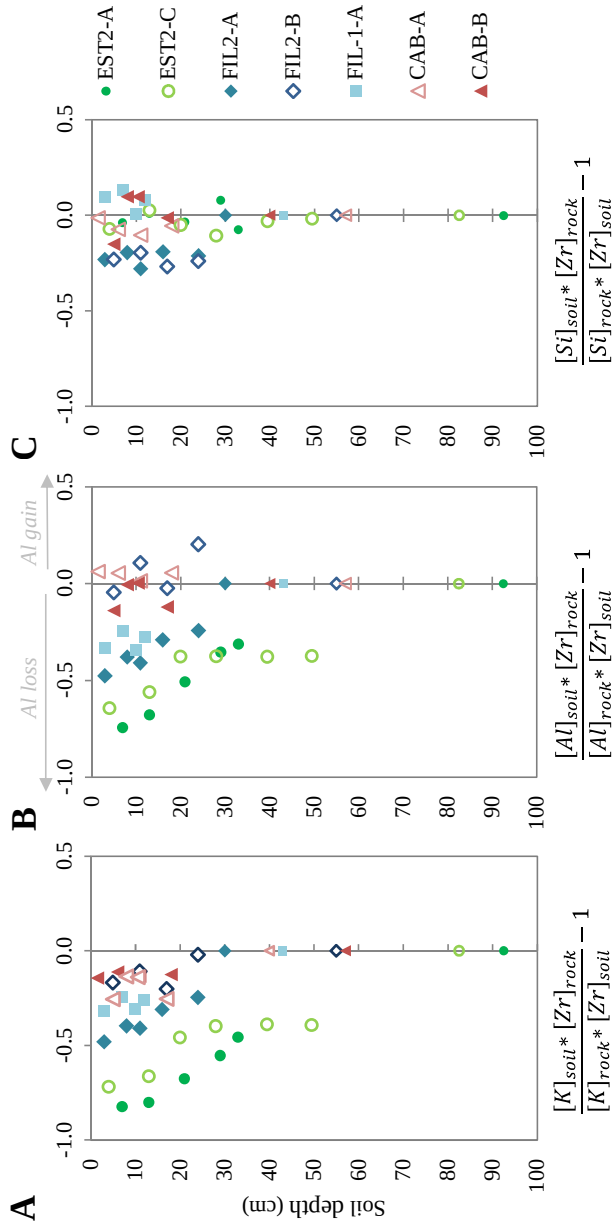

Figure 2.4: Variation of mass gain (positive values) and loss (negative values) due to chemical weathering across the Betic Cordillera (CAB, FIL1, FIL2 and EST) for three major elements (K, Al and Si). The values plotted at greatest depth are from rock samples.

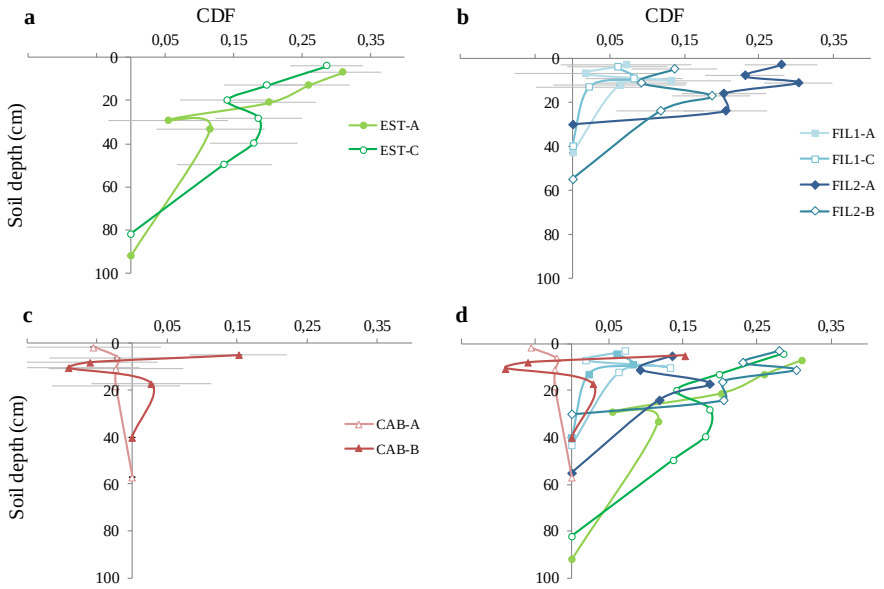

Figure 2.5: Weathering intensity of eight regolith profiles, as measured by the chemical depletion fraction (CDF, here referred to Zr). Profiles are sampled in the (A) Sierra de las Estancias, (B) Sierra de los Filabres, and (C) Sierra Cabrera. The variation in chemical depletion between soil profiles from the eight sites is shown in D. Error bars can be seen in figure 2.5a-c but have been omitted on 5d for visual clarity.

Chemical depletion fractions of topsoil material in the 9 soil profiles vary between ~0.05 and 0.30, indicating that the chemical weathering accounts for ~5 % to 30 % of total denudation in the Betic Cordillera. Most of the CDF curves, corresponding to the weathering intensity, show a progressive increase from bottom to surface (Figure 2.5). This gradual increase of the intensity of chemical weathering with decreasing depth is expected, as chemical weathering processes depend on the presence of organic acids, water, CO_2, and roots that increase the mineral surface area by fragmentation and dissolution, and was reported earlier for soil CDF profiles in Puerto Rico [*Riebe et al.*, 2003], San Gabriel mountains [*Dixon et al.*, 2012] and Sri Lankan highlands [*Hewawasam et al.*, 2013].

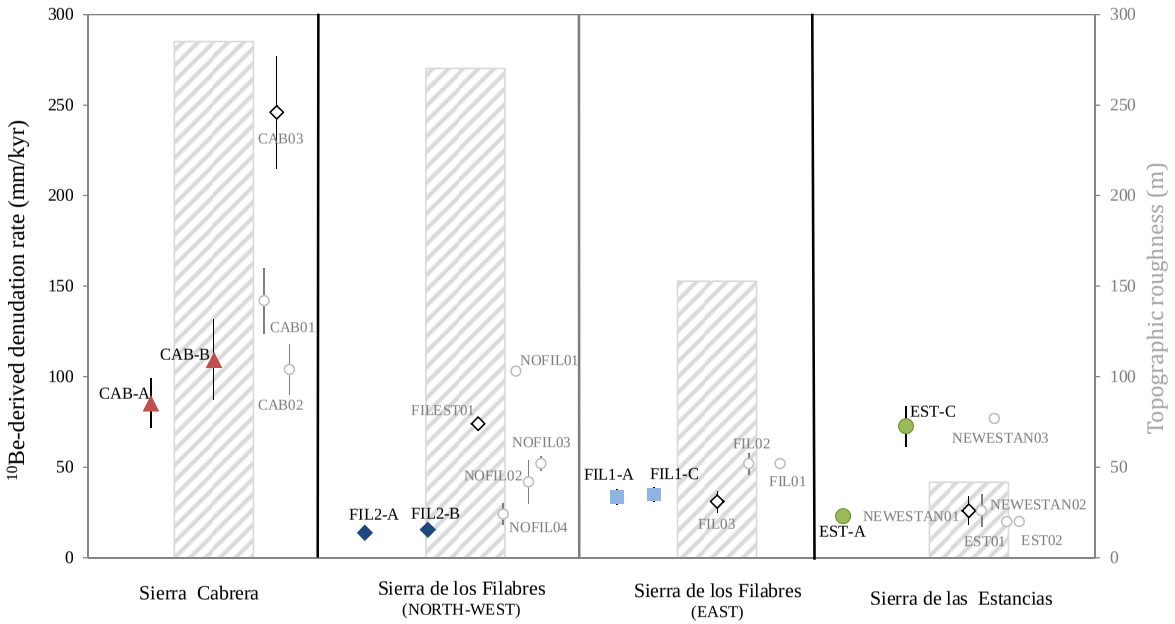

Figure 2.6: Denudation ates at hillslope and catchment scale in the Betic Cordillera. The surface denudation rates were measured from in-situ produced ^{10}Be concentrations (CRN) in regolith profiles at topographic convexities (colored symbols). Catchment-wide denudation rates of the four sampled catchments were determined from CRN in fresh alluvial material (black diamonds). Additional information on catchment-wide denudation rates from nearby sites are taken from Bellin et al. [2014] (grey dots). The topographic roughness of the four sampling sites is here assessed by the catchment relief (difference between maximum and minimum altitude, m), and is plotted on the second Y axis (grey bars).

Chemical weathering intensity varies widely across the eastern Betic Cordillera, with highest soil chemical depletions measured in the Sierra de las Estancias ($CDF_{(EST-A)}$ = 31 %, $CDF_{(EST-C)}$ = 29 %), intermediate values in Sierra de los Filabres ($CDF_{(FIL1-C)}$ = 6 %, $CDF_{(FIL1-B)}$ = 12 %, $CDF_{(FIL1-A)}$ = 7 %, $CDF_{(FIL2-B)}$ = 14 %, and $CDF_{(FIL2-A)}$= 28 %) and lowest depletions in Sierra Cabrera ($CDF_{(CAB-A)}$ < 0 %, $CDF_{(CAB-B)}$ = 15 %, Figure 2.5). In the most developed soils of Sierra de las Estancias, the vertical redistribution of major elements is most pronounced, with highest CDF and fractional mass losses of K, Na and Al in the upper 20 cm of the soil profile. This change in soil chemical properties roughly occurs at the transition between the pedogenic horizons from the soil profile descriptions (Figure 2.5). The near-absence of vertical homogenization of the upper soil horizons is quite remarkable, and suggests that soil turnover and mixing through e.g. bioturbation is limited. In contrast, in the weakly developed soils of the Sierra de los Filabres and Sierra Cabrera, the elemental depletion profiles for the upper 25 cm of soil (τ-plots as shown in Figure 2.4) are flat, and the observed variation in CDF may either result from soil mixing and analytical uncertainty on the CDF values, for instance, related to variation in the parent rock chemistry.

Total denudation rates

Total denudation rates, derived from in-situ produced ^{10}Be concentrations, of the sampled soil profiles range between 14 and 109 mm/kyr (Table 2.2). The denudation rates are considered to be low compared to other convergent mountain ranges [*Cyr and Granger*, 2008; *Ouimet et al.*, 2009; *DiBiase et al.*, 2010; *Cyr et al.*, 2010]. There is no direct evidence of strong anthropogenic perturbations to the sampled soil profiles, despite intense land use change since the Mid-Holocene following multiple phases of human occupation and land abandonment in southern Spain [*Bellin et al.*, 2013]. Strong anthropogenic disturbance of soils due to accelerated erosion, ploughing or levelling is expected to result in (1) a high spatial heterogeneity in soil surface denudation rates from local differences in the degree and intensity of anthropogenic disturbance, and (2) physical mixing of the upper soil horizons as a result of ploughing. The denudation rates of the two most northern Sierras (Sierra de las Estancias and Sierra de los Filabres) are significantly lower than the rates in Sierra Cabrera [*Bellin et al.*, 2014]. For three out of four catchments (CAB, FIL1 FIL2), the denudation rates of various ridge crests agree within uncertainty (Figure 2.6). This suggests that erosion rates are rather uniform for a given topographic and geomorphological setting. The denudation rate of EST-C (73 ± 11 mm/kyr) is slightly higher than expected for the Sierra de las Estancias, based on

comparative analyses of denudation rates both at the soil profile ($D_{(EST-A)}$ = 23 ± 3 mm/kyr) and catchment scale (Figure 2.6). As soil profile descriptions of EST-A and EST-C did not show any evidence of soil truncation, this could eventually be an artifact resulting from deep soil mixing.

DISCUSSION

Denudation rates at hillslope and catchment scale

Catchment-wide denudation rates across the Betic Cordillera, as measured by *Bellin et al.* [2014], display a similar magnitude and spatial pattern as the rock uplift rates in the region. They are highest in Sierra Cabrera (104 to 246 mm/kyr), intermediate in Sierra de los Filabres and lowest in Sierra de las Estancias (77 to 20 mm/kyr, Figure 2.6). The strong correlations between catchment-wide denudation rates, mean hillslope gradient and local relief [*Bellin et al.* [2014]] imply that hillslopes are actively adjusting to tectonic uplift by slope adjustments. While the pattern of in-situ produced ^{10}Be denudation rates at the ridge crests is similar (with higher denudation soil rates in Sierra Cabrera, and systematically lower values in the other mountain ranges), there is clearly less variation in the magnitude of the soil denudation rates of ridge crests (Figure 2.6). Soil denudation rates are generally less than or equal to catchment-wide denudation rates measured at the outlet of small basins, which further supports our hypothesis that soils on the hill crests are not strongly disturbed by local anthropogenic disturbance. The difference between soil and catchment-wide denudation is largest for highly dissected catchments with pronounced topographic relief such as the Sierra Cabrera (Table 2.1, Figure 2.6), where soil denudation rates of ridge crests are about 120 mm/kyr lower than the average catchment-wide denudation rate; but is statistically indistinguishable for the eastern part of the Sierra de los Filabres and Sierra de las Estancias. This might be an indicator that the rate of change in denudation rate with distance downslope depends on the topographic relief of the catchment, or an indication of the importance of soil particle trajectories in conditioning ^{10}Be depth profiles in unmixed soils as suggested by *Anderson* [2015].

Topographic and geomorphic control on chemical weathering

Chemical weathering accounts for ~5 to 30 % of the total mass lost by denudation

(Figure 2.5). Average chemical depletion fractions (CDF) of the topsoil (i.e. upper 15 cm of soil material) are negatively correlated with total surface denudation (Figure 2.7A), and catchment-wide denudation rates (not shown). Based on the general agreement between catchment-wide denudation and long-term uplift as reported by *Bellin et al.* [2014], we can infer that weathering depletions are negatively associated with tectonic uplift rates. The relationship between CDF and physical erosion rates shows a similar negative trend.

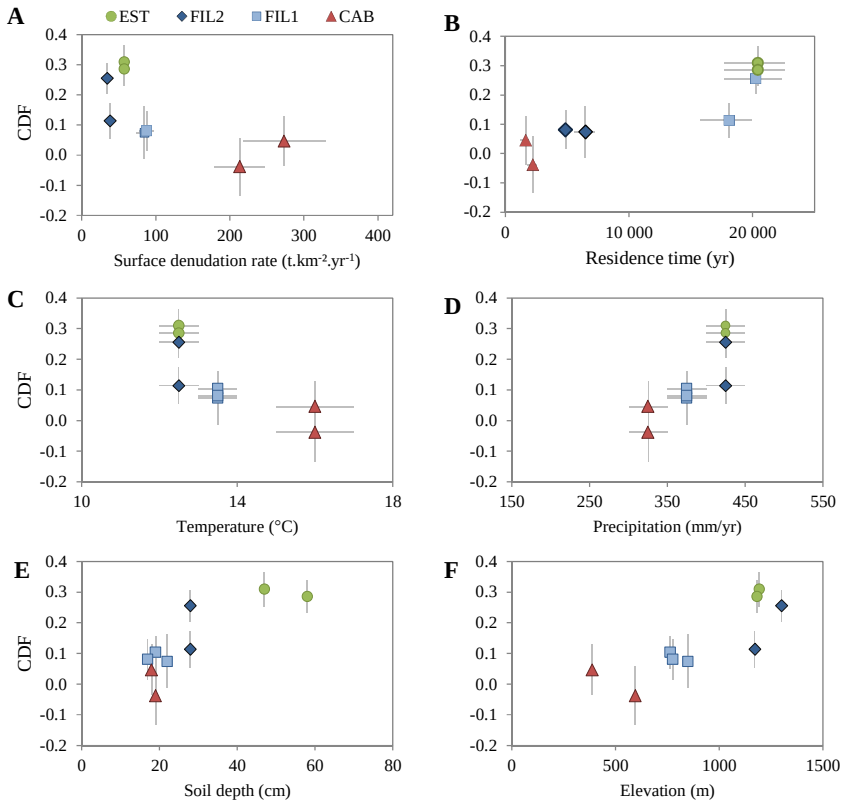

Figure 2.7: Average chemical weathering extent of topsoil (as measured by the chemical depletion fraction) decreases with (A) total denudation rate, and increases with soil (B) residence time. Climatic proxies such as the mean annual temperature (C) and mean annual precipitation (D) are strongly related to chemical weathering losses. The climate proxies are highly elevation-dependent (F). Chemical weathering losses are highest for thicker soils (E), and decrease nonlinearly with depth. Note that the surface denudation rate of EST-C has been considered as equal to EST-A (see text).

Chemical weathering extent is positively related to soil thickness (Figure 2.7E), although the observed relation is strongly nonlinear. The intensity of weathering reactions is dependent of the intensity of biological activity enhanced by vegetation development,

association with mycorrhizal fungi, pH, organic acids and water content [*Amundson*, 2007; *Quirk et al.*, 2012]. For thin soils without diagnostic horizons, a wide variation in chemical depletion fractions is observed for a given soil thickness. These thin, stony soils are characterized by high denudation rates (Figure 2.5), and soil residence times are estimated at 2000 years by dividing the soil thickness by denudation rate. With increasing soil thickness, the CDF increments towards a maximum value of about 30 %. Given the negative relation between soil thickness and denudation rate, soil residence time strongly increases with soil thickness up to ~20 000 years (Figure 2.7B).

Climatic control on chemical weathering

Climatic patterns in the Betic Cordillera are strongly associated with altitude and slope orientation. Sites at higher altitudes are characterized by lower air temperature and higher precipitation. Our data show that weathering losses increase with mean annual precipitation and decrease with mean annual temperature (Figure 2.7C, D). Even if these climatic data are only representative for the last 30 years, we assume that the climatic patterns (characterized by elevation dependence of temperature and precipitation) were similar in the past. In a comparison of Holocene vegetation change and climate reconstruction from both high elevation and lower elevation sites among the Betic Cordillera, *Anderson et al.* [2011] show that, for the most part, the main features of Holocene vegetation change are roughly similar and synchronous with a progressive aridification since the beginning of the Holocene. While we cannot rule out that other elevation-dependent factors (such as total denudation rates) may influence weathering processes, we hypothesize that climate affects weathering processes in this semi-arid region mainly through water availability in the soil system. A similar observation was made by *Rasmussen et al.* [2010] and *Ferrier et al.* [2012] who suggested that regolith temperature may have no effect on chemical weathering processes when the soil system is under water deficit. The negative relationship between weathering extent and temperature that we observe here might either result from decreasing soil biotic activity at high ambient (and regolith) temperatures, or a statistical artifact as temperature is strongly associated with elevation, and topographic roughness in the Betic Cordillera.

In semi-arid mountain ranges, the high solar radiation together with reduced precipitation strongly controls water availability in the vadose zone. This situation is most stringent in the Sierra Cabrera, where the mean annual potential evapotranspiration (ET_p = 903 mm/yr) largely exceeds the mean annual precipitation (*MAP* = 275 mm/yr, Table 2.1);

leading to acute soil water deficits during 6 to 7 months of the year [*Junta de Andalucía*, 2008]. The situation is considerably more advantageous for vegetation growth in the Sierra de las Estancias, with an ET_p of 794 mm/yr and *MAP* of 425 mm/yr [*Junta de Andalucía*, 2008]. With increasing water availability, more moisture becomes available in the soil system for living organisms that enhance mineral dissolution through their respiration and secretion of acids and enzymes, and for mechanical rock breakdown and soil mixing through e.g. plant root wedging or burrowing. Although no field data are available from soil solution chemistry on solute fluxes in the region, we theoretically expect element leaching and solute fluxes to increase with soil water availability and fluid residence times [*Rasmussen et al.*, 2010; *Maher*, 2011].

Coupling between chemical weathering and total denudation

Our discussion is focused on the relation between chemical weathering extent (CDF) and total denudation (*D*), as these two variables were determined independently in this study. The observation that chemical weathering extent (1) increases with soil thickness, and (2) decreases with increasing denudation rates (and tectonic uplift) is generally assumed to be characteristic of kinetically limited weathering processes [*Ferrier and Kirchner*, 2008; *Gabet and Mudd*, 2009; *Lebedeva et al.*, 2010]. Previous studies have provided evidence for kinetic weathering processes in rapidly eroding landscapes only [e.g. *Norton and von Blanckenburg*, 2010; *Dixon et al.*, 2012]; where physical erosion processes reduce soil thickness and limit mineral residence time [*Stallard and Edmond*, 1983]. Our data confirm the hypothesis put forward by *Ferrier and Kirchner* [2008] that kinetically limited regimes can occur in a wide range of erosional settings, where denudation rates are high relative to the maximum soil production rate. We consider mineral residence time and water balance in the soil system as the two most important elements constraining chemical weathering processes. Mineral residence time is here observed to be nonlinearly related to denudation rates: an increase in denudation rate leads to a strong nonlinear decrease in soil residence time, given the negative relationship between soil denudation and soil thickness (Figure 2.7E). The negative correlation between chemical weathering extent (CDF) and total denudation rates (*D*) observed for the Betic Cordillera is consistent with earlier work in kinetically limited regimes by e.g. *Norton and von Blanckenburg* [2010], *Larsen et al.* [2014] (Figure 2.8A).

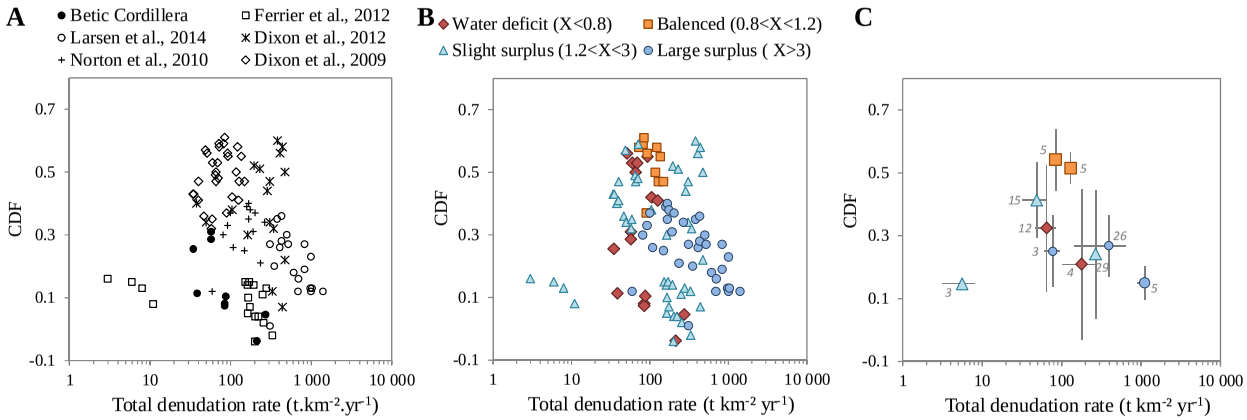

Figure 2.8: Empirical relationships between chemical weathering extent, total denudation rate and soil water balance for a wide variety of environmental conditions. Chemical weathering extent (CDF) plotted against in-situ ^{10}Be derived denudation, with annotation of (A) the original source of information, (B) a proxy of soil water balance ($X = MAP/ET_p$ see text). (C) Average chemical weathering extent (±1 SD) per log bin of total denudation rate (mean ±1 SD, with numbers referring to the amount of observations in each bin). Note that we plot the original values as reported in Dixon et al. [2009]; Norton and von Blanckenburg [2010]; Dixon et al. [2012]; Ferrier et al. [2012]; Larsen et al. [2014], with no further adjustments for AMS standardization or nuclide production rates, as detailed information on topographic shielding and/or production rate schemes was not available for all studies. Chemical weathering losses reported in Dixon et al. [2009]; Dixon et al. [2012]; and Ferrier et al. [2012] refer to the maximum chemical weathering extent of the top layer of the mineral soil, while the values reported in Norton and von Blanckenburg [2010] and Larsen et al. [2014] refer to the average chemical weathering extent of the bulk soil. In our plot, data points from Rapid Creek [Larsen et al., 2014] are not included, as they clearly plot outside the range of most observational datasets on soil denudation rates (B).

Water balance in the soil system depends on local climatic settings, and strongly controls element leaching and soil solute fluxes [*White et al.*, 2009; *Rasmussen et al.*, 2010; *Maher*, 2011]. According to previous work by *Riebe et al.* [2004], 67 to 84 % of the observed variance in weathering intensities can be explained by precipitation and temperature for supply-limited processes, while *West et al.* [2005] suggest that silicate weathering is controlled by temperature and runoff in kinetically limited regimes only. On the other hand, *Rasmussen et al.* [2011] report that there is no significant relation between temperature and Na chemical weathering in their study case, but rather pointed to denudation and precipitation as the dominant controls on weathering. We explore the role of soil water balance on chemical weathering (surface and subsurface CDF), by plotting chemical depletion functions against total (^{10}Be derived) denudation rates for a worldwide data set covering a wide range of soil hydrological conditions (Figure 2.8A).

As no detailed information is available to reconstruct local water balances, we calculate a first order proxy of soil water balance by dividing mean annual precipitation, *MAP*, by potential evapotranspiration, ET_p (Figure 2.8B), thereby assuming that local runoff is minimal. ET_p was calculated with the Thornthwaite method [*Palmer and Havens*, 1958], and is based on latitude (defining the day length) and mean monthly temperature. Temperature data from the weather stations in the close neighborhood of the study sites are derived from NOAA for US sites, and national climate databases for Switzerland, and New Zealand. For the Spanish sites, mean monthly gridded values for the period 1971-2000 are available from the *Junta de Andalucía* [2008]. Four states of soil water balance are then defined as follow: water deficit ($MAP/ET_p < 0.8$), balanced ($0.8 < MAP/ET_p < 1.2$), slight surplus ($1.2 < MAP/ET_p < 3$), and large surplus ($MAP/ET_p > 3$). Our data suggest that soils "under balanced conditions" are generally characterized by high chemical weathering losses (Figure 2.8C). In contrast, soils under water deficit or with large surplus show systematically lower chemical weathering extents for a given range of denudation rates. Soil development in regions with high denudation rates and large moisture excess ($MAP/ET_p > 3$) is rather limited by prolonged waterlogged conditions that constrain element leaching and soil solute fluxes. There obviously exists a wide scatter in the dataset that limits further interpretation, and confounding variables such as lithology, rock rheology, vegetation cover and density may affect the interpretation of statistical associations. Comparative studies covering a wider range of environmental conditions (Figure 2.8C), are needed for advanced statistical analyses. Besides, a modelling framework such as the one proposed by *Maher and Chamberlain* [2014] is very useful to fully explore the role of soil water hydrology on chemical weathering losses across a wide range of climatic conditions.

CONCLUSION

Understanding the relation between chemical weathering and physical erosion is crucial for understanding long-term landscape evolution and dynamics of nutrient cycling in soil systems. The present paper constrains chemical weathering rates for a semi-arid environment, characterized by strong soil water deficit during the prolonged dry season. As such, it helps to fill a gap in existing datasets by supplying new data on chemical weathering losses for soil water limited conditions. In the southern Betic Cordillera, in-situ produced ^{10}Be denudation rates display a similar magnitude and spatial pattern as the rock uplift rates in the region. Total denudation rates are low, and range between 14 and 109 mm/kyr. Chemical weathering losses account for ~5 to 30 % of the total mass lost by denudation. Soil weathering extents increase (nonlinearly) with soil thickness and decrease with increasing surface denudation rates, consistent with kinetically limited or -controlled weathering.

Our data suggest that soil residence time and water availability limit weathering processes in dry environmental conditions, which has not been validated previously with field data. An important implication of this finding is that climatic regimes may strongly regulate soil weathering by modulating soil solute fluxes. Therefore, it will become essential for chemical weathering and landscape evolution models to include soil water and solute fluxes in soil development models. To validate such models across a wide range of soil hydrological conditions, it is crucial to expand existing field datasets on soil solid and solute fluxes into less explored climatic and lithological settings.

Chapter III

Topographic imprint of chemical weathering and soil development in deeply weathered subtropical soils (southern Brazil)

Based on:

Schoonejans, J., V. Vanacker, S. Opfergelt (in prep.) Topographic imprint of chemical weathering and soil development in deeply weathered subtropical soils (southern Brazil)

ABSTRACT

In soil-mantled landscapes, the development of the regolith results of in-situ weathering, atmospheric input and downhill transport of weathering products. Along hillslopes, the lateral transport of weathering products is accomplished through diffusive and concentrated fluxes which redistribute weathering products over the hillslope. In this study, spatial variability in chemical mass fluxes and weathering intensity was studied along two toposequences with similar climate, lithology and vegetation but different slope morphologies. This allowed us to isolate the topographic imprint on chemical weathering and soil development. The toposequences have convexo-concave slope morphology, and eight regolith profiles

were analysed involving the flat upslope, steep midslope and flat toeslope part. The chemical mass fluxes of our regolith profiles show vertical transfers and accumulation in the illuviation horizon which is typical for Alisol/Acrisol. At the upslope positions, the weathering intensities and total chemical mass losses are systematically lowest: the weathering process results from in-situ weathering of the parent material. Mass transfers and chemical weathering intensities increase towards the footslope of both toposequences and result of in-situ weathering and aggradation of transported – and weathered - regolith. Our data also indicate that soil profiles are significantly more weathered in the steeper toposequence. The data presented here quantify the role of topography on soil development and provide reliable data for soil landscape models.

INTRODUCTION

The regolith mantle is defined as the thin layer of unconsolidated material overlaying bedrock that contributes to shape the Earth's surface [*Brantley et al.*, 2006; *Anderson et al.*, 2007]. The development of the regolith mantle in a landscape is the result of in-situ weathering, atmospheric input and downhill transport of weathering products [*Mudd et al.*, 2013]. Bedrock weathering - the physical and chemical transformations of rock to soil - contributes to the vertical development of the regolith layer through downward propagation of the weathering front. Lateral transport of soil particles, aggregates and solutes by diffusive and concentrated particle and solute fluxes result in lateral redistribution of weathering products over the hillslope. Long-term evolution of soil mantled hillslopes is controlled by tectonics [*Riebe et al.*, 2001], water availability [*Rasmussen et al.*, 2010; *Schoonejans et al.*, 2016b], biota [*Roering et al.*, 2010], and local topography [*Yoo et al.*, 2007]. Various numerical schemes for explicit and quantitative modelling of soil landscapes have been developed [*Mudd and Furbish*, 2006; *Brantley et al.*, 2008; *Vanwalleghem et al.*, 2013; *Finke et al.*, 2015] to simulate the long-term evolution of soil mantled landscapes. While soil landscape models vary widely in complexity, their widespread application at the landscape scale is currently limited by two aspects. First, soil landscape models commonly simulate in-situ bedrock weathering using a depth-dependent soil production function where the weathering rate depends on the depth below the surface [*Ahnert*, 1977; *Heimsath*, 1997]. Field data that underpin depth-dependent weathering are typically derived from landscape convexities where vertical movement of soil particles, aggregates and solutes define soil formation and development, and steady-state regolith thickness can be assumed [*Schoonejans et al.*,

2016a]. The soil production function not necessarily applies at the landscape scale, where lateral fluxes of soil constituents along the toposequence influences soil development. Second, the downslope movement of soil particles, aggregates and solutes over the hillslope not only depends on local topography but also on the thickness of the regolith mantle [*Furbish*, 2003; *Roering*, 2008]. Field data have shown that a simple relation between diffusive transport rates and hillslope gradients is restricted to landscape convexities [*West et al.*, 2013]. Existing soil landscape models often make abstraction of the spatial variation in soil properties, by assuming constant regolith thickness and constant rates of soil production [*Green et al.*, 2006]. In order to extend the models to the landscape scale, the downslope transport of weathering products should also be related to the regolith thickness [*Heimsath et al.* 2005].

In this study, we aim to expand the empirical basis on long-term soil evolution at the landscape scale through a detailed study of soil weathering in subtropical soils. Spatial variability in chemical mass fluxes and weathering intensity was studied along two toposequences with similar climate, lithology and vegetation but different slope morphologies. This allowed us to isolate the topographic imprint on chemical weathering and soil development. The soil observatory is located in southern Brazil, and representative for deeply weathered soils developed on rhyodacitic rocks in humid subtropical conditions. This work builds on earlier work by *Jin et al.* [2010] on the quantification of mineral weathering and elemental transport along toposequences from the Shale Hill Critical Zone Observatory.

METHODOLOGY

Study sites

The study area is located in the central part of the Rio Grande do Sul State in southern Brazil on the southern border of the so-called Serra Geral Formation belonging to the Paraná Magmatic Province, the second largest continental flood basalt province [*Frank et al.*, 2009]. The volcanic plateau contains mainly basic volcanic rocks (basalt) but also acid rocks (rhyolite-dacite) [*Bellieni et al.*, 1986; *Montanheiro et al.*, 2004] from the late Mesozoic (137-127 Ma, *Turner et al.* [1994]) (Figure 3.1). The humid subtropical climate is characterized by oceanic influences and absence of a marked dry season [*Alvares et al.*, 2013]. Mean annual rainfall is comprised between 1700 and 1800 mm,

with a peak between September and October (30% of the total rainfall amount), and mean annual temperature ranges between 14 and 18 °C [*Alvares et al.*, 2013; *Minella et al.*, 2014]. The natural vegetation can be described as deciduous tropical forest with remnants of native *Araucaria angustifolia* trees. Agricultural expansion has led to a massive conversion of the native forests to agricultural fields, but patches of natural forest are still remaining. The soil observatory is situated in the vicinity of Ilopolis city (28°55' W; 52°07' S; Figure 3.1), and located in a subtropical forest. The catchment is underlain by rhyodacitic rocks belonging to the Palmas-Santa Maria group. The bedrock has an aphanitic texture with 69 to 71 wt% of SiO_2, < 0.87 wt% of TiO_2 and < 0.21 wt% of P_2O_5 [*Polo and Janasi*, 2014]. The XRD mineralogical analysis indicates that sanidine belonging to the feldspar group is the most abundant mineral (45-55%), followed by very fine grained quartz (~38%) that is set in matrix with hematite, goethite and clays (~8%). Soils are classified as Alisol and Acrisol according the FAO system [*IUSS Working Group WRB*, 2014] with pH (H_2O) values between 4.7 and 5.9.

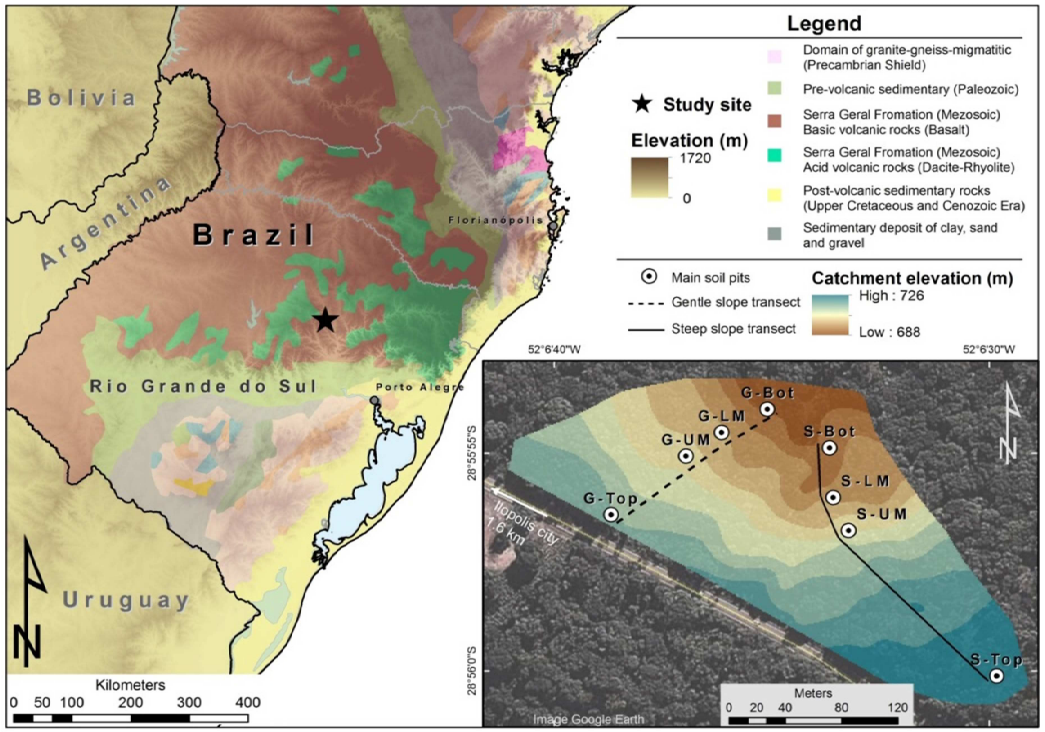

Figure 3.1: Topographic map of southern Brazil, with its location shown on the inset (upper left). Geostructural boundaries are derived from [Renner et al., 2011; IBGE, 2016]. The location of the Critical Zone Observatory is indicated by a black star. The topography of the CZO is given in the lower right panel, and the regolith profiles are located by white circles.

Within the soil observatory, two toposequences were selected for the soil landscape analysis: a north-east facing slope having an average slope gradient of 8° (referred to as "gentle slope"), and a north-west facing hillslope having an average slope gradient of 13° (referred to as "steep slope"; Figure 3.1 and 3.2). Soil pits were excavated at the upslope, upper middle, low middle and toeslope topographic position. Pits were dug to the refusal layer (saprolite or bedrock) or to 2 meters deep. The soil profiles were sampled by taking depth slices. A total of 67 regolith, 8 saprolite, and 1 bedrock samples were taken (Table S1). The regolith is here defined as the loose, unconsolidated layer overlaying the bedrock, and is progressively weathered over time; and the saprolite as the chemically weathered rock that retains the original rock structure and fabric. The fresh bedrock was sampled in a nearby outcrop. All samples were dry-sieved at 2 mm.

Quantifying chemical fluxes and weathering intensities

The mass fluxes and the intensity of chemical weathering are here quantified using a chemical mass balance approach and based on earlier work of *Brimhall and Dietrich* [1987], *Chadwick et al.* [1990], *Brimhall et al.* [1992], *Egli and Fitze* [2000], *Anderson et al.* [2002], *Heckman and Rasmussen* [2011] and *Brantley and Lebedeva* [2011]. The mass balance model allows quantification of elemental mass gains or losses in the regolith, by comparing the elemental composition of the weathered material and fresh bedrock. Our calculations are based on the mass balance model as published by *Brimhall and Dietrich* [1987], and rests on the idea that the mass of an element, j, in the weathered regolith, V_w, is equal to its mass in the parent material, V_p, plus the mass gained or lost through weathering processes, $m_{j,flux}$:

$$\frac{1}{100}\left(V_w \rho_w C_{j,w}\right) = \frac{1}{100}\left(V_p \rho_p C_{j,p}\right) + m_{j,flux} \quad (3.1)$$

Where, ρ_w and ρ_p correspond to the bulk densities of respectively the weathered regolith and parent material and $C_{j,w}$ and $C_{j,p}$ to the concentrations of an element, j, in the weathered regolith (w) and in the parent material (p) (in weight percent). To account for non-isovolumetric weathering, it is necessary to quantify the changes in volume when the parent material (V_p) is transformed into regolith (V_w). The strain ε_i (dimensionless ratio) can be calculated as a function of depth z (cm), and accounts for volumetric expansion (>0) or collapse (<0) of the regolith relative to the parent material by referring to a chemically immobile element:

$$\varepsilon_i(z) = \frac{\rho_p C_{i,p}}{\rho_w C_{i,w}} - 1 \tag{3.2}$$

where, $C_{i,w}$ and $C_{i,p}$ are the concentrations of an immobile element, i, in the regolith and parent material. The elements *Ti* and *Zr* are considered to be chemically immobile in a wide range of environmental settings, and are typically enriched in the regolith as a result of chemical weathering and mineral dissolution [*Brimhall and Dietrich*, 1987; *Riebe et al.*, 2001; *Kirchner et al.*, 2006].

Mass transfer coefficients (τ_j) are calculated to account for changes in the immobile element concentration ratio as a result of removal or addition of mobile elements. The relative change in elemental mass, $\tau_j(z)$ (dimensionless ratio) of a mobile element, j, gained ($\tau_j > 0$) or lost ($\tau_j < 0$) in the regolith at depth *z*, can be derived as:

$$\tau_j(z) = \frac{C_{j,w}\, C_{i,p}}{C_{j,p}\, C_{i,w}} - 1 \tag{3.3}$$

By combining Eq. 3.2 and 3.3, we can calculate the mass flux of element *j* that is depleted or added to the regolith per unit area, $m_{j,flux}$ (kg/m²) following *Egli and Fitze* [2000] and *Brantley and Lebedeva* [2011]:

$$m_{j,flux} = \rho_p C_{j,p} \int_0^{L_w} \frac{\tau_j(z)}{(\varepsilon_i(z) + 1)}\, dz \tag{3.4}$$

where $\tau_j(z)$ and $\varepsilon_i(z)$ are resp. the mass transfer coefficient and strain at depth *z* in the regolith that are integrated over the entire thickness of the regolith, L_w, (m) using a spline function (SRS1, Cubic Spline). As we do not have data on deep saprolite weathering as e.g. *Dixon et al.* [2012], our mass fluxes are only representative for regolith weathering. Hence, the mass fluxes are minimal estimates of the total elemental fluxes. To compare elemental mass fluxes between regolith profiles with different thicknesses, the mass fluxes were normalized, $m_{j,flux\,n}$ (kg/m²), to a regolith thickness of 1 m.

The elemental mass fluxes can be summed over all elements (j = 1 to n) to obtain the

total weathering flux over the entire regolith profile (Figure 3.2), M_{tot} (kg/m²):

$$M_{tot} = \sum_{j=1}^{n} m_{j,flux\ n} \tag{3.5}$$

The chemical depletion fraction ($CDF_{(z)}$) is used, as a complementary tool, to quantify the chemical weathering intensity at depth (z) of the regolith profile. The expression is here corrected for strain and $C_{j,p}$ is expressed in terms of percent oxide (wt %):

$$CDF_{(z)} = -\frac{1}{100}\sum_{j=1}^{n} \frac{\tau_j(z)\ C_{j,p}}{(\varepsilon_i(z)+1)} \tag{3.6}$$

Similar as for the mass fluxes (equation 3.4), $CDF_{(z)}$, can be integrated over the thickness of the regolith profile using a spline function (SRS1, Cubic Spline) in order to obtain CDF_{tot}.

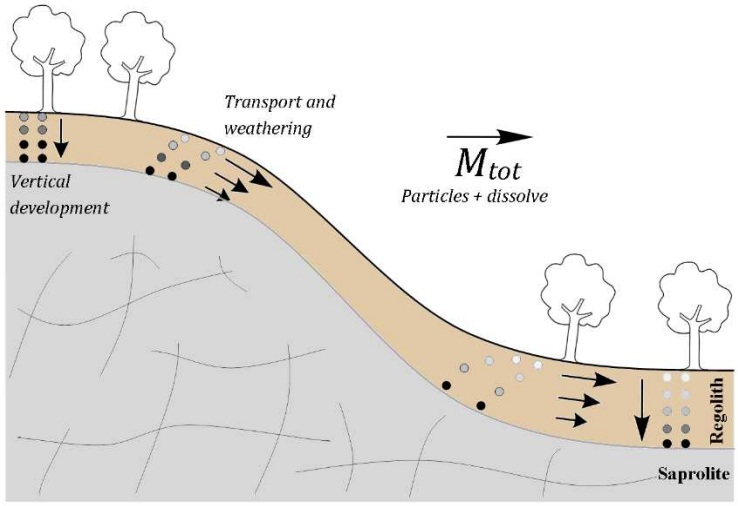

Figure 3.2: Development of the regolith mantle along a toposequence. At the upslope position, vertical movement of soil particles, aggregates and solutes is dominant. At the shoulder, toeslope and backslope position, soil development results from the chemical weathering of in-situ parent material and incorporated weathering products from upslope. At the toeslope position, the accumulation of weathering products in the basal concavity strongly influences soil formation and development. (Black arrows schematize the total mass fluxes, and the length of the arrow is indicative for the magnitude of the mass flux). The dots illustrate the weathering products, and are filled according to their weathering degree, with black dots representing fresh bedrock and white dots representing highly weathered material.

Along the toposequences, weathering products are transported downslope. The residual weathered products can continue to weather chemically during transport (Figure 3.2). The chemical depletion of a given regolith profile along the hill slope is not only dependent on in-situ weathering of parent material but also on lateral input of weathering products.

Chemical analyses of soil and rock samples

The total elemental composition of our samples was measured from bulk samples by Inductively Coupled Plasma Atomic Emission spectroscopy (ICP-AES at UCLouvain) following the analytical methods described in *Schoonejans et al.* [2016b]. Results were adjusted for loss on ignition (~1000°C for 24h). The accuracy of the concentration measurements was verified with the reference material BHVO-2 (Basalt, Hawaiian Volcanic Observatory, Wilson [1997]) and is evaluated at respectively <3% for major and ~5% for minor elements. The parent rock chemistry was characterized from three bedrock samples taken in outcrops close to the sampling site (mean value). Given the low variability in elemental concentrations of the bedrock in the study area (see Supp. Info. Table SI 3.1), we consider that the average composition of the unweathered rock samples adequately represents the geochemistry of the parent material.

RESULTS

Development of the regolith mantle

Soils in the study area are all well developed. The color of the soil profiles recurrently varies from (top to bottom) organic dark brown (0 to 5 cm), light brown (10 to ~50 cm), dark brown (~50 to ~65 cm), to light brown (below 60 cm) (Table 3.1). Strain values reveal that the regolith has undergone volumetric expansion relative to the parent material (ε_{Ti}>0 for 7/8 profiles), but differences in soil volume change exist between topographic positions.

For the two toposequences, physical soil properties vary systematically over the hillslope. The thickness of the regolith mantle increases progressively with the distance from the crest: the profiles are 50 to 100 cm deep at the upslope positions and more than

150 cm deep in the basal concavities of the toeslopes (Table 3.1). While only two soil horizons can be identified in the upslope part, four soil horizons are identified in the toeslope profiles. Soil volumetric changes are highest for the upslope profiles, with strain values above 0.70. The total strain decreases systemically with distance from the crest, and the rate of decrease is highest for the steep toposequence (Table 3.1). The total chemical depletion of the regolith profiles shows a similar pattern with highest values for the basal concavities, and maximum values for the steep toposequence. In addition, it is important to notice that the profile on the shoulder of the steep slope (S-UM) is poorly developed compared to the other profiles, with a shallow thickness (~50 cm) and only two soil horizons (Table 3.1 and Figure 3.3).

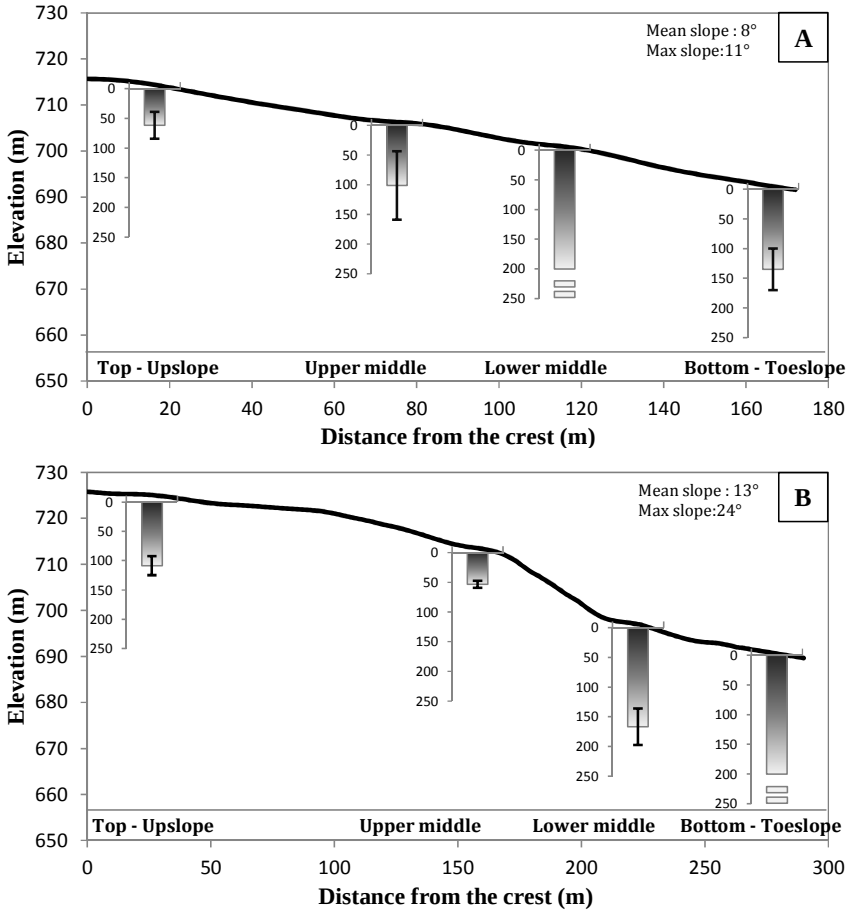

Figure 3.3: Topographic representation of the two toposequences with A gentle hillslope, and B steep hillslope. The depth (cm) of the regolith profile is shown on the Y-axis, with the mean depth and standard deviation derived from three replicate pits (n= 3). Double horizontal boxes indicate that the soil-saprolite boundary was deeper than 2 m.

Table 3.1: Main characteristics of the regolith profiles, indicating the thickness of the regolith, the soil development and total strain (normalized by depth). The soil description mentions the number of soil horizons (SH), the soil texture and color (DB: dark brown, LB: light brown, R: reddish; O: organic).

General code	**Simplified code** (used in this paper)	**Thickness** (cm)	**Soil description** (Number of soil horizons - texture - color)	**Total strain** (unitless)	CDF_{tot} (unitless)
Gentle slope					
ILGTR3	G-Top	70-90	2-3 SH : Silt - Silt loam : DBO - LB	0.73	0.23
ILGUMR2	G-UM	160	2-4 SH : Silt - Silt Clay : DBO – LB – DB - B	0.26	0.39
ILGLMR2	G-LM	200	4 SH : Silt : DBO – LB – B - LBR	0.42	0.29
ILGBR1	G-Bot	110	3-4 SH : Silt - Silt loam : DBO – LB – B - R	0.29	0.34
Steep slope					
ILSTR2	S-Top	120	4 SH : Silt - Silt loam : DBO - LB - DB - LB	0.74	0.26
ILSUMR2	S-UM	50	2 SH : Silt : DBO - LBR	0.62	0.26
ILSLMR2	S-LM	200	4 SH : Silt - Silt loam : DBO – LB – DB - LB	0.13	0.43
ILSBR2	S-Bot	200	4 SH : Silt - Silt loam : DBO - LB - DB - LB	-0.03	0.59

Variation in chemical weathering intensity

For both toposequences, chemical weathering accounts for 25 to 60% of the total denudation of the regolith mantle (Figure 3.4). The change in weathering intensity with depth - as measured by the $CDF_{(z)}$ - can be described by a bell-shaped curve: the maximum value is observed between 20 and 50 cm deep coinciding with the illuviation horizon. The chemical weathering intensity varies with topographic position, which is well illustrated by the mean $CDF_{(z)}$ ratios from the illuviation horizons. There is a general increase of the weathering intensity with the distance from the crest: the weathering intensity accounts for 28 % of the total denudation in the upslope profile (G-Top) of the gentle toposequence and increases to 41, 37 and 38 % for resp. the upper middle (G-UM), lower middle (G-LM) and bottom position (G-Bot). The change in weathering intensity along the toposequence is even more pronounced for the steep toposequence with values of 28%, 27%, 55% and 59% for resp. S-Top, S-LM, S-UM and S-Bot.

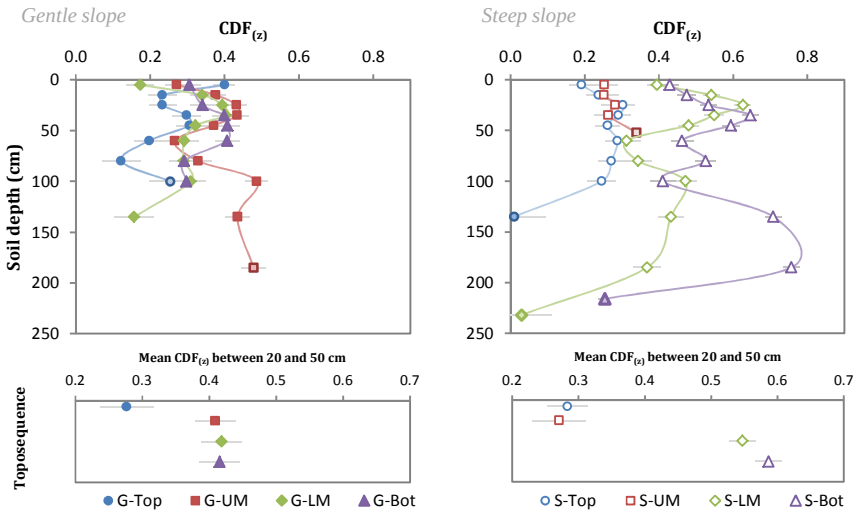

Figure 3.4: Chemical weathering intensities (CDF) for the four topographic positions in the gentle (left) and steep (right) toposequence. The lowest samples (larger symbols) correspond to saprolite samples. The two lower panels show the mean CDF for the upper 20 to 50 cm.

Mass transfer coefficients, $\tau_j(z)$, that describe the fractional mass gains or losses relative to the composition of the parent material indicate that most of the major elements are depleted in the regolith profiles with $\tau_j(z)$ values below 0 (Figure 3.5 and Supp. Info. Table SI 3.2). Strong depletion of the basic cations (Ca, Na, K, Sr, Ba) is observed with Tau values below -0.9. throughout the regolith profiles. The depletion is slightly lower at the surface suggesting external input from dust or biota. The mass transfer coefficient of Si ranges around -0.4 througout the soil profile, and increases in the saprolite (Figure 3.5). For Al and Fe, mass transfer coefficients are negative in the topsoil, but show a remarkable increase between 50 and 80 cm depth, suggesting a decrease of the weathering intensity and/or translocation of Al and Fe through migration of secondary minerals (clays) and accumulation of total organic matter [*Trigalet et al.*, in prep.] in the Bt horizon. The losses of Al increase with increasing distance from the crest, and the variation of τ_{Al} values with depth is more pronounced for the lower middle and toeslope positions (Figure 3.5). Also, the regolith profiles of the steep toposequence show higher elemental mass losses compared to the gentle toposequence.

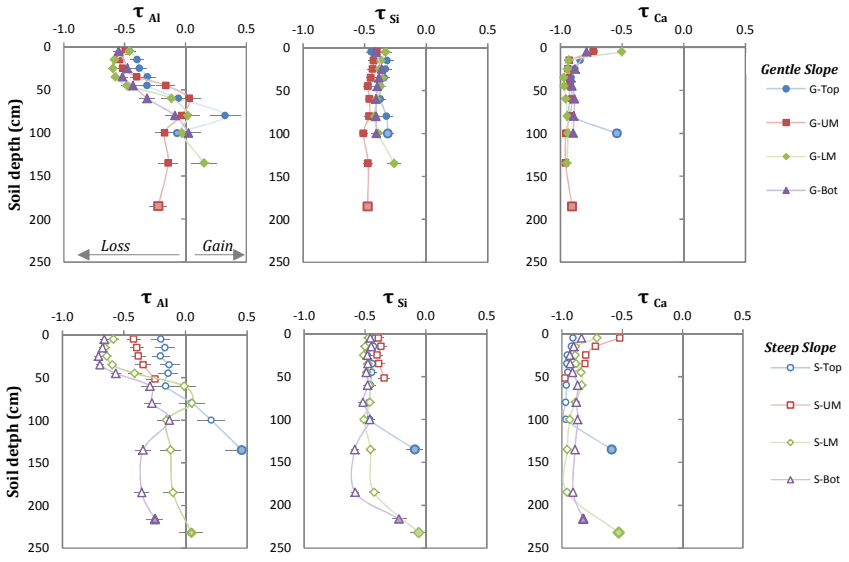

Figure 3.5: Mass transfer coefficients (and 1 st. dev.) for three major elements (Al, Si, Ca) as a function of depth. The upper panels show the four profiles of the gentle toposequence, while the lower panels show the profiles of the steep toposequence. The lowest samples (larger symbols) correspond to saprolite samples. The conservative element that was used to calculate the mass transfer coefficients is here Ti.

Quantification of chemical mass fluxes

In table 3.2, thickness normalized chemical mass fluxes ($m_{j,flux\,n}$) are systematically negative for the major elements (sum of oxides + LOI = <99 % of the total weight). The chemical mass fluxes from the upslope profiles are comparable to the weathering fluxes presented in *Caner et al.* [2014] for a soil profile developed on a rhyodacitic bedrock. Along the gentle and steep toposequence, the $m_{j,flux\,n}$ increases with the distance from the crest to become maximum at the toeslope position. This observation points to major elemental losses through vertical and lateral particle and solute fluxes. Silica is the most abundant element in the parent material (Si_2O average concentration: 71 ± 0.6 %, Table SI 3.1), and has the highest chemical mass losses (-232 to -555 kg/m²) that can reasonably be related to the weathering of feldspars (plagioclase and sanidine). The losses of Ca, K, Mg and Na are important with a mean $m_{j,flux\,n}$ of respectively -8, -62, -4 and -27 kg/m² for the eight profiles, given the relatively low concentrations of CaO (0.7 ± 0.4 %), K_2O (4.4 ± 0.9 %), MgO (0.6 ± 0.3 %) and Na_2O (2.1 ± 0.2 %) in the parent material. Aluminum and Iron are more abundant in the bedrock (respectively 12 ± 0.4 and 5 ± 0.7 %), but show low overall mass losses in the regolith profiles (mean $m_{Al,flux\,n}$: -32 and mean $m_{Fe,flux\,n}$: -8 kg/m²). The low mobility of Al and Fe can be

explained by the formation of strong complexes of iron and aluminum oxides and clays [*Ritchie*, 1995].

The total mass fluxes (M_{tot}) are lower for the upslope (S-Top and G-Top) than for the toeslope profiles, and the total mass losses generally increase with distance from the crest (Table 3.2). This observation is consistent with the pattern of chemical weathering intensities presented above, and suggests progressive loss of major and minor elements away from the hill crests. The highest mass losses are observed for the steep toposequence: M_{tot} of the lower middle and bottom slope position is about 31 to 41% higher for the steep toposequence compared to the gentle toposequence.

Table 3.2: Chemical mass fluxes (kg/m²) of the eight regolith profiles. Mass fluxes are here normalized for a regolith thickness of 1 m, to allow comparison between profiles.

Regolith profiles	**Distance from crest (m)**	**Thickness normalized mass flux ($m_{j,flux\,n}$)[a]**									M_{tot}
Gentle		Al	Fe	Si	Ca	K	Mg	Na	Mn	P	∑
G-Top	0	-19.6 ± 9	-6.7 ± 3	-181.3 ± 28	-6.4 ± 2	-50.8 ± 17	-2.3 ± 1	-22.0 ± 7	-0.3 ± 0.0	-0.5 ± 0.1	-290.0 ± 66
G-UM	60	-28.8 ± 9	-3.8 ± 6	-318.7 ± 59	-9.1 ± 3	-68.5 ± 22	-4.2 ± 1	-29.9 ± 9	-0.4 ± 0.1	-0.7 ± 0.2	-464.3 ± 108
G-LM	90	-23.6 ± 12	-6.0 ± 5	-222.4 ± 27	-8.1 ± 2	-58.4 ± 17	-3.2 ± 1	-26.0 ± 7	-0.2 ± 0.1	-0.6 ± 0.1	-348.5 ± 70
G-Bot	125	-39.0 ± 9	-12.6 ± 2	-353.8 ± 34	-8.2 ± 2	-65.6 ± 20	-3.8 ± 1	-28.7 ± 8	-0.1 ± 0.1	-0.6 ± 0.1	-412.5 ± 76
Steep											
S-Top	0	-6.2 ± 7	-6.5 ± 2	-217.8 ± 43	-6.7 ± 2	-50.7 ± 18	-3.2 ± 1	-21.9 ± 7	-0.5 ± 0.1	-0.4 ± 0.1	-314.0 ± 80
S-UM	140	-38.8 ± 5	-8.3 ± 2	-196.2 ± 31	-5.3 ± 1	-40.2 ± 11	-3.4 ± 1	-18.3 ± 5	0.7 ± 0.4	-0.3 ± 0.1	-310.0 ± 56
S-LM	165	-32.9 ± 14	-7.9 ± 5	-346.3 ± 69	-9.8 ± 3	-72.0 ± 23	-4.6 ± 1	-31.8 ± 9	-0.3 ± 0.1	-0.9 ± 0.2	-506.3 ± 125
S-Bot	200	-68.0 ± 11	-12.2 ± 6	-465.7 ± 93	-11.4 ± 3	-90.2 ± 29	-6.0 ± 1	-39.1 ± 11	-0.4 ± 0.1	-1.1 ± 0.2	-694.1 ± 155

[a]: The elements represented in this table account for more than 99% of total oxides (LOI included). We do not include saprolite samples because of a lack of bulk density data of saprolite samples.

DISCUSSION

Development of the regolith mantle along hillslope

In the subtropical soils of southern Brazil, the regolith is deeply weathered as shown by the strong depletion in Ca, K or Na cations and leaching of Si (Figure 3.5 and Table 3.2). This observation is consistent with earlier studies from tropical and subtropical regions by *Asio and Jahn* [2007], *Krasilnikov et al.* [2005] and *Caner et al.* [2014]. The redistribution of Al and Fe within the regolith profiles is clearly illustrated in Figure 3.5 (Table SI 3.2), with a bell-shaped form including a maximum fractional mass loss between 20 and 50 cm (correlated with $CDF_{(z)}$, Figure 3.4) and a decrease of the mass loss below 50 cm. Redistribution and translocation of clay minerals, aluminum and iron hydroxides and organic compounds are typical for Alisols and Acrisols, that develop in humid tropical and subtropical regions [*Caner et al.*, 2014].

Along the toposequences, lateral transport of weathering products along the hillslope influences soil development (Table 3.1). In the upslope areas, the development of the regolith mantle is regulated by soil erosion and in-situ weathering of the bedrock. Along the hillslope, weathering products are transported downslope by gravity and diffusive processes, and are progressively weathered during transport. With increasing distance from the crest, the regolith thickens, the total strain decreases and soil horizon development is more pronounced. In the basal concavities, weathering products accumulate and the regolith mantle thickens. Its chemical and mineralogical composition is largely dependent on in-situ weathering and the flux of weathering products from upslope. The chemical weathering indices that are reported above support this hypothesis: the thickness normalized mass losses ($m_{j,flux\,n}$) are 1.5 to 2 times lower for the upslope profiles compared to the toeslope profiles (Table 3.2). Moreover, the downslope enrichment of immobile elements (Figure 3.6) also supports the hypothesis of progressive weathering of the regolith along the hillslope. Figure 3.6 illustrates that the downslope regolith profiles have a higher concentration in immobile elements (Ti and Zr) than profiles located in the upslope parts of the toposequences. The enrichment in Ti and Zr is maximum in the illuviation horizons (between 20 and 50 cm) as indicated by the crossed dots in Figure 3.6. It is important to note that Zr seems to be less conservative than Ti in the weathering profiles of this subtropical environment: the regolith samples systematically plot under the theoretical enrichment line. This is less the

case for the saprolite samples where the enrichment respects the Zr/Ti ratio ratio measured in the unweathered bedrock. This argument supports our selection of Ti as the index element in order to quantify the chemical fluxes in the toposequence. Despite this choice, we do not ignore that Zr and Ti can become mobile in highly weathered tropical soils as suggested by *Melfi et al.* [1996]; *Kurtz et al.* [2000] and *Du et al.* [2012] .

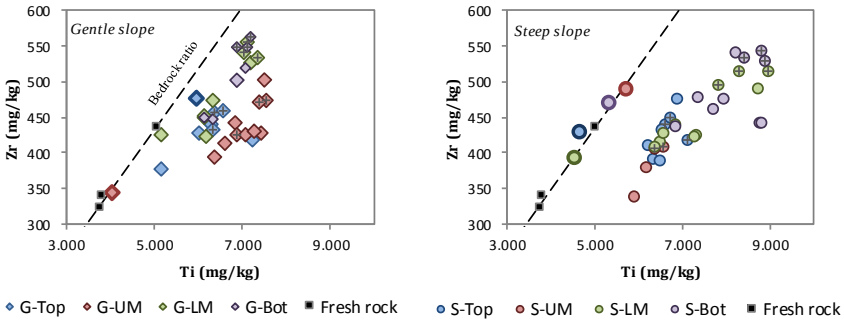

Figure 3.6: Concentrations of Ti and Zr in regolith and saprolite (thick line border) samples of the gentle (left) and steep hillslope (right). Dashed line corresponds to a theoretical enrichment of Ti and Zr if both elements were strictly immobile in the weathering profiles. Samples from the illuviation horizon (between 20 and 50 cm) are marked by a cross.

It is important to precise that the mass fluxes do not take into account the weathering losses in the saprolite which can be significant under sub-tropical climates [i.e. *Ferrier et al.*, 2010]. Following *Dixon et al.* [2012] , the chemical depletion fraction (CDF, referred to Ti) has been used to estimate the total fractional mass losses in the saprolite. Our data reveal that the CDF of the saprolite is about 35 % for the gentle sloping toposequence, and between 20 to 30% for the steep toposequence (Suppl. Inf. Table SI 3.3). The differences in saprolite CDF values can imply differences in water infiltration and percolation in the critical zone, but detailed geophysical data are needed to verify this hypothesis. Due to a lack of deep saprolite samples, it is currently not possible to correct for saprolite weathering.

The effect of local topography on regolith development

Along hillslope, the chemical weathering intensity of the regolith profiles increases with distance from the crest. In contrast to the upslope positions, the soils in the basal concavities develop on in-situ and transported regolith. The mass transfer coefficients (i.e. $\tau_{Al,w}$), CDF_{tot} and total mass fluxes (M_{tot}) indicate that the regolith profiles are more weathered at the bottom of the steep toposequence than the gentle one. This results

from the combination of in-situ weathering of the parent material and weathering of transported weathering products (soil particles and solutes fluxes) as illustrated in Figure 3.2.

While the chemical weathering extent on the slope convexities (the upslope profiles) is similar for the steep and gentle toposequence, there is a clear difference in the rate of increase of the chemical weathering extent with distance from the crest. The latter is most pronounced for the steep toposequence. This observation is rather contra-intuitive: the steepest hillslope is characterized by the highest soil erosion rates (see *chapter V*), and highest soil production rates if we assume steady-state soil thickness. Faster erosion rates and shallower thicknesses mean that the minerals move more rapidly through the regolith mantle of the steep toposequence, leading to shorter residence time of minerals in the regolith mantle along hillslope. This is typically associated with a lower degree of weathering following numerical approaches by e.g. *Ferrier and Kirchner* [2008] or experimental data by e.g. *Dixon et al.* [2012].

The exact reason for the stronger increase of chemical weathering extent for the steeper toposequence is not yet clear. Our observations of soil particle, nutrient and water fluxes in the regolith mantle suggest that this might be related to differences in surface hydrology between the two toposequences, with deeper water circulation at the gentle toposequence. The fact that the saprolite layer in the gentle toposequence shows higher degree of chemical weathering is one argument for the deeper weathering on the gentle toposequence. Additional measurements of water and solute fluxes in the regolith and saprolite layer are necessary to fully understand the complexity of deep weathering in the critical zone. Such relation between chemical mass fluxes and curvature or slope gradient has often be described in the literature [i.e. *Selby*, 1992; *Mudd et al.*, 2013; *Schaetzl*, 2013] or in conceptual models [*Mudd and Furbish*, 2004; *Yoo et al.*, 2009] but has less often be reported the field except in more temperate climate by (i.e.) by Yoo et al. [2011] in Northern Sierra Nevada (California) and by *Green et al.* [2006] in South-East Australia. The data presented in this study could help to better constrain the landscape evolution models.

CONCLUSION

The critical zone observatory of Rio Grande do Sul provides new insights in the soil

development on deeply weathered volcanic rocks. Two toposequences with a convexo-concave slope morphology were selected in a 2.9 ha watershed, and eight regolith profiles were analysed involving the flat upslope, steep midslope and flat toeslope part. The regolith profiles show evidence of redistribution and translocation of iron, aluminum and clay particles, which is typical for Alisols and Acrisols. At the upslope positions, the weathering intensities and total chemical mass losses are systematically lowest: the weathering process results from in-situ weathering of the parent material. Mass fluxes, including particle and solute fluxes, increase with distance from the crest; and are highest in the basal concavities where regolith profiles are thickened as a result of sediment accumulation. The mass fluxes in the downslope profiles are the result of in-situ weathering and aggradation of transported – and weathered - regolith. Our data show a clear topographic imprint on soil development. The increase of chemical weathering extent along hillslope is highest for the steep toposequence, suggesting that topography enhances soil particle, aggregate and solute fluxes.

Chapter IV

Coupling uranium series and ^{10}Be cosmogenic radionuclides to evaluate steady-state soil thickness in the Betic Cordillera

Based on:
Schoonejans, J., V. Vanacker, S. Opfergelt, M. Granet and F. Chabaux, Coupling uranium series and ^{10}Be cosmogenic radionuclides to evaluate steady-state soil thickness in the Betic Cordillera, (2016a) Chemical Geology, Available online 4 April 2016, ISSN 0009-2541, http://dx.doi.org/10.1016/j.chemgeo.2016.03.030.

ABSTRACT

The Critical Zone is the near-surface environment where interactions between the atmosphere, lithosphere, hydrosphere and biosphere take place. The development of the regolith mantle is controlled by the downwards propagation of the weathering front into the bedrock and denudation at the surface of the regolith by mass movements, water and wind erosion. When the removal of surface material is approximately balanced by the production of weatherable material at the bottom of the regolith profile, the soil system is assumed to be in steady-state. Although recent literature on chemical weathering often assumes that soils have a steady-state thickness, the concept has rarely been validated with empirical field data. In this study, we present and compare analytical data from two independent isotopic techniques: in-situ produced cosmogenic nuclides and U-series disequilibria to

constrain soil development under semi-arid climatic conditions. Three soil profiles were sampled across the Betic Ranges, at the ridge crest of zero-order catchments with distinct topographic relief, hillslope gradient and ^{10}Be-derived denudation rate. Soil production rates determined based on U-series isotopes (^{238}U, ^{234}U, ^{230}Th and ^{226}Ra) are of the same order of magnitude as ^{10}Be-derived denudation rates, suggesting steady state soil thickness, in two out of three sampling sites. Our results show the potential of a combined U-series disequilibria and in-situ ^{10}Be isotope approach to evaluate steady-state soil thickness. Our study also illustrates the frontiers in applying U-series disequilibria to track soil production in environments characterized by weak soil development.

INTRODUCTION

On Earth, the Critical Zone extends from the top of the canopy down to the groundwater table, and encompasses organisms, soil, rock, air and water [*National Research Council*, 2001]. It is also the near-surface environment where interactions between the atmosphere, lithosphere, hydrosphere and biosphere take place [*Brantley*, 2006; *Anderson*, 2007]. Within the Critical Zone, the development of the regolith mantle is controlled by the downwards propagation of the weathering front into the bedrock and denudation at the surface of the regolith by mass movements, water and wind erosion [*Heimsath*, 1997]. When the removal of surface material is approximately balanced by the soil production, the soil system is assumed to be in steady-state. The steady state soil thickness (or so-called SSST, *Phillips* [2010]) can be considered as a dynamic equilibrium of the system, where the thickness of the soil mantle stays relatively constant over time. Soil profiles operating under an exponential or bell-shaped soil production model tend to evolve toward steady state soil thickness because of the inverse relationship between soil production rate and soil thickness [*Pelletier and Rasmussen*, 2009]. The negative feedback mechanism between soil thickness and soil production rate was originally proposed by *Penck* [1953] and *Ahnert* [1977], and has been inferred from cosmogenic nuclide analyses on convex hillslopes by e.g *Heimsath* [1997]; *Heimsath et al.* [1999]. Although recent literature on chemical weathering often directly assumes that soils evolve towards steady state thickness [e.g. *Riebe et al.*, 2001; *Burke et al.*, 2007; *Dixon et al.*, 2009; *Norton and von Blanckenburg*, 2010], the concept has rarely been validated with empirical field data. It is, therefore, necessary to expand the foundational work initiated by *Dosseto et al.* [2011] and *Ma et al.* [2010] to a wider variety of environmental settings, as to constrain the quantitative relationship between soil

production and denudation.

Nowadays, long-term total denudation rates are commonly determined using in-situ produced and meteoric cosmogenic nuclides (e.g. ^{10}Be and ^{26}Al) [*Lal*, 1991; *Robert Bierman and Nichols*, 2004; *von Blanckenburg*, 2005; *Jungers et al.*, 2009; *Portenga and Bierman*, 2011; *West et al.*, 2013]. If long-term steady-state thickness of the soil is assumed, soil production rates can be derived from the ^{10}Be concentrations of samples taken at the soil-bedrock boundary [*Heimsath*, 1997; *Heimsath et al.*, 1999]. However, the a priori assumption of a soil thickness remaining constant over time can be questioned in highly dynamic environments [*Phillips*, 2010].

The disequilibrium of uranium isotopes (U-series: ^{238}U, ^{234}U, ^{230}Th, ^{226}Ra) is an alternative method that allows assessing weathering ages and soil formation rates through isotopic analysis of weathering products [*Chabaux et al.*, 2003b; *Dosseto et al.*, 2008b]. Although the potential of the method has been recognized in the 1960's, recent analytical improvements have boosted this field of research [*Dequincey et al.*, 1999; *Vigier*, 2001; *Dequincey et al.*, 2002; *Chabaux et al.*, 2003b; *Vigier et al.*, 2006; *Granet et al.*, 2007; *Granet et al.*, 2010; *Chabaux et al.*, 2011]. The U-series method is based on the decay chain of the radioactive isotope ^{238}U, decaying with a half-life ($T_{1/2}$) of ~4.5 Gyr to produce ^{234}U ($T_{1/2}$=244 kyr) which in turn decays to ^{230}Th ($T_{1/2}$=75 kyr). In a system closed to any loss or gain of U-series isotopes, the fresh bedrock is assumed to reach secular equilibrium after ~1.3 Myr (i.e. daughter/parent activity ratios equal unity). When the weathering front propagates into fresh rock, the U-series start to deviate from secular equilibrium. The intensity of the disequilibrium depends on the duration and intensity of the weathering processes. Preferential leaching of ^{234}U > ^{238}U > ^{226}Ra >>^{230}Th implies that the weathered material (e.g. soil) is expected to have activity ratios of (^{234}U/^{238}U) <1 and of (^{230}Th/^{238}U) >1 [*Fleischer*, 1982; *Chabaux et al.*, 2003a; *Dosseto et al.*, 2008a]. Therefore, by using U-series isotopes, it becomes possible to constrain the average time elapsed since the onset of mineral weathering within a soil profile. The method has recently been used to constrain saprolite or soil weathering age in a variety of environments ranging from temperate climate regimes in e.g Australia [*Dosseto et al.*, 2008b] and Appalachian mountains [*Ma et al.*, 2010] to tropical regimes in e.g northern Brazil [*Mathieu et al.*, 1995] and Puerto Rico [*Chabaux et al.*, 2013]. However, until nowadays, semi-arid environments received relatively little attention, and quantitative information on soil weathering based on U-series isotopes is still largely lacking.

In this study, we present and compare analytical data from two independent isotopic techniques: in-situ produced cosmogenic nuclides and U-series disequilibria to constrain long-term development of soil-mantled landscapes. The Spanish Betic Cordillera (Southeast Spain) was selected for this study, as it offers us a unique opportunity to analyze soil thickness steady-state conditions for thin soils of semi-arid environments. At the same time, the frontiers of applying U-series disequilibrium techniques in thin, stony weathering profiles can be explored.

Study area and sampling strategy

All study sites are located on the eastern part of the Betic Cordillera. For a detailed description of the study sites, we explicitly refer to *Chapter II*. The region is composed by E-W to SE-NW oriented mountain ranges rising up to 2000 m a.s.l (Figure 4.1). The Betic Ranges result from tectonic compression and shortening arising from the convergence of the African and Eurasian plates [*Braga et al.*, 2003; *Jabaloy-Sánchez et al.*, 2007]. The eastern part of the Betic Cordillera has undergone a wide range of pressures and temperatures during shortening which began around 51 Ma. The ranges are underlain by three stacked geologic formations which were exhumed during the early Miocene. The Alpujarride and Nevado-Filabres complexes are the most upper ones, while the Malaguide complex is largely covered and only outcropping in the northern part of the Sierra de las Estancias. All three study sites belong to the upper most formations and are underlain by mica-schists [*Ameijeiras-Mariño et al.*, 2015]. Small outcrops of phyllite, interbedded quartzite veins and limestone are present [*ICONA*, 1988]. The mineralogy of the mica-schists is composed of about 30% quartz, 25% muscovite and <10% clinoclore [*Ameijeiras-Mariño et al.*, 2015].

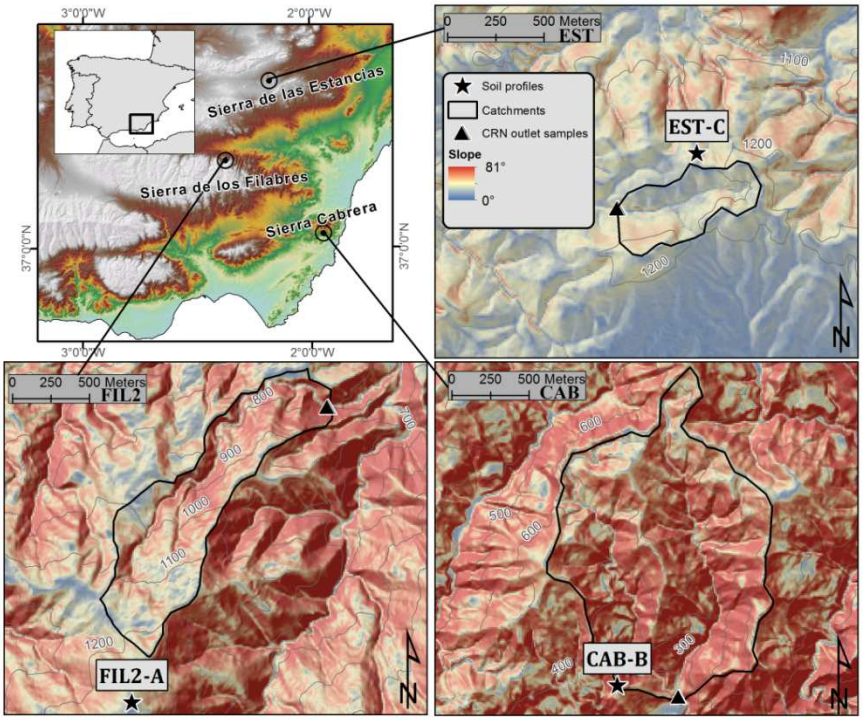

Figure 4.1: Topographic maps showing the sampling sites at Sierra de las Estancias (EST), Sierra de los Filabres (FIL2) and Sierra Cabrera (CAB). Note that all soil profiles (black stars) were selected at or near the ridge crest. Catchment-wide ^{10}Be denudation rates are derived from river sediments sampled at the outlet of the catchments (black triangle) [Bellin et al., 2014].

The Betic Ranges show strong morphological contrasts: the Sierra de las Estancias is characterized by broad convex landforms, the Sierra de los Filabres by broad convex ridgetops that steepen downslope toward the valleys, and the Sierra Cabrera displays a steep and highly dissected landscape (Figure 4.1, Table 4.1). The modern topography is a result of its recent tectonic history [*Braga et al.*, 2003]. Long-term ^{10}Be-derived denudation rates are generally low, and range from 34 ± 24 mm/kyr for Sierra de las Estancias (n = 5), 54 ± 25 mm/kyr for Sierra de los Filabres (n = 8) to 164 ± 74 mm/kyr for Sierra Cabrera (n = 3) [*Vanacker et al.*, 2014]. The spatial pattern and magnitude of ^{10}Be-derived denudation rates are consistent with tectonic uplift rates [*Bellin et al.*, 2014] that were constrained from marine deposits and trenching observations by *Braga et al.* [2003] and *Masana et al.* [2005].

The present climate of the eastern Betic Cordillera is characterized by warm summers and mild winters and is defined as semi-arid based on a ratio of precipitation over potential evapotranspiration between 0.2 and 0.8 [*Estrela et al.*, 1997]. The mean annual

precipitation ranges between 275 (± 25) and 425 (± 25) mm depending on elevation [*García*, 2009]. Precipitation records present large inter- and intra-annual variability, and torrential rainfall (200 mm/24 h) has been recorded [*De Luís et al.*, 2000]. The mean annual temperature decreases with altitude, and ranges from 16 ± 1 °C in Sierra Cabrera to 12 ± 1 °C in the Sierra de las Estancias and Filabres [*García*, 2009]. There exists large seasonal climate variability with a mean monthly temperature of 4.5°C in January and 22.3°C in July for the Sierra de las Estancias. Mean annual potential evapotranspiration (ET_p) is estimated at 900 mm for Sierra Cabrera and 794 mm for Sierra de las Estancias [*Junta de Andalucía*, 2008], implying soil water deficit during the prolonged dry season [*Schoonejans et al.*, 2016b]. Sclerophyllous and thorny vegetation are the dominant vegetation type , while small remnants of mesophilous taxons can be found at higher elevations [*Bellin et al.*, 2013].

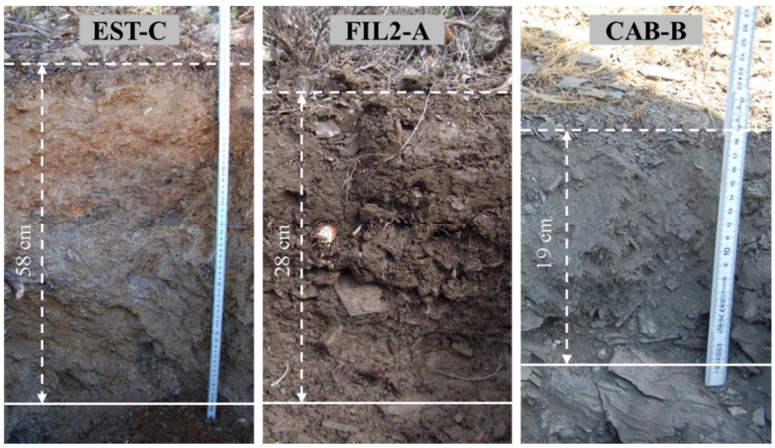

Figure 4.2: Illustration of the soil profiles studied across the Betic Cordillera with indication of soil thickness (cm) above the refusal layer (white line). Profiles were taken in Sierra de las Estancias (EST-C), Sierra de los Filabres (FIL2-A) and Sierra Cabrera (CAB-B).

Table 4.1: Key characteristics of soil profiles. Soil and catchment-wide denudation rates are derived from in-situ ^{10}Be cosmogenic radionuclides [Bellin et al., 2014; Schoonejans et al., 2016b]. Tectonic uplift rates are obtained from marine deposits and trenching observations [Braga et al., 2003; Masana et al., 2005].

Sample profile	Sierra	Latitude	Longitude	altitude elevation	Soil thickness	Average slope gradient of the catchment[a]	^{10}Be surface denudation rates (± 1 σ)	^{10}Be catchment-wide denudation rates (± 1 σ)	Tectonic uplift rates
		(°W)	(°N)	(m)	(cm)	(°)	(mm kyr^{-1})	(mm kyr^{-1})	(mm/kyr)
EST-C	de las Estancias	2°10'43"	37°35'22"	1187	58	14±5	73±11 (23 ± 3 in EST-A)	26 ± 3	10-40 (min)
FIL2-A	de los Filabres	2°22'25"	37°18'35"	972	28	23±9	14 ± 2	74 ± 8	110(min)
CAB-B	Cabrera	1°56'42"	37°3'7"	525	18	28±8	109 ± 22	246 ± 31	170 (min)

[a] Altitude and average slope gradient are derived from the 10-m resolution DEM [Junta de Andalucía, 2005].

The sampling campaign was conducted in September 2013, as part of a larger sampling campaign described in *Schoonejans et al.* [2016b]. Three soil profiles were sampled in the Sierra de las Estancias, Sierra de los Filabres and Cabrera (Figure 4.1, Table 4.1). Pits were excavated on exposed ridge tops to avoid the complexities of soil forming processes associated with lateral transport of soil particles along slope (Figure 4.1). As such, pedogenesis mainly occurs through a vertical redistribution of soil particles and elements within the profiles. All soils are very thin (< 60 cm) and overlay mechanically fractured mica-schist (Figure 4.2). Soils in Sierra de los Filabres and Cabrera are classified as Regosols according to the FAO WRB soil taxonomy [*IUSS Working Group WRB*, 2014] and do not present marked differentiation in soils horizons. Soils in the Sierra de las Estancias are clearly more developed having a soil thickness of ~60 cm compared to 20-30 cm in the Sierra de los Filabres and Cabrera. Two soil horizons can be observed: a light brown organic A horizon (0 to 15 - 20 cm) over a clay-rich B horizon (15 to 45 - 60 cm). The progressive change in color and texture from top to base of the profile suggests that soils are in a transitional stage of development, and can be defined as Cambisols [*Schoonejans et al.*, 2016b]. Within each soil profile, we sampled bulk soil material (0.5 kg) at 4 to 5 depth slices down to the soil-bedrock boundary, and a fragment of bedrock below the refusal layer.

Analytical methods

In total, we analyzed 14 soil and 3 rock samples from three weathering profiles (EST-C, FIL2-A and CAB-B). All samples were air dried and sieved at 2 mm. The weathering rings of rock samples were removed by sawing to get, as far as possible, unweathered parent material. Representative subsamples of soil (~100 mg) and rock were then powdered in an agate disk mill (~100µm) to ensure a complete sample acid digestion. Major element concentrations were determined by ICP – AES and trace element concentrations by ICP-MS after alkali fusion with Li-metaborate and Li-tetraborate [*Chao and Sanzolone*, 1992]. Loss on ignition (LOI) was recorded following combustion of an aliquot at 1000°C for 24h. The accuracy of the element chemistry was tested with reference material BHVO-2 [Basalt, Hawaiian Volcanic Observatory, *Wilson*, 1997] and WS-E [Great Whin Sill, Northern England, *Govindaraju et al.*, 1994]. The analytical uncertainty is evaluated at <3% for major element concentrations and <6% for trace element concentrations (Suppl. Inf. Table SI 4.1). One procedural blank was processed to

determine external contamination, and the reported concentrations are corrected for blank (Table SI 4.1).

Soil denudation rates are determined from ^{10}Be concentrations in three bulk soil samples taken above the soil-bedrock interface at depth *z* (cm). The ^{10}Be concentrations were corrected for laboratory blank (having a ^{10}Be/^{9}Be ratio of $0.48 \pm 0.14\times10^{-14}$), and the 1σ uncertainty estimates contain analytical errors from AMS measurement and blank error propagation. We refer to *Schoonejans et al.* [2016b] for further analytical details.

The preparation, geochemical analyses and determination of U-series isotopic ratios of the samples were performed at the University of Strasbourg (LHyGeS), France. The U and Th isotope ratios were analyzed on a Thermo Scientific NEPTUNE (ICP-MS) mass spectrometer after digestion (HNO_3, $HClO_4$, HF), separation and purification of U and Th by anionic exchange chromatography (resin Biorad® AG1X8, 200-400 mesh and Spec 50-100) following *Granet et al.* [2007]; *Pelt et al.* [2008]. The mass bias and SEM/Faraday cup yield were corrected by standard bracketing using HU1 and IRMM184. ^{226}Ra activity ratio were measured by TIMS on a Thermo Scientific Triton by using a single Re filament procedure with Ta_2O_5 following a protocol adapted from *Chabaux et al.* [1994] and *Pelt et al.* [2013]. The accuracy of the U isotopic analyses was tested with the rock standard BCR-2 and analytical uncertainties have been evaluated at 0.5% for (^{234}U/^{238}U), 2% for (^{230}Th/^{238}U), 1% for (^{238}U/^{232}Th), 2.5% for (^{230}Th/^{232}Th) and 3% for (^{226}Ra/^{230}Th). The internal reproducibility of the analysis was checked by duplicate analyses of a sample selected randomly (R-EST-C-4) and results were better than 0.5 % for (^{234}U/^{238}U), 1 % for (^{238}U/^{232}Th) and 1.9 % for (^{230}Th/^{238}U). Then, the external contamination was tested with a total procedure blank: 77 pg (0.5 ‰) for U, 149 pg (0.16 ‰) for Th and a contribution below 1 ‰ for Ra which is negligible compared to the amount of U, Th and Ra analysed.

Based on the U-series isotopic composition measured in the soil profile, it is possible to determine the weathering age (*t*) [*Dequincey et al.*, 2002; *Chabaux et al.*, 2003b; *Dosseto et al.*, 2008b]. The time evolution of a nuclide *j* (N_j) can be described as:

$$\frac{dN_j}{dt} = f_j N_{j0} - k_j N_j - \lambda_j N_j + \lambda_i N_i \quad (4.1)$$

Where N_j is the abundance of the nuclide ^{238}U, ^{234}U, ^{230}Th or ^{226}Ra (in number of atoms), N_i the abundance of the parent nuclide (note that this term is not present for ^{238}U), N_{j0} is the initial number of atoms, λ_j and λ_i are the radioactive decay constants (in yr^{-1}) for nuclide j and i respectively, f_j is the input coefficient (or gain) of nuclide j (in yr^{-1}) in the soil system and k_j is a first-order rate constant (in yr^{-1}) for output of nuclide j. Input and output coefficients encompass different processes, such as mineral dissolution or nuclide desorption from minerals, co-precipitation of nuclides with secondary minerals or alpha recoil-effect.

To determine weathering front propagation, the model assumes that initial fractionation of U-series nuclides occurs at the soil-bedrock interface and is controlled by weathering processes only. Secondly, although input and output coefficients (f_j and k_j) are representing a wide range of soil forming processes, they are represented in the model by constants implying that soil forming mechanisms are assumed to stay relatively constant over the soil residence time.

The model to estimate the weathering age (t) is solved numerically, using analytical data on ($^{234}U/^{238}U$), ($^{230}Th/^{234}U$) and ($^{226}Ra/^{230}Th$) ratios. The numerical solutions are obtained using a stochastic quantum particle swarm optimization scheme which minimizes the sum of the squared differences between measured and estimated activity ratios (for more precisions on the model, we refer to *Chabaux et al.* [2012] and *Chabaux et al.* [2013]). The estimation is based on a random set of t, k_j and f_j values which are allowed to take any value between the upper and lower parameter boundaries. In order to reduce the number of unknown parameters in our over-determined system, k_{230} and f_{230} are assumed to be negligible based on the observation that total mass-transfer coefficient $\tau_{Zr,Th}$ is generally lower than $\tau_{Zr,U}$ (Suppl. material Table SI 4.2). A similar assumption is used in previous studies by *Chabaux et al.* [2008] and *Dosseto et al.* [2014]. The parameter solutions that allow the model to fit observed activity ratios within approximately 7 % error are retained, and then averaged to obtain a set of optimized output parameter values, X_n. The cutoff value of 7% is here a compromise between maximizing the goodness-of-fit of the model, and maximizing at the same time the representativeness of model parameter solutions. The numerical models are run 1000 times, and the final results are computed as the mean of the results of individual model runs, $\overline{X_n}$ (Table 4.3, Figure 4.4, Table 4.4, Figure 4.5). The uncertainties on the parameter estimates are calculated as one standard deviation on the mean parameter estimate X_n.

The soil production rate (P) can then be estimated from the time duration (t) elapsed for a given sample to move from a reference depth in the soil profile to its current position and the thickness (H) of the soil between the reference and current sample position [*Chabaux et al.*, 2001; 2013]:

$$P = {}^{H}/_{t} \tag{4.2}$$

Given that the U-series fractionation model is over-determined, a series of samples is taken from the regolith profile to determine the mobility parameters and the age of the different samples relative to the reference sample. A mean soil production rate is then calculated from the variation of the weathering age of the samples in function of their distance to the reference sample following e.g. *Ma et al.* [2010]; *Chabaux et al.* [2013]; *Suresh et al.* [2013]. If weathering processes are uniform throughout the regolith profile, the soil production rate estimates are not dependent on the sampling position or choice of the reference sample.

In the case of the Betic Cordillera, thin soil profiles overly mechanically fractured bedrock. There is no clear continuum in chemical weathering processes between soil and hard metamorphic rock. As such, we use two different reference samples to constrain the mean soil production rate: (1) a fresh bedrock chip from below the refusal layer and (2) a soil sample taken just above the soil-bedrock interface. We refer to the mean production rates as P_{refR} and P_{refS} respectively.

RESULTS

Vertical distribution of major and trace elements in soil profiles

Element concentrations and mass transfer coefficients (τ, *Anderson et al.* [2002]) are presented in the Supporting Information (Table SI 4.1 and SI 4.2; *Schoonejans et al.* [2016b], *Chapter II*). A selected number of depth profiles of major and trace-element concentration are shown in Figure 4.3. Mass transfer coefficients, the so-called tau values (here determined by Zr enrichment), indicate that the major elements are depleted in the upper part of the soil profiles. Despite the fact that soil profiles are shallow, chemical weathering intensities increase gradually with decreasing soil depth, suggesting

that mixing by e.g. bioturbation is low. Analyses of the fractional mass change indicate that the soil at EST-C is more depleted in Na, K and Al compared to the soil profiles FIL2-A and CAB-B (Figure 4.3A, B and Table SI 4.2). The total fractional mass loss from chemical weathering in the soil, measured by the chemical depletion fraction, varies between ~0.05 and 0.29 for topsoil material, indicating that chemical weathering accounts for ~5 % to 29 % of total denudation. Chemical weathering losses are highest in the Sierra de las Estancias ($CDF_{(EST-C)}$ = 29 %), and Sierra de los Filabres ($CDF_{(FIL2-A)}$= 28 %) and lowest in Sierra Cabrera ($CDF_{(CAB-B)}$ = 15 %; Table SI 4.1, *Schoonejans et al.* [2016b], *Chapter II*).

Although our study sites do not present clear marks of open pit mining or soil pollution, our results show high enrichment values of Pb, Cd, Sb and As metals in the topsoil of the CAB-B profile sampled at Sierra Cabrera (Figure 4.3C and Table SI 4.1). Small-scale prospection and mining is reported to have occurred in the 18th to 20th century in the Sierra Cabrera [*Atlas Nacional de España*, 1993; *Castro et al.*, 2000]. The distribution of the trace metals in the CAB-B soil profile mimics the signature of the activity ratios of (^{230}Th/^{232}Th) and (^{238}U/^{232}Th) (see Figure 4.3 and 4.4). It is therefore likely that the minerals carrying heavy metals also carry isotopes of Th and U and affect the activity ratios that are measured at CAB-B.

The concentrations of U and Th range between 2.08 and 5.28 ppm and 10.85 and 20.31 ppm respectively (Table 4.2). The highest concentrations are measured in the Sierra Cabrera. For the deepest soil profile (EST-C), the U and Th concentrations are systematically lower in the soil compared to the bedrock, while the opposite is true for FIL2-A and CAB-B. The Th/U ratio is generally higher in the soil compared to the bedrock, and the difference is particularly large in CAB-B.

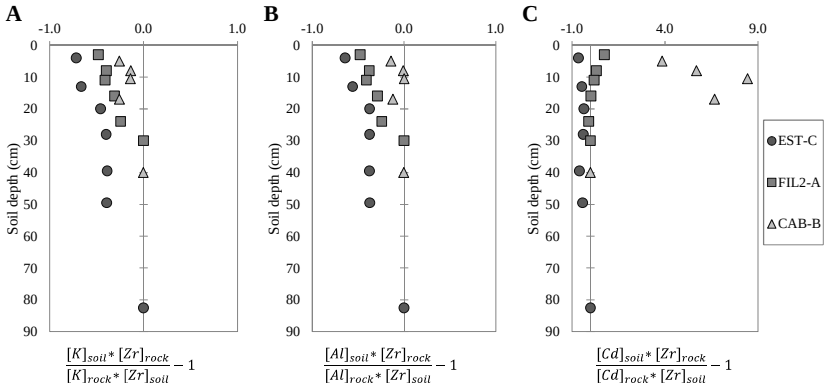

Figure 4.3: Depth variation of mass gains and losses of major (K, Al) and trace (Cd) elements for the three sites. Note that positive τ-values reflect mass gains and negative values mass losses.

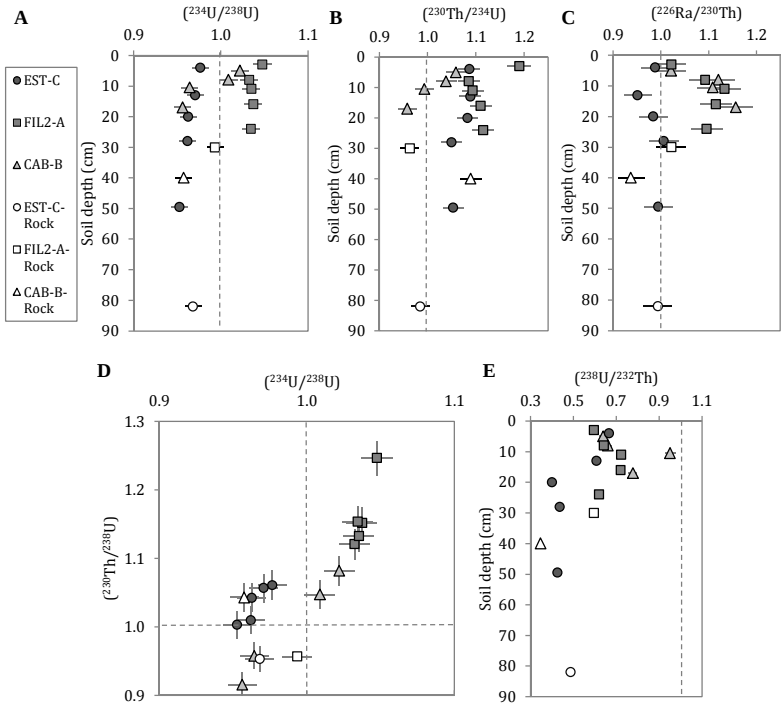

Figure 4.4: Depth variation of the measured ($^{234}U/^{238}U$) ,($^{230}Th/^{234}U$), ($^{226}Ra/^{230}Th$) and ($^{238}U/^{232}Th$) activity ratios in the soil profiles (respectively A, B, C and E). (D) Plot of ($^{230}Th/^{238}U$) vs ($^{234}U/^{238}U$) activity ratios at Sierra de las Estancias (EST-C), Sierra de los Filabres (FIL-2A) and Sierra Cabrera (CAB-B). The dashed line represents the value of the activity ratios at secular equilibrium.

Table 4.2: Summary of U and Th concentrations, and U, Th and Ra activity ratios of the three soil profiles from the Betic Cordillera as they were measured on ICP-MS and TIMS

Sample ID	Depth (cm)	[U] ppm	[Th] ppm	$(^{234}U/^{238}U)$ [1]	$(^{230}Th/^{238}U)$ [1]	$(^{238}U/^{232}Th)$ [1]	$(^{230}Th/^{232}Th)$ [1]	$(^{226}Ra/^{230}Th)$ [1]
EST-C-1	4	2.081	9.506	0.977 ± 0.005	1.061 ± 0.021	0.666 ± 0.007	0.707 ± 0.018	0.988 ± 0.030
EST-C-2	13	2.372	11.879	0.971 ± 0.005	1.057 ± 0.021	0.608 ± 0.006	0.642 ± 0.016	0.951 ± 0.029
EST-C-3	20	2.174	16.533	0.963 ± 0.005	1.042 ± 0.021	0.400 ± 0.004	0.417 ± 0.010	0.984 ± 0.030
EST-C-4	28	2.434	16.960	0.962 ± 0.005	1.010 ± 0.020	0.437 ± 0.004	0.441 ± 0.011	1.006 ± 0.030
EST-C-6	49.5	2.089	14.938	0.953 ± 0.005	1.003 ± 0.020	0.426 ± 0.004	0.427 ± 0.011	0.994 ± 0.030
EST-C-Rock	82	2.605	16.272	0.968 ± 0.005	0.953 ± 0.019	0.487 ± 0.005	0.464 ± 0.012	0.994 ± 0.030
FIL2-A-1	3	2.332	11.038	1.048 ± 0.005	1.247 ± 0.025	0.643 ± 0.006	0.801 ± 0.020	1.093 ± 0.033
FIL2-A-2	8	3.083	12.968	1.033 ± 0.005	1.121 ± 0.022	0.723 ± 0.007	0.811 ± 0.020	1.133 ± 0.034
FIL2-A-3	11	2.898	12.231	1.035 ± 0.005	1.132 ± 0.023	0.721 ± 0.007	0.816 ± 0.020	1.115 ± 0.033
FIL2-A-4	16	2.794	13.725	1.038 ± 0.005	1.152 ± 0.023	0.620 ± 0.006	0.713 ± 0.018	1.096 ± 0.033
FIL2-A-5	24	2.809	14.657	1.035 ± 0.005	1.153 ± 0.023	0.583 ± 0.006	0.673 ± 0.017	1.153 ± 0.035
FIL2-A-Rock	30	2.126	10.849	0.994 ± 0.005	0.957 ± 0.019	0.596 ± 0.006	0.57 ± 0.014	1.022 ± 0.031
CAB-B-1	5	4.268	20.312	1.022 ± 0.005	1.082 ± 0.022	0.639 ± 0.006	0.692 ± 0.017	1.021 ± 0.031
CAB-B-2	8	3.922	18.051	1.009 ± 0.005	1.047 ± 0.021	0.661 ± 0.007	0.692 ± 0.017	1.120 ± 0.034
CAB-B-3	10.5	5.279	16.882	0.964 ± 0.005	0.958 ± 0.019	0.952 ± 0.01	0.911 ± 0.023	1.109 ± 0.033
CAB-B-4	17	4.410	17.245	0.956 ± 0.005	0.916 ± 0.018	0.778 ± 0.008	0.712 ± 0.018	1.157 ± 0.035
CAB-B-Rock	40	1.571	13.774	0.958 ± 0.005	1.043 ± 0.021	0.347 ± 0.003	0.362 ± 0.009	0.937 ± 0.028
Rock Std								
BCR-2 (n=1)	-	1.682	5.928	1.003 ± 0.005	1.017 ± 0.020	0.863 ± 0.009	0.877 ± 0.022	0.995 ± 0.030
Replicate								
R-EST-C-4 (n=1)	28	2.443	17.046	0.961 ± 0.005	0.991 ± 0.020	0.433 ± 0.004	0.429 ± 0.011	0.996 ± 0.030

U-series activity ratios

Given that the outcrops are Miocene in age, secular equilibrium of the U-series isotopes in fresh bedrock can be expected. However, the activity ratios of ($^{234}U/^{238}U$) and ($^{230}Th/^{234}U$) in the bedrock samples (Table 4.2) are statistically different from 1 (Figure 4.4), suggesting that the U-series are not in secular equilibrium. It is possible that rock-water interaction in the hard bedrock is facilitated through the foliated structure of the mica-schist that facilitates micro-fracturing and water infiltration.

All samples from the soil deviate from secular equilibrium which is in agreement with the theory of U-series fractionation after chemical weathering. Our results show that ($^{234}U/^{238}U$) ratios are significantly different from 1. In the Sierra de las Estancias, ($^{234}U/^{238}U$) ratios range from 0.953 to 0.977, in the Sierra de los Filabres from 1.033 to 1.048 and Sierra Cabrera from 0.958 to 1.082. All three profiles present a slight decrease of ($^{234}U/^{238}U$) ratios with depth suggesting gain of U by surface processes (Figure 4.4). This signature is not coherent with the classical hypothesis of higher mobility of ^{234}U compared to ^{238}U, and indicates the complexity of isotope fractionation during weathering.

Figure 4.4 also illustrates that the ($^{226}Ra/^{230}Th$) activity ratio varies between the three sites, with a negative ratio in EST-C and positive one in CAB-B and FIL2-A. The variation in ($^{234}U/^{238}U$) and ($^{230}Th/^{238}U$) activity ratios within the three soil profiles seems to co-vary. The ($^{230}Th/^{234}U$) ratios are generally above 1, except in Sierra Cabrera where the two bottom samples present a ratio below 1 (Figure 4.4). The ($^{230}Th/^{234}U$) ratios generally decrease with depth which is consistent with the relative mobility of U and Th ($^{238}U>^{230}Th$) (Figure 4.4). For ($^{230}Th/^{232}Th$) and ($^{238}U/^{232}Th$) activity ratios, we notice an increase of the ratios near the top of the soil profile at the Sierra de las Estancias, whereas they decrease in the two other profiles (Figure 4.4 and Table 4.2) which could be explained by addition or leaching of U relative to Th.

DISCUSSION

In-situ ^{10}Be denudation rates

Surface denudation rates, constrained with in-situ produced ^{10}Be concentrations, range from 73 (± 11) mm/kyr in EST-C, 14 (± 2) mm/kyr in FIL2-A to 109 (± 22) mm/kyr in CAB-B [*Schoonejans et al.*, 2016b]. Soil denudation rates are generally less than or equal to catchment-wide denudation rates measured at the outlet of the basins (Table 4.1 and Figure 4.8). This might be an indicator that the rate of change in denudation with distance downslope depends on the topographic relief of the catchment, or an indication of the importance of soil particle trajectories in conditioning ^{10}Be depth profiles in unmixed soils as suggested by *Anderson* [2015]. The denudation rate inferred for EST-C (73 ± 11 mm/kyr) is higher than expected. Our ^{10}Be-derived denudation rates from five small basins draining the Sierra Estancias show evidence of rates of 26 ± 3 mm/kyr [*Vanacker et al.*, 2014] , and soil surface denudation of a nearby ridge profile (EST-A) is estimated at 23 ± 3 mm/kyr.

Mean soil production rates

The weathering age model estimates the evolution of the activity ratios of the samples in function of their distance to the reference sample. The mean soil production rate was here determined as P_{refR} and P_{refS} by using respectively a sample of fresh bedrock and soil material as reference. With regard to the P_{refR} model, the model solutions found for (^{234}U/^{238}U) and (^{230}Th/ ^{238}U) ratios are represented by a grey curve in Figure 4.5.

In the Sierra de las Estancias, the soil weathering age derived from the model is about 38 ± 12 kyr (Table 4.3 and Figure 4.5). Based on equation 4.2 and assuming H_{rock} equals 82.5 cm, the estimated soil production rate (P_{refR}) equals 22 ± 8 mm/kyr (Table 4.3). In Sierra de los Filabres and Sierra Cabrera, the model is not able to simulate correctly the isotopic disequilibrium in the soil profiles when the bedrock is used as reference sample (Table 4.3 and Figure 4.5). The model assumes that the parameters (k and f) are constant in the soil profile, implying that chemical weathering processes in rock and soil material are similar and constant through time. The abrupt differences in activity ratios between bedrock and soil samples - as shown in Figure 4.5 - suggest that these assumptions might not be valid.

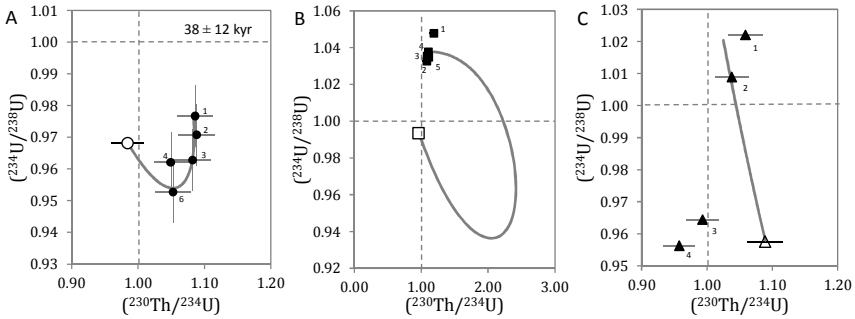

Figure 4.5: Measured ($^{234}U/^{238}U$) and ($^{230}Th/^{234}U$) activity ratios for the three soil profiles in the Betic Cordillera: (A) Sierra de las Estancias, (B) Sierra de los Filabres, (C) Sierra Cabrera (samples from bedrock are shown in open symbols, and soil in full symbols). The numbers refer to sample codes. Grey lines represent the evolution of the activity ratios in the soil profile as simulated with the U-series fractionation model using the bedrock sample as reference (Eq. 1). Where relevant, residence time is mentioned in the graph.

Table 4.3: Soil production rates (P_{refR}) and weathering ages (t) for the three soil profiles, as simulated by the numerical fractionation model taking bedrock as the reference sample

Sample profile	H (mm)	P_{refR} (mm/kyr)	t (kyr)	k_{238} (10^{-5} yr^{-1})	f_{238} (10^{-5} yr^{-1})	k_{234}/k_{238}	k_{234}/f_{234}	k_{226} (10^{-5} yr^{-1})	f_{226} (10^{-5} yr^{-1})
EST-C	825	22 ± 8	38 ± 12	5.7 ± 2.5	4.9 ± 2.2	1.8 ± 0.01	1.1 ± 0.01	4.7 ± 7.7	3.9 ± 7.5
FIL2-A	400	/	/	/	/	/	/	/	/
CAB-B	300	/	/	/	/	/	/	/	/

The second calibration of the U-series fractionation model uses the soil sample taken above the soil-bedrock interface (H_{soil}) as the reference sample. The overall fit of the soil weathering model (Figure 4.6) is better than the previous model considering the bedrock sample as a reference, which is shown by an important reduction of the Percent Bias [*Moriasi et al.*, 2007] from e.g. 3.2 % to 0.3 % for CAB. Similarly, the model also performs well for ($^{226}Ra/^{230}Th$) and ($^{230}Th/^{234}U$) ratios (Suppl. material Figure SI 4.1). Soil weathering ages range from 21 ± 4 kyr in the Sierra de las Estancias, 36 ± 7 kyr in the Sierra de los Filabres and 5 ± 1 kyr in the Sierra Cabrera (Figure 4.6). There is a large uncertainty on the modelled soil weathering age for Sierra de los Filabres (FIL2-A), resulting from a sub-optimal distribution of the activity ratios in the parameter space. Using the depth information of the soil profiles (H_{soil}), the mean soil production rate, P_{refS}, is estimated at respectively 24 ± 5 mm/kyr, 7 ± 1 mm/kyr and 35 ± 12 mm/kyr (Table 4.4).

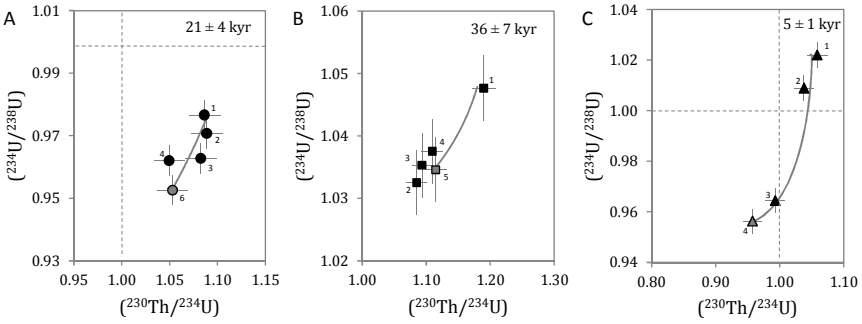

Figure 4.6: Measured ($^{234}U/^{238}U$) and ($^{230}Th/^{234}U$) activity ratios for the three soil profiles in the Betic Cordillera: (A) Sierra de las Estancias, (B) Sierra de los Filabres, (C) Sierra Cabrera (samples taken just above soil-bedrock boundary are in dark grey). The numbers refer to sample codes. Grey lines represent the evolution of the activity ratios in the soil profile as simulated with U-series fractionation model using the deepest soil sample as reference (Eq. 1). Where relevant, soil residence time is mentioned in the graph.

Table 4.4: Soil production rates (P_{refS}) and weathering ages (t) for the soil profiles, as simulated by the numerical fractionation model taking the deepest soil sample as reference.

Sample profile	H_{soil} (mm)	P_{refS} (mm/kyr)	t (kyr)	k_{238} (10^{-5} yr^{-1})	f_{238} (10^{-5} yr^{-1})	k_{234}/k_{238}	k_{234}/f_{234}	k_{226} (10^{-5} yr^{-1})	f_{226} (10^{-5} yr^{-1})
EST-C	495	24 ± 5	21 ± 4	1.2 ± 0.3	0.8 ± 0.3	1.3 ± 0.04	1.2 ± 0.04	2.0 ± 3.1	1.1 ± 3.0
FIL2-A	240	7 ± 1	36 ± 7	0.5 ± 0.1	0.2 ± 0.1	1.2 ± 0.04	1.9 ± 0.2	0.5 ± 0.5	3.6 ± 0.5
CAB-B	170	35 ± 12	5 ± 1	191.6 ± 42.5	163.5 ± 36.3	1.6 ± 0.02	1.1 ± 0.001	4.9 ± 4.2	4.6 ± 3.8

The parametrization of the soil weathering model suggests that optimal parameter values for k_{238} (leaching coefficient of ^{238}U) are 1.2×10^{-5} and 0.8×10^{-5} yr^{-1} and for f_{238} (input coefficient of ^{238}U) 0.5×10^{-5} and 0.2×10^{-5} yr^{-1} for the Sierra de las Estancias and Filabres respectively (Table 4.4). These parameter estimates are in the range of ^{238}U leaching coefficients reported in previous studies [*Dosseto et al.*, 2008b; *Ma et al.*, 2010]. The concentration density plots of the model outcomes (k_{238}, k_{234}, log k_{226}) illustrate the accuracy of the simulations, and are indicative of the model stability (Figure 4.7). The scatter on the model outcomes is larger for CAB-B compared to FIL2-A and EST-C, suggesting lower model stability (Figure 4.7). Overall, model estimates of k_{238} and k_{226} for the Sierra Cabrera are systematically higher than for Sierra de las Estancias and Filabres (Table 4.4), indicating either more intense weathering processes or a model less constrained. In all soil profiles, there is a preferential release of ^{234}U relative to ^{238}U during soil weathering with k_{234}/k_{238} ratios greater than one (Table 4.4). This is consistent with the basic model assumption that the ^{234}U isotopes are lost preferentially to ^{238}U isotopes through weathering [*Fleischer*, 1982; *Ivanovich and Harmon*, 1992; *Riotte et al.*, 2003]. Our data also suggest that uranium is removed faster than it is added to the

soil profile (shown by k_{238}/f_{238} and k_{234}/f_{234} > 1). This phenomenon is slightly enhanced in the Sierra de los Filabres.

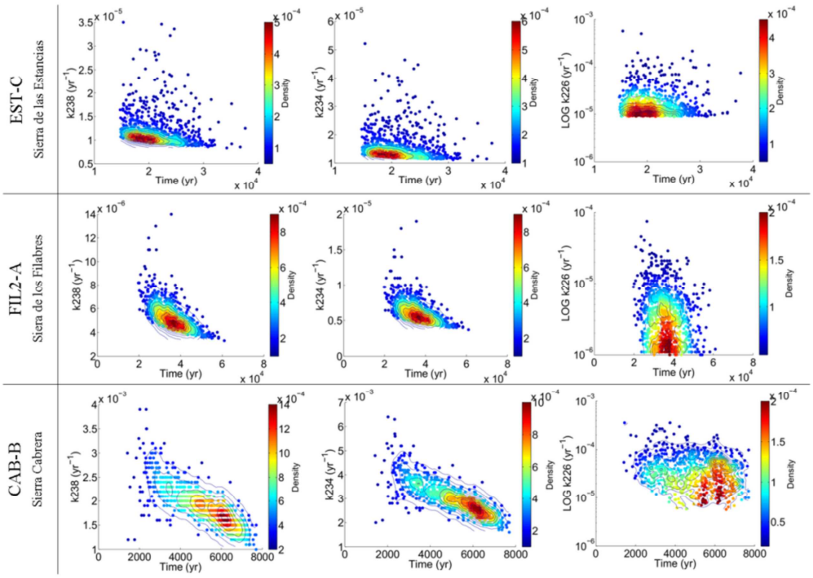

Figure 4.7: Density scatter plots for the soil weathering model based on U-series disequilibria. Leaching parameters k_{238}, k_{234} and k_{226} are plotted against time (yr).

Validation of model assumptions

Our application of the U-series fractionation model assumes that the parameters defining input and ouput of nuclides (f_j and k_j) through weathering are constant over time. In the Betic Cordillera, long-term denudation rates are sufficient to rejuvenate the thin soil after about 20 kyr in Sierra de las Estancias and Filabres and after ~2 kyr in Sierra Cabrera [*Bellin et al.*, 2014]. Since the mid-Holocene, the region is experiencing increased aridity causing a progressive degradation of the vegetation [*Rognon*, 1987; *Carrión et al.*, 2010; *Bellin et al.*, 2013]. The remoteness and higher elevation of the Betic Cordillera has allowed conservation of Pinus and Quercus forests, while lowlands often sheltered mesophytic to xeric flora. It is not clear how soil forming processes might be altered by long-term progressive changes in soil water balance in response to changes in climate and natural vegetation.

The mean soil production rate is here calculated from the variation of the weathering age

of different samples in function of their distance to the reference sample. Perturbations in depth variations in U-series disequilibria by e.g. bioturbation result in mixing of element and isotope concentrations over depths greater than 10 cm. The near-absence of vertical homogenization of major elements in the upper soil horizons is quite remarkable, and suggests that soil turnover and mixing through e.g. bioturbation is limited in our sites (Figure 4.3 and Suppl. Inf. Table SI 4.1 and 4.2).

The numerical model integrates all the input and redistribution fluxes that are occurring in the depth profile, including external input of uranium by e.g. dust, rain water or ocean sprays. First, dust deposition can influence the U and Th budget of the profiles, and potentially affect the measured activity ratios. While this is less pertinent for the analysis of deep weathering profiles, external input might be relevant for thin soil profiles. Dry deposition can significantly enrich terrestrial ecosystems in K, N, P, Fe and Ca [*Avila et al.*, 1998; *Chadwick et al.*, 1999; *Dia et al.*, 2006]. The Betic Cordillera is exposed to aeolian dust input from the Sahara and Sahel [*Castillo et al.*, 2008; *Scheuvens et al.*, 2013]. Most Saharan dust arrives with the North African anticyclone during summer red rains, and cyclonic activities play a role at the end of winter or spring [*Rodríguez et al.*, 2001]. Second, external input of dissolved uranium in rain water does not seem to have significant influence on the uranium content of river waters, suggesting that rain water is not altering activity ratios in soil weathering profiles [*Riotte et al.*, 2003; *Chabaux et al.*, 2005]. Third, sea sprays are often cited to be a potential source of external input in coastal regions [*Koide and Goldberg*, 1963], and ($^{234}U/^{238}U$) ratios in surface sea waters or sprays are consistently above 1 [e.g. *Koide and Goldberg*, 1963; *Miyake et al.*, 1966; *Aciego et al.*, 2015]. However, the work of *Pelt et al.* [2013] at Mount Cameroon showed that the contribution of uranium from sea spray deposits to the U and Th mass budget of soil profiles is negligible.

Our data are not conclusive on the importance of external input of uranium. In the studied sites, the ridge tops are typically exposed to wind and less favorable for dust deposition, unlike large intra-mountainous basins that often act as large captors [*Díaz-Hernández and Rüoss*, 2009]. Our data do not provide evidence for Si- or Al- enrichment at the top of the weathering profiles, as would be expected when levels of dust input are important. Dust from northern Africa and the Western Sahara is typically highly enriched in Silica (with SiO_2 content of dust ranging from about 50 to 60 weight percent [*Avila et al.*, 1998; *Castillo et al.*, 2008]). However, for the three study sites, the model simulations predict an input of uranium in the soil profiles (with $1 < k_j/f_j$, Table 4.4). In

addition, the activity ratios ($^{234}U/^{238}U$) that were measured in the topsoil samples of FIL2-A and CAB-B (closer to the sea) are slightly above 1. It is not clear if this enrichment is a direct result from external input as it could also be related to co-precipitation or sorption of U in secondary Fe-hydroxides or clay minerals [*Ma et al.*, 2010]. Information on ($^{230}Th/^{234}U$) and ($^{226}Ra/^{230}Th$) activity ratios in sea sprays or dust would be helpful to further constrain the element budgets.

Contrasting soil production and denudation rates

In steady state soil thickness conditions, soil denudation is predicted to balance soil production. Soil denudation is here derived from in-situ ^{10}Be cosmogenic isotopes, while mean soil production rates are estimated based on U-series disequilibria. The numerical U-series fractionation model is well constrained for the deeper weathering profile from Sierra de las Estancias. The mean soil production rates referenced to the bedrock and deepest soil sample agree well within uncertainty (P_{refS} = 24 ± 5 mm/kyr; P_{refR} = 22 ± 8 mm/kyr), suggesting that soil forming processes are uniform throughout the weathering profile. It is interesting to note that they are slightly lower than the ridge top soil production rates that were established for the Susquehanna Shale Hills Observatory (SSHO, Pennsylvania) by *Ma et al.* [2010]; [2013] that equal 40 ± 22 to 45 ± 12 mm/kyr. Although soil thickness and lithology are rather similar in both sites, there exist large differences in precipitation regime with a mean annual precipitation of about 1070 mm for the SSHO, compared to 425 mm for Sierra de las Estancias. The higher soil production rates reported at SSHO are consistent with the observed differences in climatic conditions.

For the thin soil profiles sampled in Sierras de los Filabres and Cabrera, there exist abrupt differences in activity ratios between bedrock and soil samples that hamper the calibration of the U-series fractionation model using bedrock as reference sample. When using the soil sample taken above the soil-bedrock interface as the reference sample, a mean soil production, P_{refS}, of 7 ± 1 mm/kyr and 35 ± 2 mm/kyr is obtained for Sierra de los Filabres and Cabrera respectively.

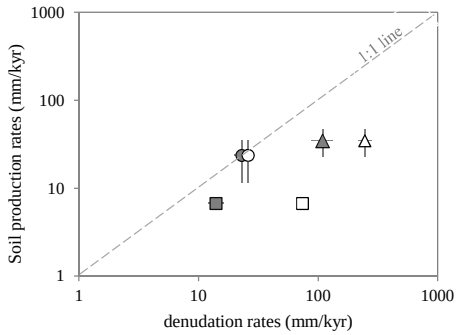

Figure 4.8: Mean soil production rates (P_{refS}) plotted against soil denudation rates for the three ridge top sites in dark symbols: Sierra de las Estancias (circle), Sierra de los Filabres (square) and Sierra Cabrera (triangle). Catchment-wide denudation rates, which integrate denudation of the entire catchment, of the sites are plotted in open symbols for comparison. Catchment-wide denudation rates exceed soil denudation rates as expected.

The observed pattern in U-series-derived soil production rates is congruent with the spatial pattern in ^{10}Be-derived soil denudation rates (Figure 4.8). Soil development is faster in the Sierra Cabrera, with soil denudation rates of 109 ± 22 mm/kyr and soil production rates of 35 ± 12 mm/kyr, compared to Sierra de las Estancias and de los Filabres with soil denudation rates of resp. 23 ± 3 and 14 ± 2 mm/kyr and soil production rates of 24 ± 5 and 7 ± 1 mm/kyr. Soil denudation and production rates in the Sierra de las Estancias and Filabres are of similar magnitude, suggesting that soils have evolved toward steady state soil thickness. In the rapidly eroding Sierra Cabrera, our data suggest that soil production is lower than denudation implying soil thinning. This can point to non-steady state conditions that can result from a recent adjustment of the upper convexities to the most recent tectonic uplift pulse in the Sierra Cabrera. This observation is congruent with the fact that the catchment-wide denudation rate exceeds surface denudation rates measured on the landscape convexities. However, in the latter case (CAB-B), the mean soil production rates established based on the U-series disequilibria should be analyzed with caution: the isotope fractionation model is not well constrained due to a limited number of depth samples and strong enrichment of the topsoil in heavy metals. As such, the hypothesis of steady-state soil thickness could only be validated for the deeper, slowly eroding soils of the Betic Cordillera that likely evolved to steady state over the last 20 kyrs.

CONCLUSION

Soil development in the Betic Cordillera was constrained using a combined approach based on in-situ produced cosmogenic radionuclides and U-series disequilibria. As such, this study is one of the first that applied U-series to constrain soil production by chemical weathering in very shallow soil (<60 cm thick) that developed on low grade metamorphic rocks in semi-arid climatic conditions. Three soil profiles were sampled across the Betic Ranges, at the ridge crest of zero-order catchments with distinct topographic relief, hillslope gradient and ^{10}Be-derived denudation rate. The magnitude of soil production rates determined based on U-series isotopes (^{238}U, ^{234}U, ^{230}Th and ^{226}Ra) is in the same order of magnitude as the ^{10}Be-derived denudation rates, suggesting steady state soil thickness in two out of three sampling sites. The results suggest that coupling U-series isotopes with in-situ produced radionuclides can provide new insights in the rates of soil development. However, our data also illustrate the potential frontiers in applying U-series disequilibria to track soil production in rapidly eroding landscapes characterized by thin weathering depths. The mechanisms of uranium fractionation through bedrock and soil weathering are difficult to grasp in shallow regolith/soil, as the numerical U-series fractionation model is currently under-constrained.

Chapter V

Long-term soil erosion derived from in-situ and meteoric ^{10}Be inventories in deeply weathered soils in southern Brazil

Based on:

Schoonejans, J., V. Vanacker, S. Opfergelt, M. Christl (in prep.) Long-term soil erosion derived from in-situ and meteoric 10Be inventories in deeply weathered soils in southern Brazil

ABSTRACT

Meteoric ^{10}Be are commonly used as a geochemical tracer of soil erosion and regolith residence time over long time scales (> 10^3 yr). However the low retention of the meteoric ^{10}Be in acidic weathering profiles complexified the translation of meteoric ^{10}Be inventories into surface denudation or residence time. In this study, we aim to evaluate the potential loss of meteoric ^{10}Be in the weathering zone. Along a toposequence in southern Brazil, three regolith profiles have been sampled from the convexity to the toeslope. We explore the behavior of the Beryllium in the

regolith over the hillslope through a sequential chemical extraction of four reactive fractions. Based on existing protocols it appears that amorphous oxy-hydroxide and crystalline oxide fractions are the main carriers of the Beryllium. The inventories of meteoric ^{10}Be are significantly higher in the accumulation zone than on the convexity which demonstrates that leaching and deep percolation of meteoric ^{10}Be occur along the hillslope. We estimate surface denudation rates on the convexity after correcting the inventories for incomplete retention of meteoric ^{10}Be by quantifying the chemical mass losses of the stable isotope, ^{9}Be. More than 50 % of the delivered meteoric ^{10}Be has been leached from our upslope regolith profiles. Upslope denudation rates are below 5 mm/kyr and correspond to in-situ ^{10}Be-derived rates. This study demonstrates that retention of meteoric ^{10}Be can no longer be ignore or neglect in highly weathered soils in order to constrain geomorphic rates.

INTRODUCTION

The development of isotopic techniques has facilitated the quantification of long-term geomorphic processes at the Earth's surface [*Banner*, 2004; *Ivy-Ochs and Kober*, 2008; *Preusser et al.*, 2008]. Cosmogenic isotopes that are formed in minerals at the earth surface (in-situ) or in the atmosphere (meteoric) are now commonly used for dating and determining denudation rates. The first applications of cosmogenic radionuclides in geomorphology were based on meteoric ^{10}Beryllium, after in-situ produced ^{10}Beryllium (^{10}Be) has routinely been used during the last 15 years to constrain surface exposure ages and/or erosion rates over timescales of 10^3 to 10^6 years [*Lal*, 1991; *von Blanckenburg*, 2005]. This radioactive isotope (half-life =1.38 Myr [*Chmeleff et al.*, 2010]) is produced at the Earth surface by the interaction of rock and soil material with high-energy cosmic rays. Recent improvements of the meteoric ^{10}Be delivery mechanisms and rates have led to a renewed interest in meteoric ^{10}Be as tracer for geomorphic processes (summarized by *Willenbring and von Blanckenburg* [2010]). Contrary to the in-situ ^{10}Be, meteoric ^{10}Be is produced in the atmosphere by cosmic ray spallation of ^{16}O and ^{14}N isotopes and delivered to the Earth's surface by rainfall or dust. It accumulates at the terrestrial surface by adsorption onto mineral surfaces or coprecipitates with amorphous and crystalline iron-oxy-hydroxides, clays or carbonates [*Barg et al.*, 1997]. The main advantages of meteoric ^{10}Be over in-situ ^{10}Be are that it requires smaller sample amounts due to its higher concentrations in soils and that it can be applied to quartz-free lithologies.

In geochemical studies, meteoric ^{10}Be is often used as a tracer for soil development [*McKean et al.*, 1993; *Jungers et al.*, 2009; *Willenbring and von Blanckenburg*, 2010; *West et al.*, 2013] and regolith residence time [e.g. *Pavich et al.*, 1984; *Bacon et al.*, 2012]. Recent studies have shown that meteoric ^{10}Be is not conservative in weathering profiles of acidic environments (having a pH < 4 to 6) [*You et al.*, 1989; *Aldahan et al.*, 1999; *Graly et al.*, 2010], and part of the meteoric ^{10}Be can be translocated to the saprolite or lost by leaching and deep percolation. At a field site in the Southern Piedmont (USA), *Bacon et al.* [2012] demonstrated that a considerable portion of the total meteoric ^{10}Be is leached from the regolith profile (Utisol, pH_{CaCl_2} ~4). In such conditions, the total amount of meteoric ^{10}Be presents in the regolith is no longer directly related to soil residence time or surface denudation. If the losses are on the order of 26% of the total meteoric ^{10}Be inventory, the error on the residence time can reach up to 25% following recent work by *Maher and von Blanckenburg* [2016]. It is therefore essential to account for potential losses of meteoric ^{10}Be in acidic weathering environments. Normalization methods that use the ratio of meteoric ^{10}Be over the stable isotope ^{9}Be have been developed to resolve potential losses of non-conservative tracers in the critical zone [*Wittmann et al.*, 2012; *von Blanckenburg et al.*, 2012]. Alternatively, *Campforts et al.* [2016] developed a numerical model that allows one to quantify soil production and denudation while accounting for leaching of meteoric ^{10}Be. It remains important to test and further develop the numerical schemes based on experimental data.

In order to evaluate the potential loss of meteoric ^{10}Be in the weathering zone, we selected a study site with deeply weathered soils in southern Brazil (pH_{H2O} = 4.7 to 5.9). A multi-proxy approach was established where the stable isotope, ^{9}Be, that is mobilized from weathering, was used to correct for incomplete retention of meteoric ^{10}Be within the regolith profile. Successive chemical extractions were realized on the regolith samples to understand the behavior of Beryllium (^{9}Be) in the soil system. The measurements of the meteoric ^{10}Be isotopes were then paired with in-situ ^{10}Be denudation estimates to provide new insights in the development of the critical zone in highly weathered subtropical environments.

METHODOLOGY

Soil sampling in CZO southern Brazil

The region has a subtropical climate, with influence of air masses coming from the Atlantic ocean [*Alvares et al.*, 2013]. A semi-deciduous subtropical forest with Araucaria trees covers the study site (Figure 5.1).The CZO is located at the southern border of the so-called Serra Geral Formation which is a volcanic plateau [*Bellieni et al.*, 1986; *Montanheiro et al.*, 2004] dated from the Mesozoic era (137-127 Ma according *Turner et al.* [1994]). The XRD mineralogical analysis of the bedrock (rhyodacitic volcanic rocks) reveals that sanidine (feldspar group) is the most abundant mineral (45-55%), followed by very fine grained quartz (~38%) embedded in a matrix of hematite, goethite and clays (~8%). Soils are classified as Alisol and Acrisol according the FAO system [*IUSS Working Group WRB*, 2014] with a pH_{H2O} between 4.7 and 5.9.

This study focuses only on the north-west facing slope of the catchment which is 210 m long. The toposequence has a mean slope of 13°, and a pronounced break in slope of 24° in the middle section of the transect (Figure 5.1 and Figure 5.2). Pits were excavated at the upslope (*S-Top*), lower middle (*S-LM*) and toeslope (*S-Bot*) topographic position (Figure 5.1 and Figure 5.2, *Chapter III*). All regolith profiles have been excavated to the refusal layer (saprolite) or to 2 meters deep and were sampled in detail by taking depth slices. The regolith is here defined as the loose, unconsolidated superficial layer overlaying the bedrock, and is progressively weathered over time; and the saprolite as the chemically weathered rock that retains the original structure and fabric of the host material.

Three pits (S-Top, S-LM, S-Bot) were analyzed in great detail (Figure 5.2), and 14 regolith and 4 saprolite samples were analysed for (i) total meteoric ^{10}Be concentrations, and (ii) Beryllium-9 concentrations in selective chemical extractions of reactive mineral phases. In addition, samples from replicate pits (S-Top1, S-Top3, S-LM1, S-LM3 and S-Bot2, Figure 5.1) were combined into a single homogenized samples (composite samples) to measure the total inventory of meteoric ^{10}Be. The amalgamation procedure accounts for differences in soil density and sampling thickness of each replicates profiles. At the convexities, three bulk samples (~ 6kg) were taken at the regolith-saprolite interface in S-Top1 and in two replicate pits (G-Top4 and S-Top6) to measure

the concentration of in-situ produced ^{10}Be (Figure 5.1). All profiles that were sampled for in-situ produced ^{10}Be are located on the landscape convexity, where the regolith mantle is assumed to have a steady-state soil thickness.

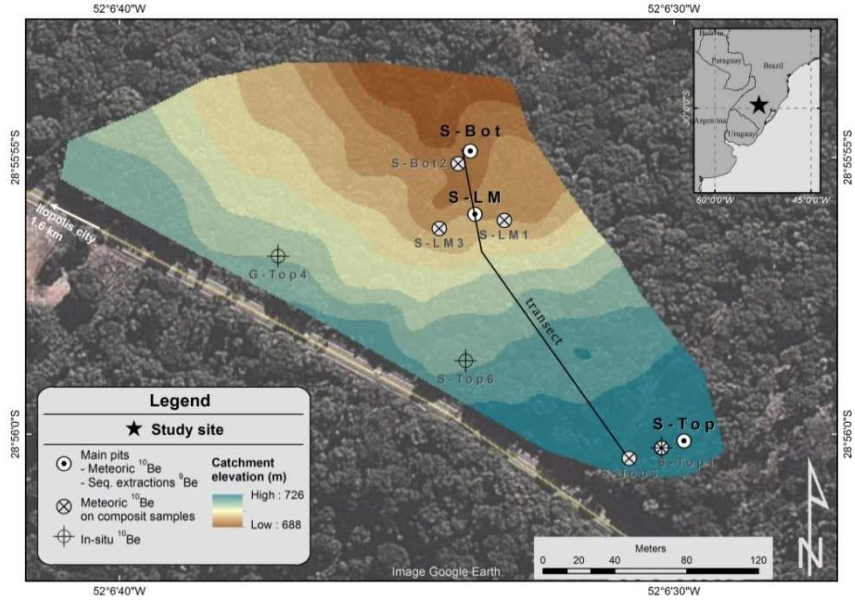

Figure 5.1: Topographic map of the Critical Zone Observatory in southern Brazil, with location of the sampling pits. The regolith profiles that were analyzed in full detail for meteoric ^{10}Be are shown by a black dot, the profiles where composite samples were taken for meteoric ^{10}Be analyzes with a multiplication sign (×), and the pits where in-situ ^{10}Be was analyzed with a cross sign (+).

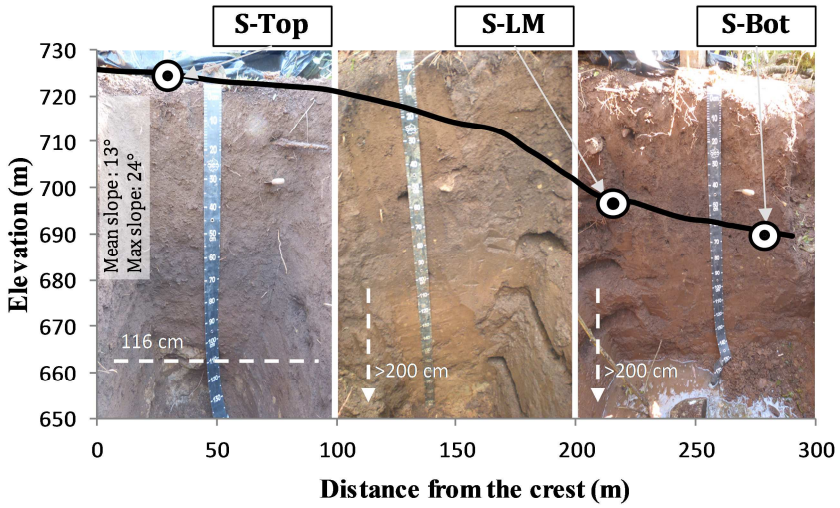

Figure 5.2: Toposequence (S-Top, S-LM, S-Bot) at critical zone observatory. The pictures are illustrative for the change in physical and chemical soil properties along hillslope. The topographic profile is shown by the black line, and the thickness of the regolith (cm) is marked on the pictures

Meteoric and in-situ produced cosmogenic radionuclides

This study uses meteoric ^{10}Be isotopes to quantify regolith denudation rates under highly weathered environmental conditions. To evaluate potential losses of meteoric ^{10}Be by leaching and deep percolation, we use here the stable isotope, ^{9}Be, mobilized from weathering of the parent material. A sequential chemical extraction scheme was applied on the mineral reactive phases. In addition, in-situ produced ^{10}Be concentrations were measured to determine surface denudation rates.

Sequential extraction of Beryllium

A sequential chemical extraction was performed on 18 samples. As the stable isotope of Beryllium, ^{9}Be, constitutes for more than 99.9% of the total Beryllium, we refer hereafter only to ^{9}Be. We assume that the inventory of ^{9}Be in the weathering zone relative to the parent material ^{9}Be reflects the loss of ^{10}Be in the weathering zone due to leaching and deep percolation. As the chemical properties of the Beryllium isotopes are identical, they behave similarly in the regolith [*Wittmann et al.*, 2012]. We hereby neglect external input of ^{9}Be, and assume that the only input of ^{9}Be to the soil comes from weathering of the primary minerals. The sequential ^{9}Be-extraction is based on the method presented in *Bourles et al.* [1989] and *Wittmann et al.* [2012]. It is here applied to ~0.9 g of sample that is dried, sieved at 2 mm and grinded. The extraction procedure isolates four fractions: (i) the exchangeable fraction ($^{9}Be_{ex}$) that is extracted by using 10 ml of 1M $MgCl_2$ solution and shaking for 12 hour, (ii) the reactive amorphous oxy-hydroxide fraction ($^{9}Be_{am\text{-}x}$) that is extracted by using 10 ml of 0.5 M HCl and shaking for 24h, (iii) the crystalline oxide fraction ($^{9}Be_{x\text{-}ox}$) extracted by using 10 ml of 0.5 hydroxylamine-hydrochloride solution in 1 M HCl, (iv) the residual fraction containing mainly silicate minerals ($^{9}Be_{residual}$) is treated with a mixture of 28 M HF and Aqua Regia to fully decompose the samples. The organic phase has not been extracted separately because of the negligible amount of organic matter (OM) in our samples (about 5 % in the upper 10-20 cm, and <3 % below 30 cm [*Trigalet et al.*, in prep.]). Between each step of the ^{9}Be-extraction procedure, the residue was washed 3 times with ultrapure water. Concentrations of $^{9}Be_{ex}$, $^{9}Be_{am\text{-}x}$ and $^{9}Be_{x\text{-}ox}$ were measured by Inductively Coupled Plasma Mass Spectrometry (ICP-MS) while $^{9}Be_{residual}$ was measured by ICP-Atomic Emission Spectroscopy at UCLouvain. Accuracy validation of our measurements was performed by decomposing about 0.4 g of two geo-standards of marine sediment (PACS-2 [*NRC-CRM*] and ISE 972 [*WEPAL*]. The concentrations measured are in agreement with the reference values (0.9 and 1.1 mg/kg). In addition, two procedural blanks were

processed to determine the external contamination which was below the detection limit. The reproducibility of our measurements was verified for each fractions based on duplicates of two randomly selected samples (S-Top/55-65 and S-LM/10-20). The final results show a difference of 6 ± 3 %.

Determination of meteoric ^{10}Be inventories

All regolith and saprolite samples were homogenized through a fine grinding after sieving (~1g). The meteoric ^{10}Be was extracted by ion exchange chromatography using a procedure adapted from *von Blanckenburg et al.* [1996b]. ^{10}Be/^{9}Be ratios were measured in BeO targets at ETH Zurich and were normalized based on the ETH secondary standard S2007N with a nominal value of ^{10}Be/^{9}Be of 28.1 × 10^{-12} [*Kubik and Christl*, 2010].

Inventories of meteoric ^{10}Be are calculated for the entire regolith profiles in order to estimate the accumulation time of the isotope. For that purpose, soil and saprolite samples were taken at depth intervals of 10 cm and covered 30 to 25% of the thickness of each profile: 5 samples in S-Top, 6 in S-LM and 7 in S-Bot. The meteoric ^{10}Be inventories ($I_{^{10}Be}$) of the regolith profiles are estimated (at/cm²) following the method presented in *Brown et al.* [1988] and *West et al.* [2013]:

$$I_{^{10}Be} = \int_{z_b}^{z_0} C_{Be} \rho dz \tag{5.1}$$

where z_0 and z_b correspond respectively to the depth of the soil surface (z = 0) and the regolith-bedrock interphase (cm), C_{Be} to the meteoric ^{10}Be concentration of the sample (at/g), ρ the bulk density of the sample (g/cm³) and dz the sample depth interval (cm). The depth integration is here performed using a spline function (SRS1, Cubic Spline).

The apparent regolith residence time (t, in yr) can be estimated if we assume a constant delivery rate of meteoric ^{10}Be over time and $I_{^{10}Be}$ at steady-state implying equivalent rates of delivery and removal of meteoric ^{10}Be. This condition is intrinsically restricted to the landscape convexities, where lateral transport of meteoric ^{10}Be is absent:

$$t = \left(\frac{-1}{\lambda}\right) \ln\left(1 - \frac{\lambda I_{^{10}Be}}{q}\right) \quad (5.2)$$

where λ is the radioactive decay constant for ^{10}Be (yr^{-1}) and q is the delivery rate of meteoric ^{10}Be to the earth surface (at cm^{-2} yr^{-1}). Considering the same assumptions, the meteoric ^{10}Be inventories can also be used to quantify surface denudation rates (mm/kyr) for the upslope areas (D):

$$D = \frac{(q - \lambda I_{^{10}Be})}{C_s \rho_s} \quad (5.3)$$

where C_s and ρ_s are the ^{10}Be concentrations and the bulk density of the uppermost surface sample (at cm^{-3}).

Correction for potential losses of meteoric ^{10}Be

Given the low pH values of the soils in the critical zone observatory, we correct the inventories for losses of meteoric ^{10}Be. The method presented here is inspired by the work of *Bacon et al.* [2012], and is based on the chemical mass losses of ^{9}Be in the regolith profile ($m_{^{9}Be,\,flux\,n}$, in at/cm²) to constrain chemical depletion of Beryllium. It uses the chemical mass balance model from *Brimhall and Dietrich* [1987] and *Egli and Fitze* [2000], and a conservative element (such as Ti) to quantify relative mass losses of mobile elements, and takes into account the volumetric changes in the regolith based on strain. The succession of equations is described in detail in *Chapter III* and is here summarized by the equation of the chemical mass losses of ^{9}Be:

$$m_{^{9}Be,\,flux} = \rho_p C_{^{9}Be,p} \int_0^{L_w} \frac{\tau_{^{9}Be}(z)}{(\varepsilon_{Ti}(z) + 1)} dz \quad (5.4)$$

where ρ_p and $C_{^{9}Be,p}$ correspond resp. to the bulk density (g/cm³) and the concentration in ^{9}Be (mg/kg) from the parent material. $\tau_{^{9}Be}(z)$ and $\varepsilon_{Ti}(z)$ are resp. the mass transfer coefficient of the ^{9}Be and strain at depth z in the regolith (unitless) that are integrated over the entire thickness of the regolith, L_w, (m) using a spline function (SRS1, Cubic

Spline). The mass losses of ^{9}Be can be quantified separately for each of the four fractions ($m_{^{9}Be,\,flux}$) by considering $C_{^{9}Be,p}$ of each fraction.

The chemical losses of the ^{9}Be fractions are added to the measured ^{9}Be inventory ($I_{^{9}Be}$, obtained in the same way than equation 5.1). The fractions selected for this correction should present a positive correlation with meteoric ^{10}Be concentrations. The ratio between the corrected and measured ^{9}Be inventory is then used to correct the meteoric ^{10}Be inventory:

$$I'_{^{10}Be} = I_{^{10}Be} \times \left(\frac{I_{^{9}Be} + m_{^{9}Be,\,flux}}{I_{^{9}Be}} \right) \tag{5.5}$$

where $I'_{^{10}Be}$ corresponds to the corrected inventory of meteoric ^{10}Be where $I_{^{9}Be}$ and $m_{^{9}Be,\,flux}$ are both expressed in at/cm².

By using the ^{9}Be chemical fractions to correct for potential loss of meteoric ^{10}Be in the regolith profile, we assume that the retention of the two Beryllium isotopes is the same within the regolith. Recent work by *Maher and von Blanckenburg* [2016] has challenged this assumption as meteoric ^{10}Be is supplied to the top of the regolith where secondary minerals are more abundant than at the weathering front where ^{9}Be is released from primary minerals. They argued that the spatial separation may result in different retention of the two isotope species [*Barg et al.*, 1997] that can be further exacerbated by biogeochemical gradients within the regolith profile.

In-situ produced ^{10}Be to constrain surface denudation

Concentrations of in-situ produced ^{10}Be in quartz grains are used to determine independently surface denudation rates, *D* (mm ky^{-1}). Samples were taken between 25 and 45 cm depth, were washed and dried. Because of the very low amount of pure quartz grains, we extracted quartz minerals by hand picking in order to get more than 3 g of pure quartz. The analytical methods are described in more detail in *Schoonejans et al.* [2016b]. The ^{10}Be/^{9}Be ratios were measured in BeO targets at ETH Zurich and then normalized with the ETH secondary standard S2007N with a nominal value of 28.1 × 10^{-12} [*Kubik and Christl*, 2010]. The ^{10}Be concentrations were corrected for laboratory blank

(having a ratio of $4.3 \pm 1.7 \times 10^{-15}$), and the 1σ uncertainty contains analytical errors from AMS measurement and blank error propagation (Table 5.4). We took into account depth shielding from the overlaying soil horizons to correct the ^{10}Be concentrations. Topographic shielding was corrected using the procedure described in *Norton and Vanacker* [2009]. Surface denudation rates were calculated with the Cronus online calculator version 2.3 [*Balco et al.*, 2008; http://hess.ess.washington.edu/], using the time-dependent scaling laws proposed by *Dunai* [2000].

RESULTS

Sequential extraction of ^{9}Be

Data obtained from the sequential extraction of ^{9}Be fractions are presented in table 5.1.

Table 5.1: Concentrations of ^{9}Be fractions that were sequentially extracted. The lower samples (S) correspond to saprolite samples.

Sample code	**^{9}Be$_{ex}$** *exchangeable* **(ng/gr)**	**^{9}Be$_{am\text{-}x}$** *amorphous oxy-hydroxide* **(ng/gr)**	**^{9}Be$_{x\text{-}ox}$** *crystalline oxide* **(ng/gr)**	**^{9}Be$_{residual}$** *residual* **(ng/gr)**	**Total ^{9}Be extractions (ng/gr)**
S-Top/10-20	4.1	29.7	105.6	573.7	713.0
30-40	3.7	32.2	118.6	569.1	723.6
55-65	5.6	60.3	135.5	566.2	767.5
95-105	16.7	107.6	195.0	575.6	894.9
155-160 (S)	16.4	48.7	258.4	653.4	976.9
Mean S-Top	9.3	55.7	162.6	587.6	815.2
S-LM/10-20	19.3	194.8	186.7	788.8	1189.6
30-40	15.8	243.0	281.5	798.4	1338.6
55-65	31.8	563.7	432.4	700.5	1728.4
95-105	31.4	358.8	390.0	740.0	1520.2
180-195	45.3	305.4	382.5	797.0	1530.2
235-240 (S)	94.6	109.4	525.1	879.8	1608.8
Mean S-LM	39.7	295.9	366.3	784.1	1486.0
S-Bot/10-20	52.9	404.4	323.5	997.1	1777.9
30-40	44.9	503.0	266.3	670.7	1485.0
55-65	53.9	786.5	399.1	648.1	1887.6
95-105	31.9	410.1	380.5	688.2	1510.8

180-190	49.4	285.0	355.9	743.6	1433.9
280-285 (S)	81.0	175.9	240.9	801.7	1299.6
395 400 (S)	90.3	122.4	95.1	805.9	1113.7
Mean S-Bot	57.8	383.9	294.5	765.0	1501.2

Along hillslope, there is a net increase of the total ^{9}Be concentrations in the regolith profiles: the mean concentration of total ^{9}Be is 815.2 ng/g at the upslope position (S-Top), 1486.0 at the midslope position (S-LM) and 1501 ng/g at the toeslope position (S-Bot). With regard to the Beryllium-9 chemical fraction, it is clear that the largest portion of ^{9}Be is retained in the silicate residues ($^{9}Be_{residual}$, 51 to 72% of the total ^{9}Be). Beryllium-9 fractions that were extracted from amorphous oxy-hydroxide and crystalline oxides ($^{9}Be_{am\text{-}x}$ and $^{9}Be_{x\text{-}ox}$) account respectively for 7% and 20% in the upslope profile, and their concentrations increase in the downslope profiles. The downslope increase of the reactive fractions is higher for the $^{9}Be_{am\text{-}x}$ chemical fraction that was extracted with HCl 0.5 M (Figure 5.3). The exchangeable fraction does not contain significant amounts of ^{9}Be ($^{9}Be_{ex,}$ 1 to 4% of the total ^{9}Be, Figure 5.3).

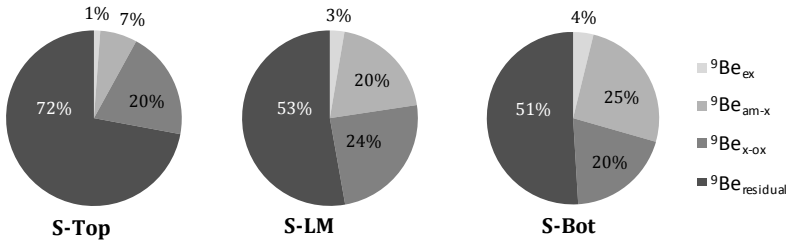

Figure 5.3: Share of the total amount of Beryllium-9 that is contained in each of the four chemical fractions: $^{9}Be_{ex}$ corresponds to the exchangeable fraction, $^{9}Be_{am\text{-}x}$ to amorphous oxy-hydroxide, $^{9}Be_{x\text{-}ox}$ to crystalline oxide, and $^{9}Be_{residual}$ to the fraction contained in the residual silicate minerals. The three plots show the difference in along hillslope (S-Top : upslope, S-LM: midslope and S-Bot: downslope position).

Figure 5.4 illustrates the variation in Beryllium-9 chemical fractions with depth for the three topographic positions (S-Top, S-LM, S-Bot). For the three regolith profiles, the exchangeable ^{9}Be fraction increases with depth, with the percentage of the $^{9}Be_{ex}$ fraction increasing from 1-3 % at the top to 2-8 % at the bottom of the profiles. The reactive fractions show a bell-shaped function with depth; the increase of $^{9}Be_{am\text{-}x}$ and $^{9}Be_{x\text{-}ox}$ in the first meter (peak at 100 cm for S-Top and 60 cm for two others profiles) is followed by a decrease to values <10 % (Figure 5.4). The residual ^{9}Be fraction does not show a linear trend, but shows a minimum value at 60 cm deep (34-40 %) and at 100 cm for S-Top (64 %) and then increases to 56 to 80 % at the surface. The latter illustrates that soil development strongly influences losses of ^{9}Be loss in this acidic environment.

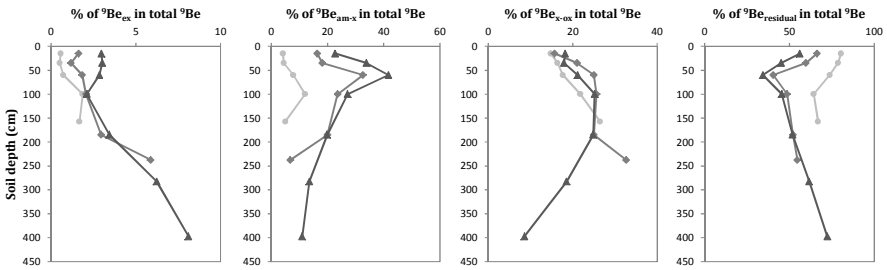

Figure 5.4: Variation of ^{9}Be chemical fractions with depth for the three topographic positions (circles=S-Top, diamonds=S-LM and triangles=S-Bot). The data are plotted as the share of the exchangeable ($^{9}Be_{ex}$), reactive ($^{9}Be_{am-x}$ $^{9}Be_{x-ox}$) and residual ($^{9}Be_{residual}$) fractions in the total ^{9}Be inventory of each sample. As such, the values on the four graphs sum to 100% for a given sample.

Variation in meteoric ^{10}Be concentrations along hillslope

The variation in meteoric ^{10}Be concentrations and ^{10}Be inventories with depth and along hillslope are presented in table 5.2.

The concentration of meteoric ^{10}Be is not constant with depth, and shows a peak-shaped depth distribution with maximum ^{10}Be concentrations at a depth of 60-100 cm (Figure 5.5A). In the upslope profile, the ^{10}Be concentration increases from ~2×10^{8} at the surface to ~4.6×10^{8} at/g at ~100 cm deep, and drops to 3.4×10^{8} at/g in the saprolite. In the midslope and toeslope positions, the variation of ^{10}Be with depth is more pronounced with higher peak values of ^{10}Be. Both profiles present a concentration of ~4×10^{8} at/g near the surface which increases to ~8×10^{8} at/g at 60 cm deep and then declines progressively with depth. In the saprolite, the ^{10}Be concentrations are similar (S-Top, S-LM) or lower (S-Bot) than at the surface, and significantly higher than the laboratory blank. The increasing concentration of the meteoric ^{10}Be with depth is indicative for leaching and chemical losses of ^{10}Be in the regolith profiles.

Table 5.2: Meteoric ^{10}Be concentrations and ^{10}Be inventories along the toposequence

General code	Sample code	^{10}Be (at/g) x10^{8} (±1σ)	Bulk Density (g/cm^{3})	^{10}Be inventoriy (at/cm^{2}) x10^{9}
	S-Top/10-20	2.04 ± 4.1	0.86	
	30-40	2.55 ± 5.1	1.02	
ILSTR2	55-65	3.12 ± 6.2	0.93	61.92
	95-105	4.59 ± 9.2	1.01	
	155-160 (S)	3.40 ± 6.8	1.70	
	S-LM/10-20	3.71 ± 7.4	1.14	
	30-40	3.87 ± 7.7	1.28	
	55-65	7.74 ± 15.5	1.16	
ILSLMR2	95-105	6.59 ± 13.2	1.37	177.43
	180-195	5.54 ± 11.1	1.38	
	235-240 (S)	3.62 ± 7.2	1.70	
	S-Bot/10-20	4.21 ± 8.4	1.06	
	30-40	5.85 ± 11.7	1.16	
	55-65	8.47 ± 16.9	0.97	
ILSBR1	95-105	5.86 ± 11.7	1.29	236.27
	180-190	4.24 ± 8.5	1.45	
	280-285 (S)	3.17 ± 6.3	1.70	
	395 400 (S)	2.30 ± 4.6	1.90	
	Composite Sample			
ILSTR1	S-Top1	3.27 ± 6.5	0.76 [a]	48.17[b]
ILSTR3	S-Top3	3.83 ± 7.7	0.91[a]	52.92[b]
ILSLMR1	S-LM1	5.06 ± 10.1	1.06 [a]	148.62[b]
ILSLMR3	S-LM3	3.54 ± 7.1	1.08 [a]	100.98[b]
ILSBR2	S-Bot2	5.61 ± 11.2	1.03 [a]	227.90[b]

[a]: density values presented here is average values.
[b]: ^{10}Be inventories have been calculated with detailed sample thicknesses and bulk densities which are not presented here with a view of simplification.

The total meteoric ^{10}Be inventories increase along the slope (Figure 5.5B), from 60 × 10^{9} at/cm² at the upslope to 177 × 10^{9} at the lower middle and 236 × 10^{9} at the toeslope position. The ^{10}Be inventories from the composite samples show a similar pattern with mean values of 51 × 10^{9} at the top, 125 × 10^{9} at the lower middle and 227 × 10^{9} at/cm² at the toeslope. However, the data from the composite samples are systematically lower than the depth-integrated samples. The latter is probably related to a bias in the amalgamation method while we have carefully taken into account differences in density and sampling thickness. The downslope increase of total ^{10}Be inventory suggests transport and accumulation of soil particles, and meteoric ^{10}Be, along the hillslope.

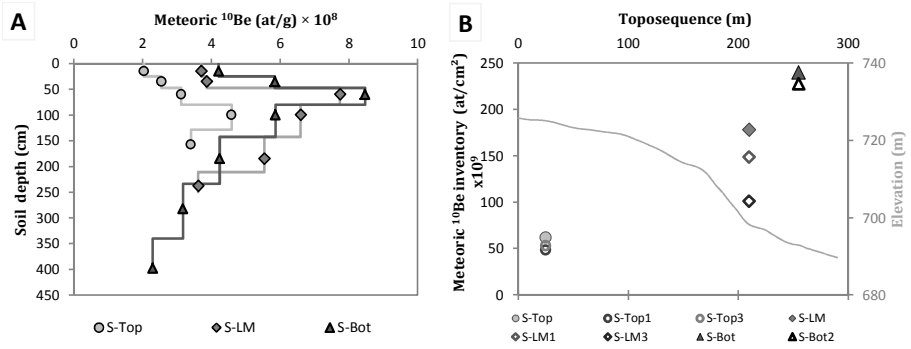

Figure 5.5: (A) Meteoric ^{10}Be concentration profiles measured along the steep slope transect. (B) Total meteoric ^{10}Be inventories of the eight regolith profiles along the hillslope transect indicating the increase of the concentration downslope.

Constraining surface denudation rates

When making abstraction of potential losses of meteoric ^{10}Be in the regolith profiles, the inventories of ^{10}Be in the regolith profiles can be used to provide estimates of soil residence time and surface denudation rates following equations 5.2 and 5.3. Results are presented in the table 5.3 for the three profiles located on the upslope portion of the catchment (S-Top, S-Top1 and S-Top3). The apparent residence time is higher (90 ± 2 kyr) for S-Top than for the composite samples (77 ± 2 and 70 ± 1 kyr) while the denudation rates are ranging from 36 ± 1 to 46 ± 1 mm/kyr. The mean residence time and mean denudation rate are estimated at 79 ± 10 kyr and 40 ± 5 mm/kyr.

Table 5.3: Meteoric ^{10}Be inventories, residence time of the meteoric ^{10}Be and denudation rates for the upslope profiles.

	$I_{^{10}Be}$ (at/cm^2) × 10^{10} (± 1 st. dev.)	Residence time of ^{10}Be (kyr)[a] (± 1 st. dev.)	Denudation rate (mm/kyr) (± 1 st. dev.)
S-Top	6.19 ± 0.14	90.5 ± 2.0	38.2 ± 0.9
Composite samples			
S-Top1	4.82 ± 0.10	70.0 ± 1.4	46.2 ± 1.1
S-Top3	5.29 ± 0.11	77.1 ± 1.6	35.9 ± 0.8

[a] assuming a meteoric ^{10}Be delivery rate (q) of 7.0 × 10^5 at cm^{-2} yr^{-1} [*Willenbring and von Blanckenburg*, 2010]

Alternatively, the concentration of in-situ produced ^{10}Be concentrations in the upslope profiles can be used to provide in-situ produced ^{10}Be-derived denudation rates. As the samples were taken at depth, the ^{10}Be concentrations were corrected for soil shielding

using the values mentioned in Table 5.4. The ^{10}Be concentration in the horizon 25-45 cm of the profile G-Top4 and S-Top6, the concentrations are above 6.3 ± 0.1 at. g_{qtz}^{-1} while it is lower in the profile S-Top1 with 1.9 ± 0.2 at. g_{qtz}^{-1}. The concentration measured in the horizon 60-80 cm in the profile S-Top1 is higher than in the horizon 25-45 cm and equals 3.7 ± 0.1 at. g_{qtz}^{-1}. The long term surface denudation rates of the latter profile do not change significantly with the sampling depth (1.6 ± 1.2 and 5.2 ± 2.9 mm/kyr). In the three upslope regolith profiles, in-situ ^{10}Be derived denudation rates range between 0.2 and 5.2 mm/kyr (Table 5.4).

Table 5.4: In-situ ^{10}Be concentration and denudation rates from upslope profiles of the toposequence.

Sample code	Elevation (m)	^{10}Be concentration (× 10^6 at.g_{qtz}^{-1}) (± 1σ)	Soil shielding factors	Corrected ^{10}Be concentration (× 10^6 at.g_{qtz}^{-1}) (± 1σ)	Topographic shielding factor [*Norton and Vanacker*, 2009]	^{10}Be denudation rates (mm kyr^{-1}) (± 1σ)
S-Top1/60-80	726	3.74 ± 0.10	0.74	5.05 ± 0.13	0.999	1.6 ± 1.2
S-Top1/25-45	726	1.99 ± 0.20	0.86	2.23 ± 0.24	0.999	5.2 ± 2.9
G-Top4/25-45	714	6.33 ± 0.14	0.82	7.70 ± 0.17	0.999	0.5 ± 0.6
S-Top6/25-45	718	8.34 ± 0.20	0.84	9.92 ± 0.23	0.999	0.2 ± 0.5

DISCUSSION

Relationship between ^{9}Be chemical fractions and meteoric ^{10}Be in regolith profiles

Results from the sequential extraction of ^{9}Be fractions put forward two interesting aspects (i) the distribution of reactive ^{9}Be fractions with depth shows a be-shaped curve with a maximum at 60 to 100 cm deep, and (ii) the concentration of exchangeable, reactive and residual ^{9}Be chemical fractions increases systematically along hillslope (Figure 5.3, Table 5.1). The concentrations of reactive and total ^{9}Be are strongly correlated with the meteoric ^{10}Be concentrations in the regolith profiles (Figure 5.4 and 5.5). Our data show a significant correlation between the meteoric ^{10}Be concentrations and the concentrations of $^9Be_{am\text{-}x}$, $^9Be_{x\text{-}ox}$ and total ^{9}Be with a correlation coefficient of respectively 0.91, 0.68 and 0.75 (n = 18), while the correlation with $^9Be_{ex}$ and $^9Be_{residual}$ is very low (i.e. resp. 0.06 and -0.01, n = 18). The peak concentration of the $^9Be_{am\text{-}x}$ and $^9Be_{x\text{-}ox}$ fractions occurs at 55 to 65 cm deep in the regolith profiles, which coincides with the depth of maximum meteoric ^{10}Be concentrations. In the upslope profile the reactive

^{9}Be fractions and the meteoric ^{10}Be have a maximum at greater depth, 95-105 cm. It suggests that the meteoric ^{10}Be behaves similar as the amorphous oxy-hydroxide and the crystalline oxide ^{9}Be chemical fractions which is in agreement with the results presented by *Wittmann et al.* [2012].

The depth-variation of the reactive ^{9}Be fractions is illustrative for the chemical alteration of the regolith during soil development. In the regolith profiles, the Bt horizon is well recognizable (50-80 cm), and translocation of clay minerals, Aluminum and Iron oxides is notable (*Chapter III*), which can reasonably explain the accumulation of Beryllium at this depth as it readily sorbs on these minerals [*Pavich et al.*, 1984; *Wyshnytzky et al.*, 2015]. Translocation of clay, dissolved organic matter (DOC) and Al-Fe oxy-hydroxides is characteristic for the pedogenesis of Alisol and Acrisol, and has been reported in similar environments [i.e. *Krasilnikov et al.*, 2005; *Bacon et al.*, 2012; *Caner et al.*, 2014]. Geochemical analyses help us to better understand the depth-distribution of Beryllium in our regolith profiles. We explicitly refer to *Chapter III* for a detailed description of the soil chemical analyses of the regolith profiles in the southern Brazil Critical Zone Observatory. Regression analyses on the soil chemistry data indicate that the chemical fractions of ^{9}Be are positively correlated with the concentrations of base cations such as Ca, Mg, Mn and Na, and negatively with the loss on ignition (LOI, Table 5.5). The positive association of the ^{9}Be fractions with the basic cations in the soil samples suggests that Beryllium is retained on the same exchanges sites in cation-bearing clays. The negative association of the ^{9}Be chemical fractions with the organic matter and carbonate content (lost by ignition) indicates that the presence of soil organic acids enhances chemical leaching. Our data are consistent with earlier results presented in *Jungers et al.* [2009].

Table 5.5: Cross correlation coefficient matrix between the ^{9}Be chemical fractions (ng/g) and the element concentrations (mg/kg) of the basic cations for the three regolith profiles that were analyzed in depth. We refer to Chapter III for the geochemical analyses of the soil samples.

	Mg	**Mn**	**Na**	**Ca**	**LOI**
^{9}Be ex	0.39	0.56	0.43	0.51	-0.54
^{9}Be Am	0.18	0.40	-0.28	0.00	-0.01
^{9}Be Ox	0.64	0.43	0.37	0.51	-0.39
^{9}Be Res	-0.05	0.86	0.30	0.40	-0.61
^{9}Be	0.31	0.66	0.08	0.32	-0.35

The concentration of exchangeable, reactive and residual ^{9}Be chemical fractions increases systematically along hillslope. The increase is most noticeable in the

exchangeable and amorphous oxy-hydroxide fractions that increase – on average - by factor 7, and lower in the crystalline oxide and residual fractions that increase by a factor ~1.8 (Table 5.1). The downslope increase in ^{9}Be chemical fractions is similar than the increase in meteoric ^{10}Be inventories along slope which increase by a factor ~1.8. This observation supports the downslope transport of Beryllium associated with transport of soil particles, aggregates and solutes in the soil system.

Chemical mass fluxes of ^{9}Be to correct denudation rates

When assuming that Beryllium is conservative in the soil system, the meteoric ^{10}Be inventories suggest a mean residence time of 79 ± 10 kyr and a denudation rate of 40 ± 5 mm/kyr for three upslope regolith profiles (Table 5.3). Such denudation rates are remarkably high for the gently sloping hill that is covered by native forests, and are not at all supported by the in-situ ^{10}Be-derived denudation rates for the same sites. The strong association between the concentrations of meteoric ^{10}Be and reactive ^{9}Be fraction in the soil, and the significant ^{9}Be mass flux in the regolith profiles suggests that the retention of Beryllium to soil particles is not complete. A significant part of the meteoric ^{10}Be is translocated and/or leached from the regolith profile as the concentrations do not decrease monotonically with depth [Pavich et al., 1984; McKean et al., 1993; Balco, 2004] (Figure 5.4 and 5.5A). This leads to an underestimation of the residence time and an overestimation of the denudation rates.

The information from the ^{9}Be chemical fractions is here used to correct for the incomplete retention of meteoric ^{10}Be in the regolith profiles. Given that the amorphous oxy-hydroxides and crystalline oxides fractions are the main carriers of meteoric ^{10}Be, the total meteoric ^{10}Be inventory ($I_{^{10}Be}$) of the regolith profiles has been corrected based on the mass losses of the reactive ^{9}Be fractions. The correction for poor retention of meteoric ^{10}Be indicates that 51% of the meteoric ^{10}Be is not retained in the regolith profile (Table 5.3 and 5.6). After correction, the total meteoric ^{10}Be inventory increases by a factor of 2.05 (Table 5.6). The corrected soil residence time is 2 times higher (mean: 165 ± 22 kyr), and corrected denudation rate is 10 times lower (mean: 4.8 ± 0.5 mm/kyr) compared to the non-corrected values (Table 5.3).

Table 5.6: Mass fluxes of reactive ^{9}Be fractions ($m_{reac^{9}Be,\,flux}$ includes $^{9}Be_{am\text{-}x}$ + $^{9}Be_{x\text{-}ox}$) are used to correct the meteoric ^{10}Be inventories ($I'_{^{10}Be}$) for upslope profiles of the toposequence. The corrected meteoric ^{10}Be inventories are on average 2.05 times higher than the uncorrected inventories ($I_{^{10}Be}$), residence time of the meteoric ^{10}Be is increased in the same proportion while denudation rates are 10 times lower.

Sample code	$m_{reac^{9}Be,\,fl}$ (at/cm²) × 10^{18}	$I_{reac^{9}Be}$ (at/cm²) × 10^{18}	$I'_{^{10}Be}$ (at/cm²) x10^{11}	Corrected residence time (kyr)[a] (± 1 st. dev.)	Corrected denudation rate (mm/kyr) (± 1 st. dev.)
S-Top	-3.04	2.90	1.23	185 ± 95	4.9 ± 0.5
Composite samples					
S-Top1	- 3.04	2.90	0.98	146 ± 72	5.0 ± 0.5
S-Top3	-3.04	2.90	1.08	161 ± 80	5.0 ± 0.5

[a] assuming a meteoric ^{10}Be delivery rate of 7.0 × 10^{5} at cm^{-2} yr^{-1} [*Willenbring and von Blanckenburg*, 2010]

After correction for poor retention of meteoric ^{10}Be, the denudation rates of the three upslope profiles are 4.9 ± 0.5, 5.0 ± 0.5 and 5.0 ± 0.5 mm/kyr. These values are far more consistent with the in-situ ^{10}Be-derived denudation rates that range between 0.2 ± 0.5 and 5.2 ± 2.9 mm/kyr for the landscape convexities, and with reference values from literature. For deeply weathered ancient soils on plateau surfaces, earlier studies have published denudation rates of 1 to 10 mm/kyr for lateritic profiles in central Brazil, the West African Craton and high plateau of Sri Lanka [*Braucher et al.*, 1998a; *Braucher et al.*, 1998b; *Vanacker et al.*, 2007].

In deeply weathered ancient soils such as the Acrisol and Alisol in the Brazil CZO, the use of ^{9}Be chemical fractions to correct for incomplete retention of meteoric ^{10}Be in the regolith profiles leads to important corrections of the ^{10}Be inventories. Similar observations were made by *Bacon et al.* [2012] for a highly weathered Utisol in Southern Piedmont: they estimated that >30% of the total ^{10}Be is leached out of the soil system. According to numerical simulations by *Campforts et al.* [2016], the redistribution of meteoric ^{10}Be in soils with low retentivity is related to chemical mobility encompassing adsorption and desorption reactions and clay translocation. A potential caveat of using reactive ^{9}Be mass losses to correct for incomplete retention of meteoric ^{10}Be is related to the different pathways of ^{9}Be and ^{10}Be isotopes within the regolith profile. Meteoric ^{10}Be is delivered to the top of the regolith profile, while ^{9}Be is released from mineral weathering. As physicochemical conditions for weathering may vary considerably within the regolith profile, the spatial separation of the Beryllium isotope sources can introduce bias. In recent work by *Maher and von Blanckenburg* [2016], the discrepancy between

reactive ^{9}Be and meteoric ^{10}Be mass loss can reach up to 30% in soils with strong biogeochemical gradients, leading to overcorrection of surface ages and denudation rates. Soil pH has been identified as one of the key variables controlling Be sorption in the weathering profiles. In our study site, the soil pH shows little variation with depth ($\Delta pH_{H2O} < 1$, *Chapter III*) which likely minimizes the potential discrepancy between ^{9}Be and meteoric ^{10}Be mass losses. More work is needed to integrate the results from this study with reactive transport models.

CONCLUSION

For deeply weathered soils in southern Brazil, meteoric and in-situ produced ^{10}Be isotopes were used to constrain long-term denudation rates. Given that incomplete retention of meteoric ^{10}Be in the regolith profiles, it can lead to overestimation of the denudation rates. Wee apply a method that is based on the chemical behavior of the stable isotope, ^{9}Be, to correct for incomplete retention of meteoric ^{10}Be. Along a toposequence, three regolith profiles were analyzed in great detail, together with five replicate profiles located at upslope, midslope, and toeslope positions. The depth variation in the exchangeable, reactive and residual ^{9}Be fractions show that Beryllium is mobilized within the regolith profile by the amorphous oxy-hydroxide and crystalline oxide fractions. Translocation and leaching of Be increase along hillslope, with the highest ^{9}Be mass fluxes measured at the lower midslope and toeslope positions.

Based on the strong agreement in depth-variation of the reactive ^{9}Be and meteoric ^{10}Be concentrations, the reactive ^{9}Be mass losses were used to correct for the incomplete retention of meteoric ^{10}Be. Our data suggest that losses of the total ^{10}Be inventories of the upslope regolith profiles are important, and reach up to 51%.

Surface denudation rates derived from corrected meteoric ^{10}Be inventories equal 5.0 ± 0.5 mm/kyr, and are in agreement with in-situ ^{10}Be-derived denudation rates (<5 mm/kyr). Our study confirms that meteoric ^{10}Be is a useful geochronological technique that can be applied in a wider range of environments than in-situ produced ^{10}Be. However, it also shows that correction of the meteoric ^{10}Be inventories is necessary to account for incomplete retention of Be within the regolith profile.

Chapter VI

Synthesis & Outlook

SYNTHESIS

Nowadays it is accepted that constituents of the Earth's surface are rapidly changing in response to anthropogenic perturbations. Among them the fate of the soil is probably one of the most critical as it supports life and provides the primary resources to a growing population. It is therefore important to intensify the research related to the understanding of the soil system [*Anderson et al.*, 2010]. Our knowledge of the response of the soil system to perturbations is limited because the research in soil science was, until recently, discipline-oriented and had to cope with spatial variability and vast temporal scale. The concept of Critical Zone proposed by the *National Research Council* [2001] offers the opportunity to integrate the soil together with other directly related disciplines such as geology, hydrology, biology, geomorphology, climatology. It is essential to make a step forward in the understanding of the functioning of this system because the range of preserved soils from anthropogenic impacts is being reduced years after years. Several initiatives are generated such as an increasing number of Critical Zone Observatories. In this context, the SOGLO project was designed with a multi-disciplinary approach in order to integrate different expertise in this scientific domain.

In an attempt to contribute to the soil system knowledge, the aim of the present thesis was to constrain natural soil formation and development on longer time scale (10^3 to 10^5 years) in order to provide a baseline reference for distinguishing human impact on the soil system. First, chemical weathering and physical erosion rates were measured and the limiting factors of their relation were explored (*Chapter II and III)*. In the *Chapter IV*,

the steady-state hypothesis of the soil thickness was tested in thin soils of the Betic Cordillera (Spain) by the comparing data from U-series disequilibrium and in-situ ^{10}Be. Then, meteoric ^{10}Be was used as a geochemical tracer for quantifying long-term soil denudation rates. Given the low retention of meteoric ^{10}Be in highly weathered soil profiles, a recent laboratory protocol involving sequential extraction of ^{9}Be from the mineral reactive phases was developed and tested. The purpose was to correct concentrations of meteoric ^{10}Be for losses in order to derive the soil denudation rates (*Chapter V*).

Constraining long term soil processes

Being able to constrain long term soil weathering and denudation in various environments is crucial for understanding long-term landscape evolution and dynamics of nutrient cycling in soil systems.

In the *Chapter II*, weathering and denudation rates were quantified for nine soil profiles located on convex ridge crests of three mountain ranges in the Spanish Betic Cordillera. To constrain chemical weathering intensities and long-term denudation rates, we combined a geochemical mass balance (CDF) with in-situ ^{10}Be cosmogenic nuclides. In the Betic Cordillera, surface denudation rates range between 14 and 109 mm/kyr with higher denudation rates in the youngest and the most recently uplifted Sierra and systematically lower values in other mountain ranges. Chemical weathering losses account for ~5 to 30 % of the total mass lost by denudation and are (i) negatively correlated with mean annual temperature, evapotranspiration and denudation (ii) positively correlated with soil thickness and soil residence time. These observations support a kinetically limited regime between the weathering and the denudation in the Betic Cordillera. Under the semi-arid conditions in South-East of Spain (MAP: 275-425 mm/yr; ETp: 800-900 mm/yr; Table 1.1), we considered mineral residence time and water balance in the soil system as the two most important factors controlling chemical weathering processes.

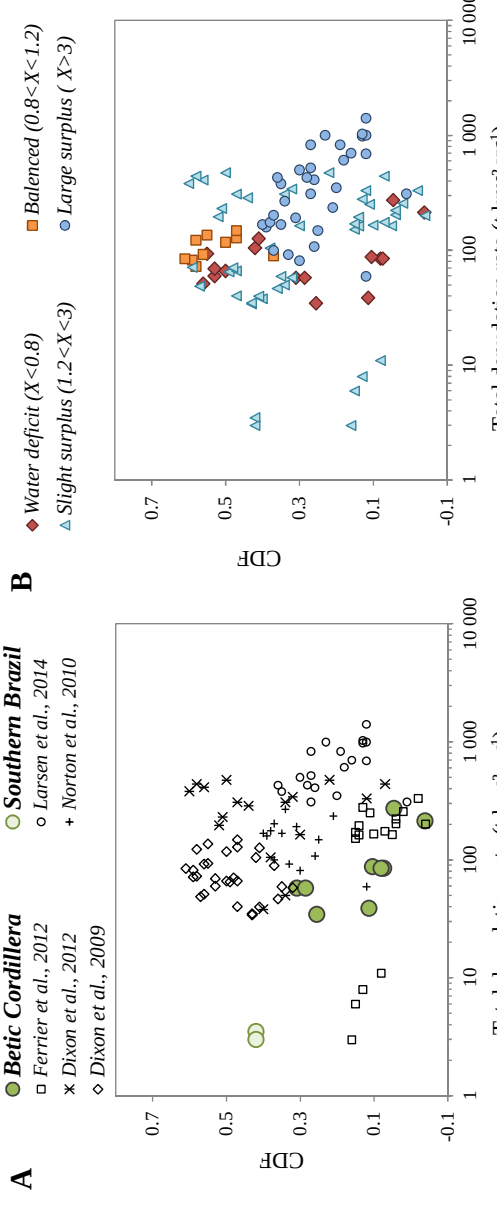

Figure 6.1: Illustration of the soil weathering intensities and denudation rates that have been collected during the four years of research. By filling a gap in the dataset, they help to better understand the relation between weathering and denudation.

By plotting chemical depletion fractions against total denudation rates for a worldwide data set covering a wide range of environmental conditions, we were able to explore the relationship between weathering and erosion (*Chapter II*). No general correlation could be established between these processes (Figure 6.1A). But the importance of the controlling factor "water availability" can be put forward with a classification of the data set based on soil hydrological conditions (ET_p, Figure 6.1B). An important implication of this finding is that it reinforces the idea that climatic regimes may strongly regulate the relation between weathering and erosion among the different environments of the Earth.

The controlling factors of the weathering processes may vary at the spatial scale of study area. In the *Chapter III*, the soil development was quantified for two toposequences (~250 m long) with contrasted slope gradients in southern Brazil. Our observations showed an increase of the soil development with the distance from the ridge crest. The downslope mass fluxes have been quantified and increased significantly towards the footslope sections of both toposequences. This results from the combination of in-situ weathering of the regolith profile and downslope transport of weathering products (soil particles and solutes fluxes). Contrasts between weathering processes are also visible between the hillslopes. We measured higher mass losses at the bottom of the steeper toposequence with fluxes >30% higher than at the same section of the gentle hillslope. Therefore, at the hillslope scale, we considered the topographic gradient as the most important controlling factor of the weathering processes. The quantification of the soil weathering mass losses will be helpful to constrain hillslope numerical models.

In the *Chapter IV*, the purpose was to verify the soil thickness steady-state hypothesis. Literature on chemical weathering often assumes that soil production equals denudation on stable sites but it has rarely been validated with empirical field data. Soil development was constrained for three soil profiles developed on convexities in the Betic Cordillera using a combined approach based on in-situ produced cosmogenic radionuclides and U-series disequilibria. The results from two soil profiles showed that magnitude of soil production rates inferred from U-series isotopes (24 ± 5 and 7 ± 1 mm/kyr) is in the same order of magnitude as the ^{10}Be-derived denudation rates (23 ± 3 and 14 ± 2 mm/kyr). The steady state soil thickness appears to be a valid hypothesis for these two sites (Sierra de las Estancias and Sierra de los Filabres). In the third soil profile (Sierra Cabrera), denudation largely exceeds soil production indicating soil thinning. The results from this work underline the precautions to take when pretending that the soil thickness of a study site is at steady-state.

Progress was made regarding the applicability of the U-series disequilibrium: the *Chapter IV* was one of the first studies applying this method in very shallow soils (< 60 cm thick) that developed on low grade metamorphic rocks in semi-arid climatic conditions. Our results confirmed the great potential of the method to investigate the soil production and the advance of the weathering front into the bedrock. The *Chapter IV* also underlines the interest of combining independent methods in order to better constrain the development of soil. The coupling of U-series with in-situ produced radionuclides has provided new insights in the rates of soil development by allowing an independent quantification of the production and the surface denudation of the soil. The combination of independent methods has also been used in other chapters (*II* and *V*) with the coupling of chemical mass balance (CDF, Tau, $m_{Be\ fluxes}$) and ^{10}Be radionuclides in order to constrain soil chemical mass losses, weathering rates and surface denudation rates. Our studies, like those of *Riebe et al.* [2004]; *Dixon et al.* [2009]; *Ferrier et al.* [2010]; *Ackerer et al.* [2016] take benefits of several chemical techniques and demonstrate the interest of combining methods to further advance our understanding of soil processes.

With the *Chapter V*, we improved the applicability of meteoric ^{10}Be to constrain long term soil denudation rates in highly weathered soils. In southern Brazil, under the sub-humid tropical climate, the behavior of the Beryllium within the soil profile was studied from three regolith profiles along a toposequence and the surface denudation rates were quantified on the upslope section. Insights from the sequential extraction showed that in soil Beryllium is mainly carried by the crystalline oxide and amorphous oxy-hydroxide fractions. Our results have also pointed the vertical leaching of the meteoric ^{10}Be through the regolith and the downslope transport with accumulation at the toeslope section of the toposequence. Inventories of meteoric ^{10}Be were corrected for losses after quantification of the mass losses. We estimated that losses of meteoric ^{10}Be on the convexity are over 50%. Soil surface denudation rates obtained from meteoric ^{10}Be and corrected for the losses are <5 mm/kyr, and correspond to the rates derived from an independent method, i.e., in-situ ^{10}Be (5-1 mm/kyr). This confirmed the high potential of the meteoric ^{10}Be method to constrain long term surface denudation rates if weathering losses of ^{10}Be are taken into account. This study shows that losses of meteoric ^{10}Be cannot be ignored in highly weathered environment and correction methods are relevant for the applicability of meteoric ^{10}Be in the future.

OUTLOOK

As mentioned in the introduction of this manuscript, the (de)coupling between chemical weathering and physical erosion in various environmental settings has to be clarified because it directly affects the intensity of silicate weathering, and thereby, it has direct implications for the global biogeochemical cycles. On a geological time scale, the weathering of silicate minerals of rocks and soils consumes atmospheric CO_2 and contributes to draw down this greenhouse gas from the atmosphere *(Chapter I)*. However the exact relation between these two geomorphic processes remains unknown, and could be positive, nonlinear or negative according *Dixon and von Blanckenburg* [2012]. We have explored the relationship between weathering and erosion by looking at a selection of data taken from different environmental settings as the South-East of Spain and the southern Brazil (Figure 2.8 and 6.1). There obviously exists a wide scatter in the data set that limits further interpretation, and confounding variables such as lithology, rock rheology, vegetation cover, and topographic position that may affect the interpretation of statistical associations. But, at landscape scale, it appears that water availability could play a key role in this relation (Figure 2.1B). Therefore, for future research in the domain, it will be essential for chemical weathering and landscape evolution models to include soil water and solute fluxes. According to *Samouëlian et al.* [2012] most of the landscape soil development models [i.e. *Dietrich et al.*, 1995; *Minasny and McBratney*, 2001; *Goddéris et al.*, 2006; *Vanwalleghem et al.*, 2013] do not include water flow in their architecture. The second version of SoilGen paves the way in the right direction by taking an initial soil or parent material as a starting point of the soil formation but also by considering soil processes such as clay migration, precipitation and bioturbation including water or solute fluxes [*Yu et al.*, 2013; *Finke et al.*, 2015]. It is also important to apply such models across a wider range of soil hydrological conditions because it is crucial to expand existing field datasets on into less explored climatic and lithological settings. Until now literature about this topic has mainly explored temperate and tropical climates and granitic and basaltic terrains but more efforts could be made: in arid to semi-arid zones which account for one third of the land area [*UNSO/UNDP*, 1997] and in metamorphic lithologies which represent about 15% of the continental crust exposed at the surface. As it is underlined in the review of *Opolot et al.* [2015] about soil development models, the scientific community is calling for high quality dataset from chronosequence, climosequence and toposequence in order to calibrate and validates the models. We believe that the dataset collected and presented in this dissertation will contribute to that effort.

The discussion of the *Chapter III* raises another point which should be investigated by additional researches. Our data on chemical mass fluxes along two toposequences in southern Brazil show that the topography has a significant impact on soil chemical mass losses which increase towards the footslope. This situation is emphasized along the steep toposequence where mass losses at midslope and footslope are > 30% higher than in the gentle slope. Considering that both hillslopes are nearly identical (aspect, lithology, vegetation cover, precipitation) this result is a counter-intuitive, as usually the intensity of the weathering losses are proportional to the residence time of the soil which is supposed to be longer along the gentle hillslope. Our hypothesis is that this could be related to soil water fluxes flowing in the subsurface along the steep toposequence (related to the slope shoulder) and in the deep saprolite along the gentle toposequence where a significant portion of the weathering would take place. In order to validate this, data on water content and elementary fluxes through the profiles and along both toposequences are required.

The application of the U-series disequilibrium to the soils of the Betic Cordillera illustrated the potential frontiers of the method to track soil production in rapidly eroding landscapes characterized by thin weathering depths *(Chapter IV)*. It appears that the mechanisms of uranium fractionation through bedrock and soil weathering are difficult to grasp in shallow soil, as the numerical U-series fractionation model is currently under-constrained. First, it would be better for future studies to focus on homogenous weathering layer (i.e. saprolite) in order to avoid potential effect of multi fractionations induced with the secondary minerals formation. It would also be important to investigate into more details the impact of the air/dust/sea spray inputs on the soil profiles, as this could potentially weaken the reliability of the obtained rates by enriching activity ratios near the soil surface and imposing more constrains to the U-series. Finally, the climatic history of the soil observatory should be taken into account when using U-series disequilibrium method. It is indeed necessary to ensure that weathering conditions of the soil have been kept constant over the residence time of the weathering products otherwise it could induce other fractionations and reset the radioactive clock. Despite all these conditions for a suitable study site, we believe that Uranium radioactive disequilibrium will continue to emerge as a performing tracer and chronometer of soil weathering processes. This is confirmed by the recent work of *Ackerer et al.* [2016] where the soil production rates is quantified in the CZO of the Strengbach catchment in France.

Accumulation of meteoric ^{10}Be in regolith mantle is a powerful and recognized tracer for quantifying long term geomorphic processes [i.e. *McKean et al.*, 1993; *Willenbring and von Blanckenburg*, 2010; *West et al.*, 2013]. Compared to in-situ ^{10}Be it has two enormous advantages: a higher concentration in the regolith (lower amount of sample to be processed) and an applicability to quartz free lithologies. But applications of this tracer are compromised by a low retention behavior of the Be nuclides in acid soils which cover 30% of the global land surface and which are commonly formed in (sub)tropical zones or at high latitude [*Merry*, 2009]. The *chapter V* illustrated the importance of the losses of meteoric ^{10}Be in acidic soil profiles developed in southern Brazil (more than 50% of the total inventory). From now, studies should be aware of this point and can no longer neglect Be loss in order to constrain geomorphic processes. For the moment, there exist no straightforward methods to account for losses of meteoric ^{10}Be but recent studies are exploring different ways. The approach proposed in *chapter V* seems to be a promising method but it should first be validated in others environmental settings as tropical or boreal forest where soils are generally strongly acid and the potential caveat related to the used of ^{9}Be should be investigated. The approach proposes by the Be2D model, developed by *Campforts et al.* [2016], is another interesting option. This model goes even further by simulating over time vertical and lateral redistribution of soil particles and meteoric ^{10}Be with the purpose to capture variations of Be concentration through the regolith. In conclusion, whatever the way chosen to integrate the Be losses from the soil profile, it will be essential to account for them in order to use the meteoric ^{10}Be tracer more routinely.

Throughout all of this study, our data have shown the importance of the processes occurring at the weathering front where the bedrock is fragmented and where the outer surface of the primary minerals begins to be weathered. For example, the shift of the Uranium activity ratios in the Betic Cordillera (Figure 4.4) or the sharp enrichment of the immobile elements in southern Brazil (Figure 5.5) occurred at bedrock-regolith interface. This attests that significant chemical transformations happen on a few centimeters only. At this time, very few studies have looked into this specific question although the data presented by *Anderson et al.* [2002] and *Pelt et al.* [2008] underline that the weathering front is a site where significant chemical transformations take place. We believe that future studies should place more emphasis on this relatively understudied domain.

Annexes VII

Supporting Information

CHAPTER II

Table SI 2.1: Elemental concentrations in regolith profiles

Sample ID	Depth	Al %	Ca %	Fe %	K %	Mg %	Na %	Si %	Ti %	Zr mg/kg	LOI (%)
EST-A-U1	7	4.73	0.25	2.19	0.99	0.39	0.33	37.37	0.37	304.6	4.35
EST-A-U2	13	5.53	0.28	2.64	1.04	0.48	0.26	36.55	0.44	283.9	3.71
EST-A-U3	21	7.87	0.49	4.01	1.57	0.74	0.29	32.46	0.46	263.6	4.65
EST-A-U4	29	8.71	0.50	4.70	1.83	0.89	0.28	30.63	0.43	222.4	5.48
EST-A-U5	33	9.92	0.63	5.26	2.37	1.01	0.67	28.09	0.49	238.1	6.17
EST-A-UR	92.5	12.74	0.64	4.72	3.86	0.20	0.80	26.82	0.58	210.3	3.15
EST-C-U1	4	6.62	0.53	3.06	1.54	0.79	0.55	33.50	0.45	324.7	5.61
EST-C-U2	13	7.27	0.47	3.70	1.64	0.81	0.32	33.02	0.46	289.4	4.74
EST-C-U3	20	9.63	0.61	5.39	2.47	1.02	0.33	28.51	0.50	270.0	5.94
EST-C-U4	28	10.19	0.58	5.15	2.89	0.92	0.42	28.32	0.54	285.1	5.12
EST-C-U5	39.5	10.05	0.54	4.73	2.92	0.79	0.47	30.48	0.54	282.8	1.54
EST-C-U6	49.5	9.61	0.56	5.08	2.75	0.89	0.41	29.33	0.51	268.7	4.43
EST-C-R	82.5	13.25	0.67	5.19	3.90	0.22	1.05	25.77	0.65	232.0	3.50

Sample ID	Depth	Al %	Ca %	Fe %	K %	Mg %	Na %	Si %	Ti %	Zr mg/kg	LOI (%)
FIL1-A-U1	3	8.85	0.32	4.51	2.44	0.58	1.28	29.82	0.55	219.5	5.65
FIL1-A-U2	7	9.51	0.31	4.83	2.56	0.62	1.28	29.08	0.56	207.5	5.30
FIL1-A-U3	10	9.31	0.32	4.78	2.65	0.64	1.26	29.30	0.57	234.8	5.11
FIL1-A-U4	12	9.55	0.30	4.76	2.62	0.61	1.28	29.13	0.58	217.6	5.17
FIL1-A-R	43	12.33	0.60	5.97	3.31	0.88	1.79	25.23	0.57	203.8	3.89
FIL1-B-U1	4	8.25	0.33	4.15	1.70	0.56	1.70	31.03	0.58	318.8	5.03
FIL1-B-U2	7	8.30	0.31	3.96	1.73	0.56	1.67	31.27	0.55	331.5	4.76
FIL1-B-U3	11	8.70	0.32	4.08	2.02	0.67	1.54	30.56	0.53	288.8	4.98
FIL1-B-U4	15.5	9.20	0.28	4.14	2.25	0.84	1.13	30.36	0.52	277.4	4.50
FIL1-B-R	25	4.23	0.12	1.89	0.57	0.54	1.95	38.79	0.23	279.4	1.20
FIL1-C-U1	4	8.79	0.45	4.38	2.08	0.58	0.98	30.05	0.51	289.3	6.14
FIL1-C-U2	9	8.86	0.31	4.50	2.03	0.58	0.96	30.27	0.49	296.3	5.69
FIL1-C-U3	13	8.92	0.32	4.41	2.07	0.60	0.91	30.45	0.47	278.1	5.35
FIL1-C-R	40	5.66	1.27	2.37	0.76	0.25	1.29	36.53	0.37	271.9	1.76
FIL2-A-U1	3	7.49	0.36	4.26	1.84	0.51	0.65	31.03	0.90	373.9	6.88
FIL2-A-U2	8	8.33	0.36	4.40	2.01	0.48	0.70	30.42	0.93	350.4	6.12
FIL2-A-U3	11	8.74	0.40	4.37	2.17	0.49	0.75	30.06	0.92	386.3	5.84
FIL2-A-U4	16	9.18	0.38	4.47	2.22	0.51	0.76	29.54	0.88	338.1	6.02
FIL2-A-U5	24	9.83	0.41	4.41	2.43	0.53	0.81	28.81	0.73	339.0	6.33
FIL2-A-R	30	10.32	0.10	4.76	2.56	0.68	0.94	29.08	0.61	269.5	4.34
FIL2-B-U1	5	6.96	0.51	3.66	1.85	0.53	0.74	31.95	0.66	326.5	6.87
FIL2-B-U2	11	7.68	0.36	4.23	1.89	0.58	0.78	31.76	0.67	310.6	5.13
FIL2-B-U3	17	7.55	0.34	4.16	1.88	0.56	0.78	32.26	0.77	346.8	4.26
FIL2-B-U4	24	8.60	0.61	4.18	2.13	0.58	0.89	30.95	0.59	319.8	4.50
FIL2-B-R	55	6.30	0.18	2.63	1.92	0.47	0.70	35.90	0.34	282.1	2.26
CAB-A-U1	1.5	12.10	2.35	6.29	2.51	1.02	0.53	22.97	0.81	213.3	8.43
CAB-A-U2	6	12.42	2.74	6.16	2.69	0.96	0.53	22.28	0.79	220.4	8.83
CAB-A-U3	11	11.93	3.51	6.33	2.63	0.88	0.50	21.52	0.74	219.8	10.42

CAB-A-U4	18	12.40	2.48	6.14	2.65	0.70	0.52	22.66	0.70	219.9	9.13
CAB-A-R[1]	57	12.29	0.37	6.21	3.17	0.98	0.80	25.12	0.66	225.0	5.17
CAB-B-U1	4	12.19	0.76	5.98	2.72	1.02	0.66	24.58	0.77	265.4	7.10
CAB-B-U2	6.5	11.28	1.41	5.46	2.53	1.01	0.59	25.44	0.70	212.2	7.29
CAB-B-U3	12	11.07	2.12	5.59	2.45	1.03	0.57	24.74	0.65	206.4	8.19
CAB-B-U4	18.5	10.88	2.28	5.03	2.37	1.01	0.61	24.94	0.57	231.4	8.87
CAB-B-R[1]	40	12.29	0.37	6.21	3.17	0.98	0.80	25.12	0.66	225.0	5.24
STD(BHVO)	-	6.8	7.9	8.3	0.4	4.2	1.7	22.9	1.6	170.9	-

[1]: Elemental concentrations (Zr include) were defined as the average from four rock samples.

Table SI 2.2: Fractional mass change for the major elements (Tau referred to Zr) (positive in case of mass gains and negative in case of mass losses)

Sample ID	τ-Al	τ-Ca	τ-Fe	τ-K	τ-Mg	τ-Na	τ-Si	τ-Ti
EST-A-U1	-0.74	-0.73	-0.68	-0.82	0.32	-0.71	-0.04	-0.56
EST-A-U2	-0.68	-0.68	-0.58	-0.80	0.73	-0.76	0.01	-0.45
EST-A-U3	-0.51	-0.39	-0.32	-0.67	1.87	-0.71	-0.03	-0.37
EST-A-U4	-0.35	-0.25	-0.06	-0.55	3.12	-0.67	0.08	-0.31
EST-A-U5	-0.31	-0.12	-0.01	-0.46	3.38	-0.26	-0.07	-0.25
EST-C-U1	-0.64	-0.43	-0.58	-0.72	1.55	-0.62	-0.07	-0.51
EST-C-U2	-0.56	-0.44	-0.43	-0.66	1.96	-0.76	0.03	-0.43
EST-C-U3	-0.38	-0.23	-0.11	-0.46	2.97	-0.73	-0.05	-0.35
EST-C-U4	-0.37	-0.30	-0.19	-0.40	2.41	-0.67	-0.11	-0.33
EST-C-U5	-0.38	-0.34	-0.25	-0.39	1.95	-0.63	-0.03	-0.32
EST-C-U6	-0.37	-0.28	-0.15	-0.39	2.49	-0.66	-0.02	-0.32
FIL1-A-U1	-0.33	-0.51	-0.30	-0.32	-0.38	-0.34	0.10	-0.11
FIL1-A-U2	-0.24	-0.49	-0.21	-0.24	-0.31	-0.30	0.13	-0.03
FIL1-A-U3	-0.34	-0.53	-0.31	-0.31	-0.37	-0.39	0.01	-0.14
FIL1-A-U4	-0.28	-0.53	-0.25	-0.26	-0.35	-0.33	0.08	-0.06
FIL1-B-U1	0.71	1.42	0.93	1.59	-0.08	-0.23	-0.30	1.19
FIL1-B-U2	0.65	1.21	0.77	1.54	-0.12	-0.28	-0.32	1.01
FIL1-B-U3	0.99	1.59	1.09	2.40	0.21	-0.23	-0.24	1.23
FIL1-B-U4	1.19	1.35	1.21	2.94	0.57	-0.42	-0.21	1.28

FIL1-C-U1	0.46	-0.67	0.74	1.56	1.19	-0.28	-0.23	0.31
FIL1-C-U2	0.44	-0.78	0.74	1.44	1.13	-0.31	-0.24	0.23
FIL1-C-U3	0.54	-0.75	0.82	1.65	1.35	-0.31	-0.19	0.25
FIL2-A-U1	-0.48	1.52	-0.36	-0.48	-0.46	-0.51	-0.23	0.07
FIL2-A-U2	-0.38	1.72	-0.29	-0.40	-0.46	-0.43	-0.20	0.18
FIL2-A-U3	-0.41	1.77	-0.36	-0.41	-0.50	-0.44	-0.28	0.06
FIL2-A-U4	-0.29	1.99	-0.25	-0.31	-0.40	-0.36	-0.19	0.15
FIL2-A-U5	-0.24	2.22	-0.26	-0.25	-0.39	-0.32	-0.21	-0.04
FIL2-B-U1	-0.04	1.38	0.20	-0.17	-0.01	-0.08	-0.23	0.67
FIL2-B-U2	0.11	0.80	0.46	-0.11	0.12	0.02	-0.20	0.78
FIL2-B-U3	-0.02	0.50	0.28	-0.20	-0.03	-0.09	-0.27	0.84
FIL2-B-U4	0.20	1.91	0.40	-0.02	0.09	0.12	-0.24	0.52
CAB-A-U1	0.06	5.84	0.09	-0.14	0.12	-0.28	-0.01	0.32
CAB-A-U2	0.06	6.71	0.04	-0.11	0.01	-0.31	-0.07	0.25
CAB-A-U3	0.02	8.91	0.07	-0.13	-0.06	-0.35	-0.10	0.17
CAB-A-U4	0.06	5.99	0.03	-0.13	-0.25	-0.32	-0.06	0.10
CAB-B-U1	-0.14	0.79	-0.17	-0.26	-0.10	-0.29	-0.15	0.01
CAB-B-U2	0.00	3.11	-0.05	-0.13	0.12	-0.21	0.10	0.15
CAB-B-U3	0.00	5.38	0.00	-0.14	0.16	-0.22	0.10	0.09
CAB-B-U4	-0.12	5.12	-0.19	-0.25	0.02	-0.25	-0.01	-0.14

Table SI 2.3: CRONUS calculator input

Sample ID	Lat.	Lon.	Mean Elev. (m)	Density ($g.cm^3$)	Shielding factor	^{10}Be Conc. ($at\ g^{-1}$)	^{10}Be Conc. uncertainty ($at\ g^{-1}$)	Soil Shielding factor
EST-C	37,5872	-2,1775	1187	2,5	0,99	108743	12937	1,58
EST-A	37,5872	-2,1775	1187	2,5	0,99	346758	21488	1,55
FIL1-C	37,2302	-2,1050	776	2,5	0,95	169032	10262	1,16
FIL1-A	37,2302	-2,1050	776	2,5	0,95	174359	13823	1,18
FIL3-A	37,1840	-2,0486	585	2,5	0,975	352496	31237	1,12
FIL2-B	37,3216	-2,3686	972	2,5	0,965	429765	22207	1,32
FIL2-A	37,3216	-2,3686	972	2,5	0,965	478512	24142	1,23
CAB-B	37,0607	-1,9379	525	2,5	0,945	46490	8332	1,17
CAB-A	37,0607	-1,9379	525	2,5	0,945	59539	7954	1,19

CHAPTER III

Table SI 3.1: Elemental concentration in regolith profiles (wt %)

Sample ID	Depth	Al_2O_3 %	Fe_2O_3 %	SiO_2 %	CaO %	K_2O %	MgO %	MnO %	Na_2O %	TiO_2 %	P_2O_5 %	Zr ppm	LOI
Gentle slope													
G-Top/0-10	5	11.5	6.9	66.9	0.3	0.6	0.5	0.1	0.2	1.2	0.11	417	11.4
G-Top/10-20	15	11.1	6.1	71.7	0.2	0.6	0.4	0.1	0.2	1.0	0.09	441	8.4
G-Top /20-30	25	11.7	6.3	71.5	0.1	0.5	0.4	0.1	0.2	1.1	0.08	456	7.9
G-Top /30-40	35	12.8	6.4	69.7	0.1	0.5	0.5	0.1	0.2	1.1	0.09	432	8.4
G-Top /40-50	45	13.2	6.6	69.1	0.1	0.5	0.4	0.1	0.1	1.1	0.08	459	8.5
G-Top /55-65	60	16.7	7.4	63.2	0.1	0.5	0.6	0.1	0.1	1.0	0.09	428	10.2
G-Top /75-85	80	20.1	7.3	58.2	0.1	0.6	0.7	0.1	0.2	0.9	0.09	376	11.6
G-Top/R	100	16.3	7.6	68.6	0.4	4.5	1.0	0.1	1.8	1.0	0.06	475	4.0
G-UM/0-10	5	10.2	6.6	68.7	0.3	0.8	0.3	0.1	0.3	1.1	0.14	441	11.2
G-UM/10-20	15	10.1	7.4	71.7	0.1	0.8	0.3	0.1	0.3	1.2	0.11	501	7.6
G-UM/20-30	25	10.8	7.5	71.3	0.1	0.8	0.3	0.1	0.3	1.3	0.11	473	7.3
G-UM/30-40	35	13.0	7.8	67.8	0.1	0.8	0.4	0.1	0.2	1.2	0.12	470	8.3
G-UM/40-50	45	17.0	9.1	60.7	0.1	0.7	0.5	0.1	0.2	1.1	0.13	424	10.2
G-UM/55-65	60	19.3	9.0	57.5	0.1	0.6	0.5	0.1	0.1	1.1	0.11	394	11.4
G-UM/75-85	80	18.8	8.8	59.3	0.1	0.6	0.5	0.1	0.1	1.1	0.09	413	10.4
G-UM/95-105	100	18.1	8.9	60.9	0.1	0.5	0.5	0.1	0.1	1.2	0.08	428	9.2
G-UM/130-140	135	17.8	8.4	62.3	0.0	0.6	0.5	0.1	0.2	1.2	0.07	424	8.6
G-UM/R	185	16.6	8.9	63.6	0.1	1.1	0.5	0.1	0.4	1.2	0.09	430	7.1
G-LM/0-10	5	9.8	5.4	68.8	0.5	0.9	0.3	0.1	0.2	1.0	0.1	448	12.7
G-LM/10-20	15	8.8	5.7	75.8	0.1	0.9	0.3	0.1	0.3	1.2	0.1	526	6.5
G-LM/20-30	25	8.8	5.8	76.5	0.1	0.9	0.3	0.1	0.3	1.2	0.1	533	5.7
G-LM/30-40	35	8.9	5.7	76.3	0.0	0.9	0.3	0.1	0.3	1.2	0.1	554	6.0
G-LM/40-50	45	10.8	6.3	73.6	0.0	0.9	0.3	0.1	0.2	1.2	0.1	541	6.2
G-LM/55-65	60	16.5	7.7	63.4	0.0	0.8	0.5	0.1	0.2	1.1	0.1	473	9.4
G-LM/75-85	80	18.5	8.1	60.2	0.1	0.8	0.6	0.1	0.2	1.0	0.1	423	10.2
G-LM/95-105	100	17.5	8.0	62.5	0.1	0.8	0.6	0.1	0.2	1.0	0.1	452	9.1
G-LM/130-140	135	17.5	7.6	63.8	0.0	0.8	0.6	0.1	0.2	0.9	0.1	426	8.2
G-Bot/0-10	5	9.4	6.2	69.7	0.2	0.5	0.4	0.2	0.1	1.2	0.1	519	11.7

G-Bot/20-30	25	10.6	6.2	73.3	0.1	0.5	0.4	0.1	0.1	1.1	0.1	548	7.1
G-Bot/30-40	35	10.2	6.3	74.2	0.1	0.5	0.4	0.1	0.1	1.2	0.1	562	6.5
G-Bot/40-50	45	11.9	6.5	71.7	0.1	0.5	0.4	0.1	0.1	1.2	0.1	548	7.0
G-Bot/55-65	60	13.9	7.0	68.2	0.1	0.5	0.5	0.1	0.1	1.1	0.1	502	8.1
G-Bot/75-85	80	17.1	7.6	62.9	0.1	0.5	0.5	0.1	0.1	1.1	0.1	446	9.7
G-Bot/95-105	100	18.5	7.9	61.1	0.1	0.5	0.6	0.1	0.1	1.0	0.1	449	9.7
	Depth	**Al_2O_3 %**	**Fe_2O_3 %**	**SiO_2 %**	**CaO %**	**K_2O %**	**MgO %**	**MnO %**	**Na_2O %**	**TiO_2 %**	**P_2O_5 %**	**Zr ppm**	**LOI**
Steep slope													
S-Top/0-10	5	14.9	6.7	61.7	0.1	0.4	0.4	0.1	0.2	1.1	0.2	391	14.1
S-Top/10-20	15	16.0	7.0	62.4	0.1	0.3	0.4	0.0	0.1	1.1	0.1	388	12.3
S-Top/20-30	25	16.7	7.2	62.0	0.1	0.3	0.4	0.0	0.0	1.2	0.1	418	11.8
S-Top/30-40	35	16.9	7.2	62.2	0.0	0.3	0.4	0.0	0.0	1.1	0.1	440	11.4
S-Top/40-50	45	17.0	7.1	62.7	0.1	0.3	0.4	0.0	0.0	1.1	0.1	450	10.9
S-Top/55-65	60	17.1	7.0	63.0	0.0	0.3	0.4	0.0	0.1	1.2	0.1	476	10.7
S-Top/75-85	80	20.2	7.6	58.7	0.0	0.3	0.4	0.0	0.0	1.1	0.1	432	11.3
S-Top/95-105	100	22.1	8.1	56.2	0.0	0.3	0.4	0.0	0.0	1.0	0.1	410	11.4
S-Top/R	135	19.9	6.0	70.6	0.3	5.3	0.4	0.1	1.9	0.8	0.1	429	3.1
S-UM/0-10	5	10.1	6.2	60.4	0.5	1.6	0.4	0.2	0.6	1.0	0.2	339	18.7
S-UM/10-20	15	11.0	6.7	65.7	0.3	1.9	0.3	0.2	0.7	1.0	0.1	380	11.7
S-UM/20-30	25	11.9	7.0	66.0	0.2	2.0	0.4	0.2	0.6	1.1	0.1	408	10.1
S-UM/30-40	35	12.4	7.0	65.9	0.2	2.0	0.4	0.2	0.8	1.1	0.1	405	9.8
S-UM/R	52	12.7	5.6	62.9	0.0	0.1	0.3	0.0		1.0	0.1	491	9.3
S-LM/0-10	5	9.0	6.7	64.8	0.3	1.0	0.3	0.2	0.4	1.2	0.1	426	15.8
S-LM/10-20	15	9.0	7.9	73.4	0.2	1.1	0.3	0.1	0.4	1.5	0.1	491	5.9
S-LM/20-30	25	9.5	8.0	73.6	0.2	1.1	0.3	0.1	0.4	1.5	0.1	515	5.0
S-LM/30-40	35	9.9	7.7	73.2	0.2	1.1	0.3	0.1	0.4	1.4	0.1	514	5.6
S-LM/40-50	45	13.5	8.0	67.3	0.2	1.0	0.4	0.1	0.3	1.3	0.1	496	7.7
S-LM/55-65	60	19.0	8.4	58.3	0.2	0.9	0.5	0.1	0.2	1.1	0.1	416	11.0
S-LM/75-85	80	19.7	8.2	57.4	0.1	0.9	0.6	0.1	0.2	1.1	0.1	408	11.4
S-LM /95-105	100	18.1	8.7	60.0	0.1	0.9	0.5	0.1	0.2	1.2	0.1	424	9.7
S-LM/130-140	135	17.8	8.2	62.6	0.0	0.8	0.5	0.1	0.2	1.1	0.1	440	8.4
S-LM/180-190	185	17.4	7.9	63.5	0.0	0.9	0.5	0.1	0.2	1.1	0.1	427	8.0
S-LM/R	232	14.0	5.4	71.3	0.3	5.8	0.5	0.1	2.0	0.8	0.1	395	2.6
S-Bot/0-10	5	8.0	6.5	72.3	0.2	0.7	0.3	0.2	0.2	1.3	0.1	477	9.9

S-Bot/10-20	15	8.0	6.5	76.0	0.1	0.7	0.3	0.2	0.3	1.4	0.1	540	6.2
S-Bot/20-30	25	7.7	6.6	77.4	0.1	0.8	0.3	0.1	0.2	1.5	0.1	529	5.0
S-Bot/30-40	35	7.9	6.8	77.0	0.1	0.7	0.2	0.1	0.2	1.5	0.1	544	5.0
S-Bot/40-50	45	10.7	7.4	72.1	0.1	0.7	0.3	0.1	0.2	1.4	0.1	534	6.5
S-Bot/55-65	60	15.4	8.3	64.3	0.2	0.7	0.5	0.1	0.2	1.2	0.1	478	8.9
S-Bot/75-85	80	16.5	8.9	62.4	0.1	0.7	0.5	0.1	0.2	1.3	0.1	460	8.9
S-Bot/95-105	100	17.5	8.3	61.9	0.1	0.7	0.6	0.1	0.2	1.1	0.1	438	9.1
S-Bot/130-140	135	16.9	10.8	61.2	0.2	0.5	0.5	0.1	0.1	1.5	0.1	442	7.9
S-Bot/180-190	185	16.7	10.3	61.8	0.1	0.6	0.5	0.1	0.1	1.5	0.1	441	7.9
S-Bot/R	216	11.7	6.4	69.2	0.1	1.8	0.9	0.0	0.7	0.9	0.1	471	5.9

Bedrock samples	**Depth**	**Al_2O_3 %**	**Fe_2O_3 %**	**SiO_2 %**	**CaO %**	**K_2O %**	**MgO %**	**MnO %**	**Na_2O %**	**TiO_2 %**	**P_2O_5 %**	**Zr ppm**	**LOI**
Average sample		12.4	5.3	71.1	0.7	4.4	0.6	0.1	2.1	0.7	0.1	364	2.5
ILOPOLIS GAZ STATION	Outcrop	12.2	5.3	70.4	1.0	3.5	0.8	0.1	2.2	0.6	0.2	338	2.7
ILOPOLIS GAZ STATION 2	Outcrop2	12.2	6.0	71.6	0.2	5.4	0.3	0.0	2.0	0.8	0.1	434	2.8
ARVOREZINHA	River boulder	12.9	4.6	71.3	0.8	4.3	0.7	0.1	2.0	0.6	0.2	321	2.1

Table SI 3.2: Fractional mass gain ($\tau_{j,w} > 0$) or loss ($\tau_{j,w} < 0$) relative to the composition of the parent material and referred to Ti

Sample ID	Depth	τ_{Al}	τ_{Fe}	τ_{Si}	τ_{Ca}	τ_{K}	τ_{Mg}	τ_{Mn}	τ_{Na}	τ_{P}	τ_{Zr}
Gentle slope data											
G-Top/0-10	5	-0.50	-0.31	-0.50	-0.82	-0.91	-0.69	-0.49	-0.95	-0.70	-0.35
G-Top/10-20	15	-0.44	-0.30	-0.38	-0.90	-0.90	-0.68	-0.62	-0.95	-0.71	-0.21
G-Top /20-30	25	-0.43	-0.29	-0.39	-0.92	-0.91	-0.70	-0.65	-0.96	-0.74	-0.19
G-Top /30-40	35	-0.37	-0.27	-0.40	-0.94	-0.91	-0.68	-0.65	-0.96	-0.72	-0.23
G-Top /40-50	45	-0.37	-0.28	-0.43	-0.95	-0.92	-0.70	-0.69	-0.96	-0.76	-0.21
G-Top /55-65	60	-0.13	-0.12	-0.43	-0.95	-0.91	-0.58	-0.64	-0.96	-0.68	-0.19
G-Top /75-85	80	0.22	0.03	-0.39	-0.94	-0.87	-0.40	-0.59	-0.94	-0.64	-0.17
G-Top/Sap	100	-0.14	-0.08	-0.38	-0.71	-0.18	-0.26	-0.43	-0.49	-0.80	-0.10
G-UM/0-10	5	-0.53	-0.30	-0.45	-0.83	-0.87	-0.77	-0.46	-0.94	-0.58	-0.27
G-UM/10-20	15	-0.57	-0.29	-0.48	-0.95	-0.88	-0.82	-0.53	-0.94	-0.71	-0.24
G-UM/20-30	25	-0.55	-0.28	-0.49	-0.96	-0.88	-0.81	-0.54	-0.94	-0.71	-0.29
G-UM/30-40	35	-0.45	-0.24	-0.50	-0.95	-0.88	-0.78	-0.58	-0.95	-0.69	-0.28
G-UM/40-50	45	-0.23	-0.05	-0.52	-0.95	-0.89	-0.71	-0.56	-0.95	-0.63	-0.30
G-UM/55-65	60	-0.05	0.01	-0.51	-0.94	-0.89	-0.63	-0.48	-0.96	-0.64	-0.30
G-UM/75-85	80	-0.11	-0.04	-0.51	-0.95	-0.91	-0.66	-0.64	-0.97	-0.72	-0.29
G-UM/95-105	100	-0.23	-0.14	-0.55	-0.97	-0.92	-0.70	-0.70	-0.97	-0.78	-0.35
G-UM/130-140	135	-0.21	-0.14	-0.52	-0.97	-0.90	-0.69	-0.65	-0.96	-0.80	-0.32
G-UM/Sap	185	-0.28	-0.12	-0.52	-0.94	-0.84	-0.66	-0.30	-0.90	-0.75	-0.33
G-LM/0-10	5	-0.50	-0.37	-0.39	-0.68	-0.85	-0.74	-0.26	-0.93	-0.56	-0.18
G-LM/10-20	15	-0.62	-0.43	-0.43	-0.96	-0.86	-0.82	-0.41	-0.94	-0.71	-0.17
G-LM/20-30	25	-0.63	-0.43	-0.44	-0.96	-0.86	-0.83	-0.38	-0.94	-0.72	-0.18
G-LM/30-40	35	-0.61	-0.43	-0.42	-0.98	-0.86	-0.82	-0.36	-0.93	-0.71	-0.12
G-LM/40-50	45	-0.52	-0.36	-0.43	-0.98	-0.86	-0.79	-0.47	-0.94	-0.71	-0.13
G-LM/55-65	60	-0.18	-0.13	-0.46	-0.97	-0.86	-0.64	-0.59	-0.95	-0.62	-0.16
G-LM/75-85	80	-0.06	-0.06	-0.47	-0.96	-0.86	-0.60	-0.61	-0.95	-0.64	-0.23
G-LM/95-105	100	-0.11	-0.06	-0.45	-0.96	-0.87	-0.58	-0.58	-0.95	-0.69	-0.17
G-LM/130-140	135	0.06	0.06	-0.33	-0.97	-0.83	-0.51	-0.44	-0.93	-0.66	-0.07
G-Bot/0-10	5	-0.58	-0.37	-0.47	-0.86	-0.92	-0.76	-0.10	-0.97	-0.61	-0.17
G-Bot/20-30	25	-0.52	-0.35	-0.42	-0.92	-0.92	-0.74	-0.42	-0.97	-0.70	-0.10
G-Bot/30-40	35	-0.55	-0.37	-0.44	-0.95	-0.92	-0.77	-0.39	-0.97	-0.70	-0.12

G-Bot/40-50	45	-0.47	-0.34	-0.45	-0.94	-0.92	-0.74	-0.42	-0.97	-0.70	-0.13
G-Bot/55-65	60	-0.37	-0.27	-0.46	-0.93	-0.92	-0.70	-0.47	-0.97	-0.66	-0.17
G-Bot/75-85	80	-0.16	-0.13	-0.46	-0.93	-0.91	-0.63	-0.59	-0.98	-0.65	-0.20
G-Bot/95-105	100	-0.05	-0.07	-0.46	-0.93	-0.91	-0.59	-0.57	-0.98	-0.67	-0.17
	135	-0.09	-0.10	-0.43	-0.94	-0.91	-0.58	-0.55	-0.98	-0.68	-0.15
Steep slope	**Depth**	τ_{Al}	τ_{Fe}	τ_{Si}	τ_{Ca}	τ_{K}	τ_{Mg}	τ_{Mn}	τ_{Na}	τ_{P}	τ_{Zr}
S-Top/0-10	5	-0.26	-0.24	-0.47	-0.94	-0.93	-0.72	-0.54	-0.95	-0.47	-0.30
S-Top/10-20	15	-0.23	-0.22	-0.48	-0.95	-0.94	-0.75	-0.78	-0.99	-0.59	-0.33
S-Top/20-30	25	-0.26	-0.27	-0.53	-0.97	-0.95	-0.78	-0.82	-0.99	-0.64	-0.34
S-Top/30-40	35	-0.20	-0.22	-0.49	-0.97	-0.95	-0.75	-0.79	-0.99	-0.62	-0.25
S-Top/40-50	45	-0.21	-0.24	-0.49	-0.97	-0.95	-0.76	-0.79	-0.99	-0.64	-0.24
S-Top/55-65	60	-0.22	-0.27	-0.50	-0.98	-0.95	-0.76	-0.80	-0.99	-0.66	-0.22
S-Top/75-85	80	-0.03	-0.17	-0.51	-0.98	-0.94	-0.71	-0.81	-0.99	-0.69	-0.25
S-Top/95-105	100	0.12	-0.06	-0.51	-0.98	-0.94	-0.70	-0.83	-0.99	-0.68	-0.26
S-Top/Sap	135	0.34	-0.06	-0.17	-0.74	0.25	-0.64	-0.43	-0.30	-0.58	0.05
S-UM/0-10	5	-0.47	-0.25	-0.45	-0.69	-0.70	-0.73	0.45	-0.81	-0.39	-0.35
S-UM/10-20	15	-0.44	-0.23	-0.43	-0.82	-0.66	-0.75	0.18	-0.79	-0.52	-0.31
S-UM/20-30	25	-0.43	-0.23	-0.45	-0.87	-0.67	-0.75	0.07	-0.84	-0.60	-0.30
S-UM/30-40	35	-0.39	-0.21	-0.44	-0.88	-0.66	-0.73	-0.16	-0.80	-0.61	-0.28
S-UM/Sap	52	-0.30	-0.29	-0.40	-0.98	-0.99	-0.74	-0.84	-	-0.54	-0.03
S-LM/0-10	5	-0.62	-0.34	-0.52	-0.81	-0.86	-0.82	-0.04	-0.92	-0.60	-0.34
S-LM/10-20	15	-0.68	-0.35	-0.54	-0.93	-0.87	-0.86	-0.48	-0.92	-0.79	-0.37
S-LM/20-30	25	-0.67	-0.36	-0.55	-0.93	-0.87	-0.86	-0.56	-0.93	-0.83	-0.35
S-LM/30-40	35	-0.63	-0.33	-0.52	-0.93	-0.86	-0.85	-0.59	-0.93	-0.80	-0.30
S-LM/40-50	45	-0.46	-0.27	-0.53	-0.90	-0.86	-0.79	-0.61	-0.93	-0.75	-0.28
S-LM/55-65	60	-0.09	-0.07	-0.51	-0.89	-0.85	-0.66	-0.56	-0.94	-0.63	-0.28
S-LM/75-85	80	-0.03	-0.07	-0.51	-0.93	-0.85	-0.61	-0.58	-0.94	-0.65	-0.28
S-LM /95-105	100	-0.22	-0.14	-0.55	-0.96	-0.86	-0.66	-0.55	-0.95	-0.77	-0.34
S-LM/130-140	135	-0.19	-0.15	-0.50	-0.97	-0.87	-0.69	-0.55	-0.95	-0.79	-0.28
S-LM/180-190	185	-0.17	-0.14	-0.48	-0.97	-0.85	-0.69	-0.53	-0.94	-0.78	-0.27
S-LM/Sap	232	-0.03	-0.15	-0.15	-0.70	0.39	-0.46	-0.17	-0.26	-0.47	-0.02
S-Bot/0-10	5	-0.69	-0.42	-0.51	-0.90	-0.90	-0.84	-0.07	-0.95	-0.67	-0.32
S-Bot/10-20	15	-0.70	-0.43	-0.50	-0.94	-0.90	-0.86	-0.31	-0.95	-0.72	-0.26
S-Bot/20-30	25	-0.73	-0.46	-0.53	-0.96	-0.91	-0.87	-0.46	-0.95	-0.80	-0.33

S-Bot/30-40	35	-0.72	-0.44	-0.53	-0.96	-0.91	-0.87	-0.48	-0.95	-0.80	-0.30
S-Bot/40-50	45	-0.60	-0.36	-0.53	-0.94	-0.91	-0.83	-0.58	-0.96	-0.78	-0.28
S-Bot/55-65	60	-0.34	-0.19	-0.53	-0.92	-0.89	-0.72	-0.65	-0.96	-0.70	-0.26
S-Bot/75-85	80	-0.33	-0.17	-0.56	-0.92	-0.90	-0.70	-0.65	-0.96	-0.74	-0.32
S-Bot/95-105	100	-0.20	-0.12	-0.51	-0.92	-0.89	-0.63	-0.64	-0.96	-0.73	-0.28
S-Bot/130-140	135	-0.40	-0.12	-0.62	-0.93	-0.93	-0.73	-0.59	-0.98	-0.79	-0.43
S-Bot/180-190	185	-0.40	-0.16	-0.62	-0.94	-0.92	-0.74	-0.65	-0.97	-0.79	-0.43
S-Bot/Sap	216	-0.31	-0.14	-0.29	-0.89	-0.63	-0.27	-0.77	-0.78	-0.47	0.00

Table SI 3.3: Chemical Depletion Fraction ($CDF_{(z)}$) of the saprolite samples (not corrected for Strain).

Sample ID	$CDF_{(z)}$
Gentle slope data	
G-Top/Sap	0.31
G-UM/Sap	0.48
Steep slope data	
S-Top/Sap	0.10
S-UM/Sap	0.39
S-LM/Sap	0.20
S-Bot/Sap	0.30

CHAPTER IV

Table SI 4.1: Chemical characterization of the samples. Major elements are given in oxide wt. % trace elements in ppm and Chemical Depletion Fraction in %.

Sample Code	LOI (%)	Depth (cm)	Si	Al	Fe	K	Mg	Na	Ca	Ti	P
			Measured at UCL (in wt. %)								
EST-C-U1	5.9	4	33.5	6.62	3.06	1.54	0.79	0.55	0.53	0.45	0.02
EST-C-U2	5.5	13	33.02	7.27	3.7	1.64	0.81	0.32	0.47	0.46	0.02
EST-C-U3	6.3	20	28.51	9.63	5.39	2.47	1.02	0.33	0.61	0.5	0.02
EST-C-U4	5.5	28	28.32	10.19	5.15	2.89	0.92	0.42	0.58	0.54	0.02
EST-C-U5	4.7	39.5	30.48	10.05	4.73	2.92	0.79	0.47	0.54	0.54	0.02
EST-C-U6	4.9	49.5	29.33	9.61	5.08	2.75	0.89	0.41	0.56	0.51	0.01
EST-C-rock	3.3	82.5	25.77	13.25	5.19	3.9	0.22	1.05	0.67	0.65	0.07
FIL2-A-U1	6.6	3	31.03	7.49	4.26	1.84	0.51	0.65	0.36	0.9	0.04
FIL2-A-U2	6.1	8	30.42	8.33	4.4	2.01	0.48	0.7	0.36	0.93	0.03
FIL2-A-U3	5.5	11	30.06	8.74	4.37	2.17	0.49	0.75	0.4	0.92	0.03
FIL2-A-U4	6	16	29.54	9.18	4.47	2.22	0.51	0.76	0.38	0.88	0.04
FIL2-A-U5	6.8	24	28.81	9.83	4.41	2.43	0.53	0.81	0.41	0.73	0.04
FIL2-A- rock	3.4	43	29.08	10.32	4.76	2.56	0.68	0.94	0.1	0.61	0.05
CAB-B-U1	6.9	5	24.58	12.19	5.98	2.72	1.02	0.66	0.76	0.77	0.08
CAB-B-U2	7.7	8	25.44	11.28	5.46	2.53	1.01	0.59	1.41	0.7	0.07
CAB-B-U3	8	10.5	24.74	11.07	5.59	2.45	1.03	0.57	2.12	0.65	0.08
CAB-B-U4	8.2	17	24.94	10.88	5.03	2.37	1.01	0.61	2.28	0.57	0.08
CAB-B-Rock	4.9	40	25.12	12.29	6.21	3.17	0.98	0.8	0.37	0.66	0.09
BHVO-2[1]	/	/	22.86	6.83	8.28	0.43	4.17	1.64	7.91	1.57	0.10
WS-E[1]	/	/	/	/	/	/	/	/	/	/	/
BLANK	/	/	0.03	0.005	0.002	0.007	0.005	<0.001	0.01	<0.001	<0.001

[1] BHVO-2 corresponds to Basalt, Hawaiian Volcanic Observatory [*Wilson*, 1997] and WS-E to Great Whin Sill, Northern England [*Govindaraju et al.*, 1994]

Table SI 4.1: continued…

Sample Code	Zr	CDF (Zr)	Cd	Sb	Pb	As	Nb	Hf
	(in mg/kg)	*% of denudation attributed to chemical weathering*	*Measured at LHyGeS (in mg/kg)*					
EST-C-U1	325	0.29	0.06	2	28.6	12.8	13.8	8.2
EST-C-U2	289	0.20	0.08	3	22.6	28.8	14.5	8.2
EST-C-U3	270	0.14	0.09	3	16.8	28.4	15.2	6.9
EST-C-U4	285	0.19	0.09	3	17	14.4	15.4	7
EST-C-U5	283	0.18	0.06	6	16.2	13.5	17	7
EST-C-U6	269	0.14	0.08	6	15.5	13.4	15.6	6.9
EST-C-rock	232	0	0.12	3	19.8	3.2	18.9	6.5
FIL2-A-U1	374	0.28	0.17	4	51	13.6	24.6	10.1
FIL2-A-U2	350	0.23	0.12	4	41.2	13.8	23.9	9.7
FIL2-A-U3	386	0.3	0.12	4	35.7	13	25	10.2
FIL2-A-U4	338	0.2	0.09	4	32.9	14.5	22.3	8.5
FIL2-A-U5	339	0.2	0.08	4	32.6	10.5	20	6.9
FIL2-A- rock	270	0	0.07	2	16.9	13.3	14	7.6
CAB-B-U1	265	0.15	2.13	24	469	34	21.9	7.4
CAB-B-U2	212	-0.06	2.35	22	312	27.5	18.2	6.4
CAB-B-U3	206	-0.09	3.22	53	381	34.1	18.4	6.3
CAB-B-U4	231	0.03	2.93	38	317	30	19.3	7
CAB-B- Rock	225	0	0.38	6	73.2	6	17.4	5
BHVO-2[1]	171	/	/	/	/	/	/	/
WS-E[1]	/	/	0.29	0.2	15.2	0.8	16.7	5.29
BLANK	<0.001		<0.001	<0.001	<0.001	<0.001	<0.001	<0.001

Table SI 3.2: Mass transfer coefficient (Tau) of the samples for major elements and U, Th (referred to Zr)

Sample Code	Depth (cm)	τ - Si	τ - Al	τ - Fe	τ - K	τ - Mg	τ - Na	τ - Ca	τ - Ti	τ - P	τ - U	τ - Th
EST-C-U1	4.0	-0.07	-0.64	-0.58	-0.72	1.57	-0.63	-0.43	-0.51	-0.79	-0.43	-0.58
EST-C-U2	13.0	0.03	-0.56	-0.43	-0.66	1.95	-0.76	-0.44	-0.43	-0.82	-0.27	-0.41
EST-C-U3	20.0	-0.05	-0.38	-0.11	-0.46	2.98	-0.73	-0.22	-0.34	-0.77	-0.28	-0.13
EST-C-U4	28.0	-0.11	-0.37	-0.19	-0.40	2.40	-0.67	-0.30	-0.32	-0.76	-0.24	-0.15
EST-C-U5	39.5	-0.03	-0.38	-0.25	-0.39	1.95	-0.63	-0.34	-0.32	-0.80	-	-
EST-C-U6	49.5	-0.02	-0.37	-0.15	-0.39	2.49	-0.66	-0.28	-0.32	-0.81	-0.31	-0.21
EST-C-rock	82.5	-	-	-	-	-	-	-	-	-	-	-

FIL2-A-U1	3.0	-0.23	-0.48	-0.35	-0.48	-0.46	-0.50	1.59	0.06	-0.36	-0.21	-0.27
FIL2-A-U2	8.0	-0.20	-0.38	-0.29	-0.40	-0.46	-0.43	1.77	0.17	-0.42	0.12	-0.08
FIL2-A-U3	11.0	-0.28	-0.41	-0.36	-0.41	-0.50	-0.44	1.79	0.05	-0.49	-0.05	-0.21
FIL2-A-U4	16.0	-0.19	-0.29	-0.25	-0.31	-0.40	-0.36	2.03	0.15	-0.39	0.05	0.01
FIL2-A-U5	24.0	-0.21	-0.24	-0.26	-0.25	-0.38	-0.31	2.26	-0.05	-0.36	0.05	0.07
FIL2-A- rock	43.0	-	-	-	-	-	-	-	-	-	-	
CAB-B-U1	5.0	-0.17	-0.16	-0.18	-0.27	-0.12	-0.30	0.74	-0.01	-0.25	1.30	0.25
CAB-B-U2	8.0	0.07	-0.03	-0.07	-0.15	0.09	-0.22	3.04	0.12	-0.13	1.65	0.39
CAB-B-U3	10.5	0.07	-0.02	-0.02	-0.16	0.15	-0.22	5.25	0.07	-0.06	2.66	0.34
CAB-B-U4	17.0	-0.03	-0.14	-0.21	-0.27	0.00	-0.26	4.99	-0.16	-0.13	1.73	0.22
CAB-B- Rock	40.0	-0.07	-	-	-	-	-	-	-	-	-	-

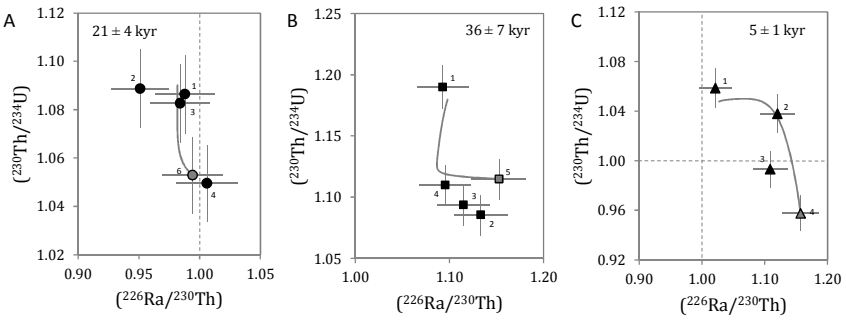

Figure. SI 4.1 : Measured ($^{230}Th/^{234}U$) and ($^{226}Ra/^{230}Th$) activity ratios for the three regolith profiles in the Betic Cordillera: (A) Sierra de las Estancias, (B) Sierra de los Filabres, (C) Sierra Cabrera (samples taken just above soil-bedrock boundary are in dark grey). The numbers refer to sample codes. Grey lines represent the evolution of the activity ratios in the soil profile as simulated with the soil U-series fractionation model using the deepest soil sample as reference (Eq. 1). Where relevant, soil residence time is mentioned in the graph.

References

Aciego, S. M., S. M. Aarons, and K. W. W. Sims (2015), The uranium-isotopic composition of Saharan dust collected over the central Atlantic Ocean, *Aeolian Research*, *17*, 61-66.

Ackerer, J., F. Chabaux, J. Van der Woerd, D. Viville, E. Pelt, E. Kali, C. Lerouge, P. Ackerer, R. di Chiara Roupert, and P. Négrel (2016), Regolith evolution on the millennial timescale from combined U–Th–Ra isotopes and in situ cosmogenic 10Be analysis in a weathering profile (Strengbach catchment, France), *Earth and Planetary Science Letters*, *453*, 33-43.

Ahnert, F. (1977), Some comments on the quantitative formulation of geomorphological processes in a theoretical model, *Earth Surface Processes*, *2*(2 - 3), 191-201.

Aldahan, A., Y. Haiping, and G. Possnert (1999), Distribution of beryllium between solution and minerals (biotite and albite) under atmospheric conditions and variable pH, *Chemical geology*, *156*(1), 209-229.

Alvares, C. A., J. L. Stape, P. C. Sentelhas, G. de Moraes, J. Leonardo, and G. Sparovek (2013), Köppen's climate classification map for Brazil, *Meteorologische Zeitschrift*, *22*(6), 711-728.

Ameijeiras-Mariño, Y., S. Opfergelt, J. Schoonejans, V. Vanacker, P. Sonnet, and P. Delmelle (2015), Tectonic uplift and denudation rate influence soil chemical weathering intensity in a semi-arid environment, southeast Spain: physico-chemical and mineralogical evidence, paper presented at EGU General Assembly 2015, Copernicus, Vienna.

Amundson, R. (2007), Coupling between Biota and Earth Materials in the Critical Zone, *Elements*, *3*(327-332).

Anderson, R. S. (2007), Physical and Chemical controls on the Critical Zone, *Elements*, *3*, 315-319.

Anderson, R. S. (2015), Particle trajectories on hillslopes: Implications for particle age and ^{10}Be structure, *Journal of Geophysical Research: Earth Surface*, *120*(9), 1626-1644.

Anderson, R. S., G. Jiménez-Moreno, J. S. Carrión, and C. Pérez-Martínez (2011), Postglacial history of alpine vegetation, fire, and climate from Laguna de Río Seco, Sierra Nevada, southern Spain, *Quaternary Science Reviews*, *30*(13-14), 1615-1629.

Anderson, R. S., S. Anderson, A. K. Aufdenkampe, R. Bales, S. Brantley, J. Chorover, C. J. Duffy, F. Scatena, D. L. Sparks, and P. A. Troch (2010), Future directions for critical zone observatory (CZO) science, *CZO Community*, *29*.

Anderson, S. P., W. E. Dietrich, and G. H. Brimhall (2002), Weathering profiles, mass-balance analysis, and rates of solute loss: Linkages between weathering and erosion in a small, steep catchment., *Geological Society of America Bulletin*, 1143-1148.

Anderson, S. P., F. von Blanckenburg, and A. F. White (2007), Physical and chemical controls on the critical zone, *Elements*, *3*(5), 315-319.

Asio, V. B., and R. Jahn (2007), Weathering of basaltic rock and clay mineral formation in Leyte, Philippines, *Philippine Agricultural Scientist (Philippines)*.

Atlas Nacional de España (1993), Mapa Minero, Instituto Tecnológico GeoMinero de España, Madrid.

Attal, M., S. M. Mudd, M. D. Hurst, B. Weinman, K. Yoo, and M. Naylor (2015), Impact of change in erosion rate and landscape steepness on hillslope and fluvial sediments grain size in the Feather River basin (Sierra Nevada, California), *Earth Surf. Dynam.*, *3*(1), 201-222.

Avila, A., M. Alarcón, and I. Queralt (1998), The chemical composition of dust transported in red rains—its contribution to the biogeochemical cycle of a holm oak forest in Catalonia (Spain), *Atmospheric Environment*, *32*(2), 179-191.

Bacon, A. R., P. R. Bierman, and D. H. Rood (2012), Coupling meteoric ^{10}Be with pedogenic losses of ^{9}Be to improve soil residence time estimates on an ancient North American interfluve, *Geology*, *40*(9), 847-850.

Balco, G. (2004), The sedimentary record of subglacial erosion beneath the Laurentide Ice Sheet, 137 pp, University of Washington.

Balco, G., J. O. Stone, N. A. Lifton, and T. J. Dunai (2008), A complete and easily accessible means of calculating surface exposure ages or erosion rates from ^{10}Be and ^{26}Al measurements, *Quaternary Geochronology*, *3*(3), 174-195.

Banner, J. L. (2004), Radiogenic isotopes: systematics and applications to earth surface processes and chemical stratigraphy, *Earth-Science Reviews*, *65*(3–4), 141-194.

Barg, E., D. Lal, M. Pavich, M. Caffee, and J. Southon (1997), Beryllium geochemistry in soils: evaluation of ^{10}Be/^{9}Be ratios in authigenic minerals as a basis for age models, *Chemical Geology*, *140*(3), 237-258.

Bauer, A., and B. D. Velde (2014), *Geochemistry at the Earth's Surface*, 1 ed., XIII, 315 pp., Springer-Verlag Berlin Heidelberg.

Behrmann, J. H. (1983), Microstructure and fabric transitions in calcite tectonites from the Sierra Alhamilla (Spain), *Geologische Rundschau*, *72*(2), 605-618.

Bellieni, G., P. Comin-Chiaramonti, L. Marques, A. Melfi, A. Nardy, C. Papatrechas, E. Piccirillo, A. Roisenberg, and D. Stolfa (1986), Petrogenetic aspects of acid and basaltic lavas from the Paraná plateau (Brazil): geological, mineralogical and petrochemical relationships, *Journal of Petrology*, *27*(4), 915-944.

Bellin, N., V. Vanacker, and S. De Baets (2013), Anthropogenic and climatic impact on Holocene sediment dynamics in SE Spain: A review, *Quaternary International*, *308-309*, 112-129.

Bellin, N., V. Vanacker, and P. W. Kubik (2014), Denudation rates and tectonic geomorphology of the Spanish Betic Cordillera, *Earth and Planetary Science Letters*, *390*, 19-30.

Berner, R. A., A. C. Lasaga, and R. M. Garrels (1983), The carbonate-silicat geochemical cycle and its effect on atmospheric carbon dioxide over the past 100 million years, *American Journal of Science*, *283*, 641-683.

Bhatt, M. P., and W. H. McDowell (2007), Controls on major solutes within the drainage network of a rapidly weathering tropical watershed, *Water Resources Research*, *43*(11), n/a-n/a.

Bourles, D., G. M. Raisbeck, and F. Yiou (1989), ^{10}Be and ^{9}Be in marine sediments and their potential for dating, *Geochimica et Cosmochimica Acta*, *53*(2), 443-452.

Brady, N. C., and R. R. Weil (1996), *The nature and properties of soils*, Prentice-Hall Inc.

Braga, J. C., J. M. Martín, and C. Quesada (2003), Patterns and average rates of late Neogene – Recent uplift of the Betic Cordillera, SE Spain, *Geomorphology*, *50*, 3-26.

Brantley, S., T. White, A. White, D. Sparks, D. Richter, K. Pregitzer, L. Derry, J. Chorover, O. Chadwick, and R. April (2006), Frontiers in Exploration of the Critical Zone: Report of a workshop sponsored by the National Science Foundation (NSF), *Newark, DE*, 30.

Brantley, S. L. (2006), Frontiers in Exploration of the Critical Zone: Report of a workshop sponsored by the National Sciences Foundation (NSF), 30.

Brantley, S. L., and M. Lebedeva (2011), Learning to Read the Chemistry of Regolith to Understand the Critical Zone, *Annual Review of Earth and Planetary Sciences*, *39*(1), 387-416.

Brantley, S. L., M. B. Goldhaber, and V. K. Ragnarsdottir (2007), Crossing Disciplines and Scales to Understand the Critical Zone, *Elements*, *3*, 307-314.

Brantley, S. L., J. Bandstra, J. Moore, and A. F. White (2008), Modelling chemical depletion profiles in regolith, *Geoderma*, *145*(3–4), 494-504.

Brantley, S. L., et al. (2011), Twelve testable hypotheses on the geobiology of

weathering, *Geobiology*, *9*(2), 140-165.

Braucher, R., D. L. Bourlès, F. Colin, E. T. Brown, and B. Boulangé (1998a), Brazilian laterite dynamics using in situ-produced ^{10}Be, *Earth and Planetary Science Letters*, *163*(1-4), 197-205.

Braucher, R., F. Colin, E. T. Brown, D. L. Bourlès, O. Bamba, G. M. Raisbeck, F. Yiou, and J. M. Koud (1998b), African laterite dynamics using in situ-produced ^{10}Be, *Geochimica et Cosmochimica Acta*, *62*(9), 1501-1507.

Brimhall, G. H., and W. E. Dietrich (1987), Constitutive mass balance relations between chemical composition, volume, density, porosity, and strain in metasomatic hydrochemical systems: Results on weathering and pedogenesis, *Geochimica et Cosmochimica Acta*, *51*(3), 567-587.

Brimhall, G. H., O. A. Chadwick, C. J. Lewis, W. Compston, I. S. Williams, K. J. Danti, W. E. Dietrich, M. E. Power, D. Hendricks, and J. Bratt (1992), Deformational Mass Transport and Invasive Processes in Soil Evolution, *Science*, *255*(5045), 695-702.

Brown, L., M. J. Pavich, R. Hickman, J. Klein, and R. Middleton (1988), Erosion of the eastern United States observed with ^{10}Be, *Earth Surface Processes and Landforms*, *13*(5), 441-457.

Burke, B. C., A. M. Heimsath, and A. F. White (2007), Coupling chemical weathering with soil production across soil-mantled landscapes, *Earth Surface Processes and Landforms*, *32*(6), 853-873.

Buss, H. L., M. A. Bruns, M. J. Schultz, J. Moore, C. F. Mathur, and S. L. Brantley (2005), The coupling of biological iron cycling and mineral weathering during saprolite formation, Luquillo Mountains, Puerto Rico, *Geobiology*, *3*(4), 247-260.

Campforts, B., V. Vanacker, J. Vanderborght, S. Baken, E. Smolders, and G. Govers (2016), Simulating the mobility of meteoric ^{10}Be in the landscape through a coupled soil-hillslope model (Be2D), *Earth and Planetary Science Letters*, *439*, 143-157.

Caner, L., L. M. Radtke, M. L. Vignol-Lelarge, A. V. Inda, E. C. Bortoluzzi, and A. S. Mexias (2014), Basalt and rhyo-dacite weathering and soil clay formation under subtropical climate in southern Brazil, *Geoderma*, *235*, 100-112.

Carrión, J. S., S. Fernández, G. Jiménez-Moreno, S. Fauquette, G. Gil-Romera, P. González-Sampériz, and C. Finlayson (2010), The historical origins of aridity and vegetation degradation in southeastern Spain, *Journal of Arid Environments*, *74*(7), 731-736.

Castillo, S., T. Moreno, X. Querol, A. Alastuey, E. Cuevas, L. Herrmann, M. Mounkaila, and W. Gibbons (2008), Trace element variation in size-fractionated African

desert dusts, *Journal of Arid Environments*, *72*(6), 1034-1045.

Castro, P., S. Gili, V. Lull, R. Mico, C. Rihuete, R. Risch, M. E. S. Yll, and R. Chapman (2000), Archaeology and Desertification in the Vera Basin (Almeria, South-East Spain), *European Journal of Archaeology*, *3*(2), 147-166.

Cerdan, O., et al. (2010), Rates and spatial variations of soil erosion in Europe: A study based on erosion plot data, *Geomorphology*, *122*(1-2), 167-177.

Chabaux, F., D. B. Othman, and J. L. Birck (1994), A new RaBa chromatographic separation and its application to Ra mass-spectrometric measurement in volcanic rocks, *Chemical Geology*, *114*(3-4), 191-197.

Chabaux, F., J. Riotte, and O. Dequincey (2003a), U-Th-Ra Fractionation During Weathering and River Transport *Reviews in Mineralogy and Geochemistry*, *52*, 533-576.

Chabaux, F., B. Bourdon, and J. Riotte (2008), Chapter 3 U-Series Geochemistry in Weathering Profiles, River Waters and Lakes, *13*, 49-104.

Chabaux, F., J. Riotte, N. Clauer, and C. France-Lanord (2001), Isotopic tracing of the dissolved U fluxes of Himalayan rivers: Implications for present and past U budgets of the Ganges-Brahmaputra system, *Geochimica et Cosmochimica Acta*, *65*(19), 3201-3217.

Chabaux, F., E. Blaes, M. Granet, R. Roupert, and P. Stille (2012), Determination of transfer time for sediments in alluvial plains using ^{238}U-^{234}U-^{230}Th disequilibria: The case of the Ganges river system, *Comptes Rendus Geoscience*, *344*(11–12), 688-703.

Chabaux, F., O. Dequincey, J.-J. Lévèque, J.-C. Leprun, N. Clauer, J. Riotte, and H. Paquet (2003b), Tracing and dating recent chemical transfers in weathering profiles by trace-element geochemistry and ^{238}U · ^{234}U · ^{230}Th disequilibria: the example of the Kaya lateritic toposequence (Burkina-Faso), *Comptes Rendus Geoscience*, *335*(16), 1219-1231.

Chabaux, F., J. Riotte, A. D. Schmitt, J. Carignan, P. Herckes, M. C. Pierret, and H. Wortham (2005), Variations of U and Sr isotope ratios in Alsace and Luxembourg rain waters: Origin and hydrogeochemical implications, *Comptes Rendus - Geoscience*, *337*(16), 1447-1456.

Chabaux, F., L. Ma, P. Stille, E. Pelt, M. Granet, D. Lemarchand, R. Roupert, and S. L. Brantley (2011), Determination of chemical weathering rates from U series nuclides in soils and weathering profiles: Principles, applications and limitations, *Applied Geochemistry*, *26*, S20-S23.

Chabaux, F., E. Blaes, P. Stille, R. di Chiara Roupert, E. Pelt, A. Dosseto, L. Ma, H. L. Buss, and S. L. Brantley (2013), Regolith formation rate from U-series nuclides: Implications from the study of a spheroidal weathering profile in the Rio Icacos

watershed (Puerto Rico), *Geochimica et Cosmochimica Acta*, *100*, 73-95.

Chadwick, O. A., and J. Chorover (2001), The chemistry of pedogenic thresholds, *Geoderma*, *100*(3–4), 321-353.

Chadwick, O. A., G. H. Brimhall, and D. M. Hendricks (1990), From a black to a gray box — a mass balance interpretation of pedogenesis, *Geomorphology*, *3*(3–4), 369-390.

Chadwick, O. A., L. A. Derry, P. M. Vitousek, B. J. Huebert, and L. O. Hedin (1999), Changing sources of nutrients during four million years of ecosystem development, *Nature*, *397*(6719), 491-497.

Chao, T. T., and R. F. Sanzolone (1992), Decomposition techniques, *Journal of Geochemical Exploration*, *44*(1-3), 65-106.

Chmeleff, J., F. von Blanckenburg, K. Kossert, and D. Jakob (2010), Determination of the ^{10}Be half-life by multicollector ICP-MS and liquid scintillation counting, *Nuclear Instruments and Methods in Physics Research Section B: Beam Interactions with Materials and Atoms*, *268*(2), 192-199.

Cohen, S., G. Willgoose, and G. Hancock (2009), The mARM spatially distributed soil evolution model: A computationally efficient modeling framework and analysis of hillslope soil surface organization, *Journal of Geophysical Research: Earth Surface*, *114*(F3), n/a-n/a.

Crews, T. E., K. Kitayama, J. H. Fownes, R. H. Riley, D. A. Herbert, D. Mueller-Dombois, and P. M. Vitousek (1995), Changes in Soil Phosphorus Fractions and Ecosystem Dynamics across a Long Chronosequence in Hawaii, *Ecology*, *76*(5), 1407-1424.

Crutzen, P. J. (2002), Geology of mankind, *Nature*, *415*(6867), 23-23.

Cyr, A. J., and D. E. Granger (2008), Dynamic equilibrium among erosion, river incision, and coastal uplift in the northern and central Apennines, Italy, *Geology*, *36*(2), 103-106.

Cyr, A. J., D. E. Granger, V. Olivetti, and P. Molin (2010), Quantifying rock uplift rates using channel steepness and cosmogenic nuclide–determined erosion rates: Examples from northern and southern Italy, *Lithosphere*, *2*(3), 188-198.

De Luís, M., J. Raventós, J. C. González-Hidalgo, J. R. Sánchez, and J. Cortina (2000), Spatial analysis of rainfall trends in the region of Valencia (east Spain), *International Journal of Climatology*, *20*(12), 1451-1469.

Dequincey, O., F. Chabaux, N. Clauer, N. Liewig, and J.-P. Muller (1999), Dating of weathering profiles by radioactive disequilibria: Contribution of the study of authigenic mineral fractions, *Comptes Rendus de l'Académie des Sciences - Series IIA - Earth and Planetary Science*, *328*(10), 679-685.

Dequincey, O., F. Chabaux, N. Clauer, O. Sigmarsson, N. Liewig, and J. C. Leprun (2002), Chemical mobilizations in laterites: evidence from trace elements and ^{238}U-^{234}U-^{230}Th disequilibria, *Geochimica et Cosmochimica Acta*, *66*(7), 1197-1210.

Dia, A., C. Chauvel, M. Bulourde, and M. Gérard (2006), Eolian contribution to soils on Mount Cameroon: Isotopic and trace element records, *Chemical Geology*, *226*(3–4), 232-252.

Díaz-Hernández, J. L., and J. Rüoss (2009), Atmospheric dust additions as a soil formation factor, in *Advances in studies on desertification : contributions to the International Conference on Desertification in memory of professor John B. Thornes.* , edited by A. Romero DiazF. Belmonte SerratoF. Alonso SarriaF. Lopez Bermudez, pp. 227-230, Servicio de Publicaciones, Universidad de Murcia, Murcia.

DiBiase, R. A., K. X. Whipple, A. M. Heimsath, and W. B. Ouimet (2010), Landscape form and millennial erosion rates in the San Gabriel Mountains, CA, *Earth and Planetary Science Letters*, *289*(1-2), 134-144.

Dietrich, W. E., R. Reiss, M.-L. Hsu, and D. R. Montgomery (1995), A process-based model for colluvial soil depth and shallow landsliding using digital elevation data, *Hydrological Processes*, *9*(3-4), 383-400.

Dixon, J. L., and F. von Blanckenburg (2012), Soils as pacemakers and limiters of global silicate weathering, *Comptes Rendus Geoscience*, *344*(11-12), 597-609.

Dixon, J. L., A. M. Heimsath, and R. Amundson (2009), The critical role of climate and saprolite weathering in landscape evolution, *Earth Surface Processes and Landforms*, *34*(11), 1507-1521.

Dixon, J. L., A. S. Hartshorn, A. M. Heimsath, R. A. DiBiase, and K. X. Whipple (2012), Chemical weathering response to tectonic forcing: A soils perspective from the San Gabriel Mountains, California, *Earth and Planetary Science Letters*, *323-324*, 40-49.

Dosseto, A., B. Bourdon, and S. P. Turner (2008a), Uranium-series isotopes in river materials: Insights into the timescales of erosion and sediment transport, *Earth and Planetary Science Letters*, *265*(1-2), 1-17.

Dosseto, A., S. P. Turner, and J. Chappell (2008b), The evolution of weathering profiles through time: New insights from uranium-series isotopes, *Earth and Planetary Science Letters*, *274*(3-4), 359-371.

Dosseto, A., H. Buss, and P. O. Suresh (2011), The delicate balance between soil production and erosion, and its role on landscape evolution, *Applied Geochemistry*, *26*, S24-S27.

Dosseto, A., H. L. Buss, and P. O. Suresh (2012), Rapid regolith formation over volcanic

bedrock and implications for landscape evolution, *Earth and Planetary Science Letters*, *337-338*, 47-55.

Dosseto, A., H. L. Buss, and F. Chabaux (2014), Age and weathering rate of sediments in small catchments: The role of hillslope erosion, *Geochimica et Cosmochimica Acta*, *132*(0), 238-258.

Drever, J. I., and L. L. Stillings (1997), The role of organic acids in mineral weathering, *Colloids and Surfaces A: Physicochemical and Engineering Aspects*, *120*(1–3), 167-181.

Du, X., A. W. Rate, and M. A. M. Gee (2012), Redistribution and mobilization of titanium, zirconium and thorium in an intensely weathered lateritic profile in Western Australia, *Chemical Geology*, *330–331*, 101-115.

Dudal, R. (2004), The sixth factor of soil fromation, in *Soil Classification 2004*, edited by P.V. Krasnilikov, Petrozavodsk, Russia.

Dunai, T. J. (2000), Scaling factors for production rates of in situ produced cosmogenic nuclides: a critical reevaluation, *Earth and Planetary Science Letters*, *176*, 157-169.

Egli, M., and P. Fitze (2000), Formulation of pedologic mass balance based on immobile elements: a revision, *Soil Science*, *165*(5), 437-443.

ESRI (2009), World Street Map.

Estrela, T., C. Marcuello, and C. Iglesias (1997), Water resources problems in Southern Europe*Rep.*, EEA (European Environment Agency), Denmark.

Ferrier, K. L., and J. W. Kirchner (2008), Effects of physical erosion on chemical denudation rates: A numerical modeling study of soil-mantled hillslopes, *Earth and Planetary Science Letters*, *272*(3-4), 591-599.

Ferrier, K. L., J. W. Kirchner, and R. C. Finkel (2012), Weak influences of climate and mineral supply rates on chemical erosion rates: Measurements along two altitudinal transects in the Idaho Batholith, *Journal of Geophysical Research*, *117*(F2).

Ferrier, K. L., J. W. Kirchner, C. S. Riebe, and R. C. Finkel (2010), Mineral-specific chemical weathering rates over millennial timescales: Measurements at Rio Icacos, Puerto Rico, *Chemical Geology*, *277*(1-2), 101-114.

Finke, P. A., A. Samouëlian, M. Suarez-Bonnet, B. Laroche, and S. S. Cornu (2015), Assessing the usage potential of SoilGen2 to predict clay translocation under forest and agricultural land uses, *European Journal of Soil Science*, *66*(1), 194-205.

Fleischer, R. L. (1982), Alpha-recoil damage and solution effects in minerals: uranium isotopic disequilibrium and radon release, *Geochimica et Cosmochimica Acta*,

46(11), 2191-2201.

Foley, J. A., et al. (2005), Global consequences of land use, *Science*, *309*(5734), 570-574.

Frank, H. T., M. E. B. Gomes, and M. L. L. Formoso (2009), Review of the areal extent and the volume of the Serra Geral Formation, Paraná Basin, South America, *Pesquisas em Geociências*, *36*(1), 49-57.

Furbish, D. J. (2003), Using the dynamically coupled behavior of land ‐ surface geometry and soil thickness in developing and testing hillslope evolution models, *Prediction in Geomorphology*, 169-181.

Gabet, E. J. (2007), A theoretical model coupling chemical weathering and physical erosion in landslide-dominated landscapes, *Earth and Planetary Science Letters*, *264*(1-2), 259-265.

Gabet, E. J., and S. M. Mudd (2009), A theoretical model coupling chemical weathering rates with denudation rates, *Geology*, *37*(2), 151-154.

García, A. (2009), *Atlas Geográfico de la Provincia de Almería. El medio. La sociedad. Las actividades* 1st ed., Instituto de Estudios Almerienses, Almería.

Goddéris, Y., L. M. François, A. Probst, J. Schott, D. Moncoulon, D. Labat, and D. Viville (2006), Modelling weathering processes at the catchment scale: The WITCH numerical model, *Geochimica et Cosmochimica Acta*, *70*(5), 1128-1147.

Gosse, J. C., and F. M. Phillips (2001), Terrestrial in situ cosmogenic nuclides: theory and application, *quaternary Science Reviews*, *20*, 1475-1560.

Govindaraju, K., P. J. Potts, P. C. Webb, and J. S. Watson (1994), 1994 repor t on Whin sill dolerite WS ‐ E from England and Pitscurrie microgabbro PM ‐ S from Scotland: assess-ment by one hundred and four international laboratories, *Geostandards Newsletter*, *18*(2), 211-300.

Graly, J. A., P. R. Bierman, L. J. Reusser, and M. J. Pavich (2010), Meteoric ^{10}Be in soil profiles – A global meta-analysis, *Geochimica et Cosmochimica Acta*, *74*(23), 6814-6829.

Granet, M., F. Chabaux, P. Stille, C. France-Lanord, and E. Pelt (2007), Time-scales of sedimentary transfer and weathering processes from U-series nuclides: Clues from the Himalayan rivers, *Earth and Planetary Science Letters*, *261*(3–4), 389-406.

Granet, M., F. Chabaux, P. Stille, A. Dosseto, C. France-Lanord, and E. Blaes (2010), U-series disequilibria in suspended river sediments and implication for sediment transfer time in alluvial plains: The case of the Himalayan rivers, *Geochimica et Cosmochimica Acta*, *74*(10), 2851-2865.

Green, E. G., W. E. Dietrich, and J. F. Banfield (2006), Quantification of chemical weathering rates across an actively eroding hillslope, *Earth and Planetary Science Letters*, *242*(1), 155-169.

Heckman, K., and C. Rasmussen (2011), Lithologic controls on regolith weathering and mass flux in forested ecosystems of the southwestern USA, *Geoderma*, *164*(3–4), 99-111.

Heimsath, A. M. (1997), The soil production function and landscape equilibrium, *Nature*, *388*, 358-361.

Heimsath, A. M., W. E. Dietrich, K. Nishiizumi, and R. C. Finkel (1999), Cosmogenic nuclides, topography, and the spatial variation of soil depth, *Geomorphology*, *27*(1–2), 151-172.

Heimsath, A. M., J. Chappell, W. E. Dietrich, K. Nishiizumi, and R. C. Finkel (2001), Late Quaternary erosion in southeastern Australia: a field example using cosmogenic nuclides, *Quaternary International*, *83-85*.

Hewawasam, T., F. von Blanckenburg, J. Bouchez, J. L. Dixon, J. A. Schuessler, and R. Maekeler (2013), Slow advance of the weathering front during deep, supply-limited saprolite formation in the tropical Highlands of Sri Lanka, *Geochimica et Cosmochimica Acta*, *118*(0), 202-230.

Hilley, G. E., C. P. Chamberlain, S. Moon, S. Porder, and S. D. Willett (2010), Competition between erosion and reaction kinetics in controlling silicate-weathering rates, *Earth and Planetary Science Letters*, *293*(1-2), 191-199.

Hodson, M. E., and S. J. Langan (1999), The influence of soil age on calculated mineral weathering rates, *Applied Geochemistry*, *14*(3), 387-394.

Holden, J. (2005), *An introduction to physical geography and the environment*, Pearson Education.

Hooke, R. L. (2000), On the history of humans as geomorphic agents, *Geology*, *28*(9), 843-846.

IBGE (2016), MAPA - GEOLOGIA (WebsService), Insituto Brasileiro de Geografia e Estatística, Rio de Janeiro.

ICONA (1988), *Proyecto LUCDEME. Alhama de Almería: Mapa de suelos, escala 1:100.000 (Estación Experimental del Zaidín)*, 147 pp., ICONA, España.

IUSS Working Group WRB (Ed.) (2014), *World Reference Base for Soil Resources 2014. International soil classification system for naming soils and creating legends for soil maps*, FAO, Rome.

Ivanovich, M., and R. S. Harmon (1992), Uranium-series disequilibrium: applications to earth, marine, and environmental sciences. 2.

Ivy-Ochs, S., and F. Kober (2008), Surface exposure dating with cosmogenic nuclides,

Quaternary Science Journal, *57*(1-2), 157-189.

Jabaloy-Sánchez, A., E. M. Fernández-Fernández, and F. González-Lodeiro (2007), A cross section of the eastern Betic Cordillera (SE Spain) according field data and a seismic reflection profile, *Tectonophysics*, *433*(1-4), 97-126.

Jenny, H. (1941), Factors of soil formation. A System of Quantitative Pedology, edited by McGraw-Hill, New York.

Jin, L., R. Ravella, B. Ketchum, P. R. Bierman, P. Heaney, T. White, and S. L. Brantley (2010), Mineral weathering and elemental transport during hillslope evolution at the Susquehanna/Shale Hills Critical Zone Observatory, *Geochimica et Cosmochimica Acta*, *74*(13), 3669-3691.

Jungers, M. C., P. R. Bierman, A. Matmon, K. Nichols, J. Larsen, and R. Finkel (2009), Tracing hillslope sediment production and transport with in situ and meteoric ^{10}Be, *Journal of Geophysical Research*, *114*(F4).

Junta de Andalucía (2004), Conjunto de datos de Geología de Andalucía: Edad Geológica, Estructuras, Geoestructuras, Unidades Litológicasy Unidades Tectónicas. Consejería de Medio Ambiente (1:400000), edited, Consejería de Agricultura, Pesca y Medio Ambiente.

Junta de Andalucía (2005), Modelo digital del terreno de Andalucia (1:20000; 10-m resolución), edited, Consejería de Agricultura, Pesca y Medio Ambiente.

Junta de Andalucía (2008), Evapotranspiración potencial media anual en Andalucía: periodo 1971-2000 (v2008), edited, Consejería de Agricultura, Pesca y Medio Ambiente.

Kirchner, J. W., C. S. Riebe, K. L. Ferrier, and R. C. Finkel (2006), Cosmogenic nuclide methods for measuring long-term rates of physical erosion and chemical weathering, *Journal of Geochemical Exploration*, *88*(1-3), 296-299.

Koide, M., and E. D. Goldberg (1963), Uranium-234/uranium-238 ratios in sea water, *Progress in Oceanography*, *3*, 173-177.

Krasilnikov, P. V., N. E. G. Calderón, S. N. Sedov, E. V. Gómez, and R. R. Bello (2005), The relationship between pedogenic and geomorphic processes in mountainous tropical forested area in Sierra Madre del Sur, Mexico, *CATENA*, *62*(1), 14-44.

Kubik, P. W., and M. Christl (2010), ^{10}Be and ^{26}Al measurements at the Zurich 6MV Tandem AMS facility, *Nuclear Instruments and Methods in Physics Research Section B: Beam Interactions with Materials and Atoms*, *268*(7-8), 880-883.

Kurtz, A. C., L. A. Derry, O. A. Chadwick, and M. J. Alfano (2000), Refractory element mobility in volcanic soils, *Geology*, *28*(8), 683-686.

Lal, D. (1991), Cosmic ray labeling of erosion surfaces: in situ nuclide production rates

and erosion models, *Earth and Planetary Science Letters*, *104*(2–4), 424-439.

Larsen, I. J., P. C. Almond, A. Eger, J. O. Stone, D. R. Montgomery, and B. Malcolm (2014), Rapid soil production and weathering in the Southern Alps, New Zealand, *Science*, *343*(6171), 637-640.

Lebedeva, M. I., R. C. Fletcher, and S. L. Brantley (2010), A mathematical model for steady-state regolith production at constant erosion rate, *Earth Surface Processes and Landforms*, *35*(5), 508-524.

Li, G., and H. Elderfield (2013), Evolution of carbon cycle over the past 100 million years, *Geochimica et Cosmochimica Acta*, *103*, 11-25.

Ma, L., F. Chabaux, E. Pelt, E. Blaes, L. Jin, and S. Brantley (2010), Regolith production rates calculated with uranium-series isotopes at Susquehanna/Shale Hills Critical Zone Observatory, *Earth and Planetary Science Letters*, *297*(1-2), 211-225.

Ma, L., F. Chabaux, N. West, E. Kirby, L. Jin, and S. Brantley (2013), Regolith production and transport in the Susquehanna Shale Hills Critical Zone Observatory, Part 1: Insights from U‐series isotopes, *Journal of Geophysical Research: Earth Surface*, *118*(2), 722-740.

Maher, K. (2011), The role of fluid residence time and topographic scales in determining chemical fluxes from landscapes, *Earth and Planetary Science Letters*, *312*(1–2), 48-58.

Maher, K., and C. P. Chamberlain (2014), Hydrologic Regulation of Chemical Weathering and the Geologic Carbon Cycle, *Science*, *343*(6178), 1502-1504.

Maher, K., and F. von Blanckenburg (2016), Surface ages and weathering rates from 10Be (meteoric) and 10Be/9Be: Insights from differential mass balance and reactive transport modeling, *Chemical Geology*.

Masana, E., R. Pallàs, H. Perea, M. Ortuño, J. J. Martínez-Díaz, E. García-Meléndez, and P. Santanach (2005), Large Holocene morphogenic earthquakes along the Albox fault, Betic Cordillera, Spain, *Journal of Geodynamics*, *40*(2-3), 119-133.

Mathieu, D., M. Bernat, and D. Nahon (1995), Short-lived U and Th isotope distribution in a tropical laterite derived from granite (Pitinga river basin, Amazonia, Brazil): Application to assessment of weathering rate, *Earth and Planetary Science Letters*, *136*(3–4), 703-714.

McKean, J. A., W. E. Dietrich, R. C. Finkel, J. R. Southon, and M. W. Caffee (1993), Quantification of soil production and downslope creep rates from cosmogenic ^{10}Be accumulations on a hillslope profile, *Geology*, *21*(4), 343-346.

Melfi, A. J., F. Subies, D. Nahon, and M. L. L. Formoso (1996), Zirconium mobility in bauxites of Southern Brazil, *Journal of South American Earth Sciences*, *9*(3–4), 161-170.

Merry, R. (2009), Acidity and alkalinity of soils, *Environmental and ecological chemistry*, *2*.

Millot, R., J. Gaillardet, B. Durpré, and J. C. Allègre (2002), The global control of silicate weathering rates and the coupling with physical erosion: new insights from rivers of the Canadian Shield, *Earth and Planetary Science Letters*, *196*, 83-98.

Minasny, B., and A. B. McBratney (2001), A rudimentary mechanistic model for soil formation and landscape development: II. A two-dimensional model incorporating chemical weathering, *Geoderma*, *103*(1–2), 161-179.

Minella, J. P. G., D. E. Walling, and G. H. Merten (2014), Establishing a sediment budget for a small agricultural catchment in southern Brazil, to support the development of effective sediment management strategies, *Journal of Hydrology*, *519, Part B*, 2189-2201.

Miyake, Y., Y. Sugimura, and T. Uchida (1966), Ratio $^{234}U/^{238}U$ and the uranium concentration in seawater in the western North Pacific, *Journal of Geophysical Research*, *71*(12), 3083-3087.

Montanheiro, T. J., J. K. Yamamoto, and Y. Kihara (2004), Serra Geral Formation—São Paulo State, Brazil: a potential source for natural pozzolans, *Materials Letters*, *58*(6), 876-881.

Montgomery, D. R. (2007), Soil erosion and agricultural sustainability, *Proceedings of the National Academy of Sciences of the United States of America*, *104*(33), 13268-13272.

Moriasi, D., J. Arnold, M. Van Liew, R. Bingner, R. Harmel, and T. Veith (2007), Model evaluation guidelines for systematic quantification of accuracy in watershed simulations, *Trans. Asabe*, *50*(3), 885-900.

Mudd, S. M., and D. J. Furbish (2004), Influence of chemical denudation on hillslope morphology, *Journal of Geophysical Research: Earth Surface*, *109*(F2), n/a-n/a.

Mudd, S. M., and D. J. Furbish (2006), Using chemical tracers in hillslope soils to estimate the importance of chemical denudation under conditions of downslope sediment transport, *Journal of Geophysical Research*, *111*(F2).

Mudd, S. M., K. Yoo, and E. J. Gabet (2013), Influence of Chemical Weathering on Hillslope Forms, in *Environmental Sciences Treatise on Geomorphology*, edited, pp. 56-65, Academic Press, San Diego, CA.

National Research Council (2001), Basic Research Opportunities in Earth Science, edited, p. 168, The National Academies Press, Washington, DC.

Norton, K. P., and V. Vanacker (2009), Effects of terrain smoothing on topographic shielding correction factors for cosmogenic nuclide-derived estimates of basin-averaged denudation rates, *Earth Surface Processes and Landforms*, *34*(1), 145-

154.

Norton, K. P., and F. von Blanckenburg (2010), Silicate weathering of soil-mantled slopes in an active Alpine landscape, *Geochimica et Cosmochimica Acta*, *74*(18), 5243-5258.

NRC-CRM Marine sediment, edited, Canada.

Opolot, E., Y. Y. Yu, and P. A. Finke (2015), Modeling soil genesis at pedon and landscape scales: Achievements and problems, *Quaternary International*, *376*, 34-46.

Ouimet, W. B., K. X. Whipple, and D. E. Granger (2009), Beyond threshold hillslopes: Channel adjustment to base-level fall in tectonically active mountain ranges, *Geology*, *37*(7), 579-582.

Palmer, W. C., and V. A. Havens (1958), A graphical technique for determining evapotranspiration by the thornthwaite method, *Monthly Weather Review 86*, 123-128.

Pavich, M. J., L. Brown, J. Klein, and R. Middleton (1984), ^{10}Be accumulation in a soil chronosequence, *Earth and Planetary Science Letters*, *68*(2), 198-204.

Pelletier, J. D., and C. Rasmussen (2009), Geomorphically based predictive mapping of soil thickness in upland watersheds, *Water Resources Research*, *45*(9).

Pelt, E., F. Chabaux, C. Innocent, A. K. Navarre-Sitchler, P. B. Sak, and S. L. Brantley (2008), Uranium–thorium chronometry of weathering rinds: Rock alteration rate and paleo-isotopic record of weathering fluids, *Earth and Planetary Science Letters*, *276*(1–2), 98-105.

Pelt, E., F. Chabaux, P. Stille, C. Innocent, B. Ghaleb, M. Girard, and F. Guntzer (2013), Atmospheric dust contribution to the budget of U-series nuclides in soils from the Mount Cameroon volcano, *Chemical Geology*, *341*, 147-157.

Penck, W. (1953), *Morphological Analysis of Landfroms. English translation by Czech, H., Boswell, K.C., 1953 (Written in 1924)*, Macmillan, London.

Phillips, J. D. (2010), The convenient fiction of steady-state soil thickness, *Geoderma*, *156*(3-4), 389-398.

Polo, L. A., and V. d. A. Janasi (2014), Volcanic stratigraphy of intermediate to acidic rocks in southern Paraná Magmatic Province, Brazil, *Geologia USP. Série Científica*, *14*(2), 83-100.

Portenga, E. W., and P. R. Bierman (2011), Understanding Earth's eroding surface with ^{10}Be, *GSA Today*, *21*(8), 4-10.

Preusser, F., D. Degering, M. Fuchs, A. Hilgers, A. Kadereit, N. Klasen, M. Krbetschek, D. Richter, and J. Q. Spencer (2008), Luminescence dating: basics, methods and applications, *Quaternary Science Journal*, *57*(1-2), 95-149.

Quirk, J., D. J. Beerling, S. A. Banwart, G. Kakonyi, M. E. Romero-Gonzalez, and J. R. Leake (2012), Evolution of trees and mycorrhizal fungi intensifies silicate mineral weathering, *Biology letters*, *8*(6), 1006-1011.

Rasmussen, C., R. A. Dahlgren, and R. J. Southard (2010), Basalt weathering and pedogenesis across an environmental gradient in the southern Cascade Range, California, USA, *Geoderma*, *154*(3–4), 473-485.

Rasmussen, C., S. Brantley, D. d. Richter, A. Blum, J. Dixon, and A. F. White (2011), Strong climate and tectonic control on plagioclase weathering in granitic terrain, *Earth and Planetary Science Letters*, *301*(3–4), 521-530.

Raymo, M. E., and W. F. Ruddiman (1992), Tectonic forcing of the Late Cenozoic climate, *Nature*, *359*, 117-122.

Raymond, P. A., and J. J. Cole (2003), Increase in the export of alkalinity from North America's largest river, *Science*, *301*(5629), 88-91.

Renner, L. C., L. A. Hartmann, W. Wildner, H.-J. Massonne, and T. Theye (2011), A micro-analytical approach to partition coefficients in plagioclase and clinopyroxene of basaltic sills in Serra Geral Formation, Paraná Basin, Brazil., *Rev. bras. geociênc.*, *41*(2), 263-289.

Richter, D. d. J. (2007), Humanity's transformation of earth's soil: Pedology's New Frontier, *Soil Science*, *172*(12), 957–967.

Riebe, C. S., J. W. Kirchner, and R. C. Finkel (2003), Long-term rates of chemical weathering and physical erosion from cosmogenic nuclides and geochemical mass balance, *Geochimica et Cosmochimica Acta*, *67*(22), 4411-4427.

Riebe, C. S., J. W. Kirchner, and R. C. Finkel (2004), Erosional and climatic effects on long-term chemical weathering rates in granitic landscapes spanning diverse climate regimes, *Earth and Planetary Science Letters*, *224*(3-4), 547-562.

Riebe, C. S., J. W. Kirchner, D. E. Granger, and R. C. Finkel (2001), Strong tectonic and weak climatic control of long-term chemical weathering rates, *Geology*, *29*(6), 511-514.

Riggins, S. G., R. S. Anderson, S. P. Anderson, and A. M. Tye (2011), Solving a conundrum of a steady-state hilltop with variable soil depths and production rates, Bodmin Moor, UK, *Geomorphology*, *128*(1–2), 73-84.

Riotte, J., F. Chabaux, M. Benedetti, A. Dia, M. Gérard, J. Boulègue, and J. Etamé (2003), Uranium colloidal transport and origin of the ^{234}U–^{238}U fractionation in surface waters: new insights from Mount Cameroon, *Chemical Geology*, *202*(3-4), 365-381.

Ritchie, G. S. P. (1995), Soluble aluminium in acidic soils: Principles and practicalities, in *Plant-Soil Interactions at Low pH: Principles and Management: Proceedings of the Third International Symposium on Plant-Soil Interactions at Low pH,*

Brisbane, Queensland, Australia, 12–16 September 1993, edited by R. A. DateN. J. GrundonG. E. RaymentM. E. Probert, pp. 23-33, Springer Netherlands, Dordrecht.

Robert Bierman, P., and K. K. Nichols (2004), Rock to sediment - Slope to sea with ^{10}Be - Rates of landscape change, *Annual Review of Earth and Planetary Sciences*, *32*(1), 215-255.

Rodríguez, S., X. Querol, A. Alastuey, G. Kallos, and O. Kakaliagou (2001), Saharan dust contributions to PM10 and TSP levels in Southern and Eastern Spain, *Atmospheric Environment*, *35*(14), 2433-2447.

Roering, J. J. (2008), How well can hillslope evolution models "explain" topography? Simulating soil transport and production with high-resolution topographic data, *Geological Society of America Bulletin*, *120*(9-10), 1248-1262.

Roering, J. J., J. Marshall, A. M. Booth, M. Mort, and Q. Jin (2010), Evidence for biotic controls on topography and soil production, *Earth and Planetary Science Letters*, *298*(1–2), 183-190.

Rognon, P. (1987), Late quaternary climatic reconstruction for the maghreb (North Africa), *Palaeogeography, Palaeoclimatology, Palaeoecology*, *58*(1), 11-34.

Samouëlian, A., P. Finke, Y. Goddéris, and S. Cornu (2012), *Hydrologic information in pedologic models*, Elsevier.

Schaetzl, R. J. (2013), 4.9 Catenas and Soils A2 - Shroder, John F, in *Treatise on Geomorphology*, edited, pp. 145-158, Academic Press, San Diego.

Scheuvens, D., L. Schütz, K. Kandler, M. Ebert, and S. Weinbruch (2013), Bulk composition of northern African dust and its source sediments — A compilation, *Earth-Science Reviews*, *116*(0), 170-194.

Schoonejans, J., V. Vanacker, S. Opfergelt, M. Granet, and F. Chabaux (2016a), Coupling uranium series and 10Be cosmogenic radionuclides to evaluate steady-state soil thickness in the Betic Cordillera, *Chemical Geology*.

Schoonejans, J., V. Vanacker, S. Opfergelt, Y. Ameijeiras-Mariño, and M. Christl (2016b), Kinetically limited weathering at low denudation rates in semiarid climatic conditions, *Journal of Geophysical Research: Earth Surface*, *121*(2), 336-350.

Selby, M. J. (1992), *Hillslope materials and processes*, 2nd ed., Oxford university Press, Oxford.

Stallard, R. F., and J. M. Edmond (1983), Geochemistry of the Amazon: 2. The influence of geology and weathering environment on the dissolved load, *Journal of Geophysical Research: Oceans*, *88*(C14), 9671-9688.

Suresh, P. O., A. Dosseto, P. P. Hesse, and H. K. Handley (2013), Soil formation rates

determined from Uranium-series isotope disequilibria in soil profiles from the southeastern Australian highlands, *Earth and Planetary Science Letters*, *379*, 26-37.

Syvitski, J. P. M., and A. Kettner (2011), Sediment flux and the Anthropocene, *Philosophical Transactions of the Royal Society A: Mathematical, Physical and Engineering Sciences*, *369*(1938), 957-975.

Trigalet, T., C. Chartin, E. Aldana Jague, K. Van Oost, and B. Van Wesemael (in prep.), Soil organic carbon distribution in an agricultural catchment in Southern Brazil: 6 from hillslope to catchment scale.

Turner, S., M. Regelous, S. Kelley, C. Hawkesworth, and M. Mantovani (1994), Magmatism and continental break-up in the South Atlantic: high precision 40 Ar-39 Ar geochronology, *Earth and Planetary Science Letters*, *121*(3), 333-348.

UNSO/UNDP (1997), Aridity zones and dryland popultaion An Assessment of Population Levels in the World's Drylands, edited, New York.

Vanacker, V., F. von Blanckenburg, T. Hewawasam, and P. W. Kubik (2007), Constraining landscape development of the Sri Lankan escarpment with cosmogenic nuclides in river sediment, *Earth and Planetary Science Letters*, *253*(3–4), 402-414.

Vanacker, V., N. Bellin, A. Molina, and P. W. Kubik (2014), Erosion regulation as a function of human disturbances to vegetation cover: a conceptual model, *Landscape Ecology*, *29*(2), 293-309.

Vanwalleghem, T., U. Stockmann, B. Minasny, and A. B. McBratney (2013), A quantitative model for integrating landscape evolution and soil formation, *Journal of Geophysical Research: Earth Surface*, *118*(2), 331-347.

Vigier, N. (2001), Erosion timescales derived from U-decay series measurements in rivers, *Earth and Planetary Science Letters*, *193*, 549-563.

Vigier, N., K. W. Burton, S. R. Gislason, N. W. Rogers, S. Duchene, L. Thomas, E. Hodge, and B. Schaefer (2006), The relationship between riverine U-series disequilibria and erosion rates in a basaltic terrain, *Earth and Planetary Science Letters*, *249*(3-4), 258-273.

von Blanckenburg, F. (2005), The control mechanisms of erosion and weathering at basin scale from cosmogenic nuclides in river sediment, *Earth and Planetary Science Letters*, *237*(3-4), 462-479.

von Blanckenburg, F., and J. K. Willenbring (2014), Cosmogenic Nuclides: Dates and Rates of Earth-Surface Change, *Elements*, *10*(5), 341-346.

von Blanckenburg, F., N. S. Belshaw, and R. K. O'Nions (1996a), Separation of 9Be and cosmogenic ^{10}Be from environmental materials and SIMS isotope dilution

analysis, *Chemical Geology*, *129*(1–2), 93-99.

von Blanckenburg, F., N. S. Belshaw, and R. K. O'Nions (1996b), Separation of ^{9}Be and cosmogenic ^{10}Be from environmental materials and SIMS isotope dilution analysis, *Chemical Geology*, *129*, 93-99.

von Blanckenburg, F., J. Bouchez, and H. Wittmann (2012), Earth surface erosion and weathering from the 10 Be (meteoric)/9 Be ratio, *Earth and Planetary Science Letters*, *351*, 295-305.

Weijermars, R. R., Th.b. , B. Van den Eeckout, and G. K. Postma, K. (1985), Uplift History of a Betic Fold Nappe Inferred from Neogene-Quaternary Sedimentation and Tectonics (in the Sierra Alhamilla and Almería, Sorbas and Tabernas Basins of the Betic Cordilleras, SE Spain), *Geologie en Mijnbouw*, *64*, 397-411.

WEPAL ISE reference material, marine clay, edited, Wageningen, Netherlands.

West, A., A. Galy, and M. Bickle (2005), Tectonic and climatic controls on silicate weathering, *Earth and Planetary Science Letters*, *235*(1-2), 211-228.

West, N., E. Kirby, P. Bierman, R. Slingerland, L. Ma, D. Rood, and S. Brantley (2013), Regolith production and transport at the Susquehanna Shale Hills Critical Zone Observatory, part 2: insights from meteoric ^{10}Be, *Journal of Geophysical Research: Earth Surface*, *118*(3), 1877-1896.

White, A. F., and A. E. Blum (1995), Effects of climate on chimical weathering in watersheds, *Geochimica et Cosmochimica Acta*, *59*(9), 1729-1747.

White, A. F., and S. L. Brantley (2003), The effect of time on the weathering of silicate minerals: why do weathering rates differ in the laboratory and field?, *Chemical Geology*, *202*(3–4), 479-506.

White, A. F., and H. L. Buss (2014), 7.4 - Natural Weathering Rates of Silicate Minerals A2 - Holland, Heinrich D, in *Treatise on Geochemistry (Second Edition)*, edited by Karl K. Turekian, pp. 115-155, Elsevier, Oxford.

White, A. F., A. E. Blum, M. S. Schulz, T. D. Bullen, J. W. Harden, and M. L. Peterson (1996), Chemical weathering rates of a soil chronosequence on granitic alluvium: I. Quantification of mineralogical and surface area changes and calculation of primary silicate reaction rates, *Geochimica et Cosmochimica Acta*, *60*(14), 2533-2550.

White, A. F., A. Blum, T. D. Bullen, D. V. Vivit, M. Schulz, and J. Fitzpatrick (1999), The effect of temperature on experimental and natural chemical weathering rates of granitoid rocks, *Geochimica et Cosmochimica Acta*, *63*, 3277-3291.

White, A. F., M. S. Schulz, D. A. Stonestrom, D. V. Vivit, J. Fitzpatrick, T. D. Bullen, K. Maher, and A. E. Blum (2009), Chemical weathering of a marine terrace chronosequence, Santa Cruz, California. Part II: Solute profiles, gradients and

the comparisons of contemporary and long-term weathering rates, *Geochimica et Cosmochimica Acta*, *73*(10), 2769-2803.

Wilkinson, B. H. (2005), Humans as geologic agents: A deep-time perspective, *Geology*, *33*(3), 161.

Wilkinson, B. H., and B. J. McElroy (2007), The impact of humans on continental erosion and sedimentation, *Geological Society of America Bulletin*, *119*(1-2), 140-156.

Willenbring, J. K., and F. von Blanckenburg (2010), Meteoric cosmogenic Beryllium-10 adsorbed to river sediment and soil: Applications for Earth-surface dynamics, *Earth-Science Reviews*, *98*(1), 105-122.

Wilson, S. (1997), Data compilation for USGS reference material BHVO-2, Hawaiian basalt, *US Geological Survey Open-File Report*.

Wittmann, H., F. von Blanckenburg, J. Bouchez, N. Dannhaus, R. Naumann, M. Christl, and J. Gaillardet (2012), The dependence of meteoric ^{10}Be concentrations on particle size in Amazon River bed sediment and the extraction of reactive 10 Be/9 Be ratios, *Chemical Geology*, *318*, 126-138.

Wyshnytzky, C. E., W. B. Ouimet, J. McCarthy, D. P. Dethier, R. R. Shroba, P. R. Bierman, and D. H. Rood (2015), Meteoric ^{10}Be, clay, and extractable iron depth profiles in the Colorado Front Range: Implications for understanding soil mixing and erosion, *CATENA*, *127*, 32-45.

Yoo, K., and S. M. Mudd (2008), Toward process-based modeling of geochemical soil formation across diverse landforms: A new mathematical framework, *Geoderma*, *146*(1-2), 248-260.

Yoo, K., R. Amundson, A. M. Heimsath, W. E. Dietrich, and G. H. Brimhall (2007), Integration of geochemical mass balance with sediment transport to calculate rates of soil chemical weathering and transport on hillslopes, *Journal of Geophysical Research*, *112*(F2).

Yoo, K., S. M. Mudd, J. Sanderman, R. Amundson, and A. Blum (2009), Spatial patterns and controls of soil chemical weathering rates along a transient hillslope, *Earth and Planetary Science Letters*, *288*(1–2), 184-193.

Yoo, K., B. Weinman, S. M. Mudd, M. Hurst, M. Attal, and K. Maher (2011), Evolution of hillslope soils: The geomorphic theater and the geochemical play, *Applied Geochemistry*, *26*, *Supplement*, S149-S153.

You, C.-F., T. Lee, and Y.-H. Li (1989), The partition of Be between soil and water, *Chemical Geology*, *77*(2), 105-118.

Yu, Y. Y., P. A. Finke, H. B. Wu, and Z. T. Guo (2013), Sensitivity analysis and calibration of a soil carbon model (SoilGen2) in two contrasting loess forest soils, *Geosci. Model Dev.*, *6*(1), 29-44.

List of Figures

List of Tables